FINITE ELEMENT MODELING OF IMPACT CRATERING-INDUCED CAVE FORMATION ON MARS:

ASTROBIOLOGIC AND GEOLOGIC IMPLICATIONS

by

Erin K. Kay

Submitted in Partial Fulfillment
of the Requirements for the

Master of Science in Geology

New Mexico Institute of Mining and Technology
Department of Earth and Environmental Science

Socorro, New Mexico

February 2008

Abstract

The Martian subsurface could be the last refuge for a hypothetical Mars biosphere in which caves, or vugs, as well as the near-subsurface fracture habitat, serve as possible microbiological repositories (Boston, *et al.*, 1992; Boston, *et al.*, 2001 & 2006). From this hypothesis, the following questions arise: 1) do some sort of solutional caves exist on Mars; 2) could such caves form as a result of an impact cratering event that creates fractures and liberates ices as a fluid; and 3) could an impact crater ejecta blanket extend the duration of a thermally favorable underlying near-subsurface microbiological habitat? One unusual hypothetical mechanism for cave formation involves an impact event and rapid melting and/or volatilization of subsurface ice to produce solutional voids ("catastrophic speleogenesis", Boston, *et al.*, 2006). The plausibility of a surface biological habitat in such a cold environment created as a result of heat imparted by a crater ejecta blanket deposited around the impact crater site has been suggested for Earth with implications for similar events on Mars (Cockell and Pascal, 2002). This idea is extended here to include subsurface cave habitats created as a result of the impact event itself. These notions are quantitatively constrained through computer-based modeling simulations of impacts into relevant rock and ice terrains. The modeling accounts for aspects of possible cave formation events at various locations, as well as a generalized representation of interactions between an ejecta blanket and a variety of underlying material types. Subsurface and surface compositions, amount and spatial distribution of

energy imparted and associated heat, certain impactor properties and possible microbiological implications are also considered.

Based on modeling results, a first order prediction is made of the plausibility of speleogenesis as a result of an impact cratering event, of temperatures in which possible microbiological activity could occur, as well as likely durations of sufficiently high temperatures for microbiological activity. Modeling results indicate that catastrophic speleogenesis is plausible as a result of an impact cratering event. In addition, temperatures were deemed sufficiently high for an adequate period of time to facilitate the existence of microbiological activity within the crater site.

Modeling results were then compared to the interpretation of orbiter and MER imaging to identify possible site types of subsurface cavity formation in order to aid in site selection for future Mars missions.

Acknowledgements

I would like to thank all the people who have supported and encouraged me through the completion of this research. Those directly involved with the research played an important role in my understanding of the way research projects progress: Penelope J. Boston (NMT) who suggested this research topic and supported the entire work; Horton Newsom (UNM) who always kept me on my toes with respect to the specifics of the modeling process; Philip Kyle (NMT) who filled in the blanks of my knowledge of the NMT Graduate Administration policies; Eileen Ryan (NMT) who joined this project in mid-stream but has shown me that two professionals can coexist in one family.

Those friends who have supported and encouraged me when I needed it the most: Megan Curry who became a dear friend, was always available to talk, was always willing to read something for me and gave generous and valuable feedback, and was insightful during times when I needed to bounce ideas off someone; Kevin Stafford who was a good ideas person, shared his knowledge of caves and resources, and was also generous with his time to read things for me and give valuable feedback; Laura Rosales Lagarde who was always in the office available for bouncing ideas around; and Meriah McKosky who listened when I needed to vent and no one else would listen.

My family who has been integral to the completion of this research: David Kay, my husband, who has stuck with me and supported me through it all; Cherie and Pat

Byrne, my parents, who gave it to me straight even when I did not want to hear it; Shannon Byrne, my sister, who spent countless hours on the phone with me explaining the ins and outs of heat transfer.

Without these special people this research project would not be what it is: a project I am very proud of and excited to share with others.

Table of Contents

List of Tables

Page

List of Figures

Page

List of Symbols

C	heat capacity rate (W/Kelvin)
Const	radiation constant
C_p	specific heat (J/kg·K)
C_{trans}	user defined constant
g	gravitational acceleration for Mars (m/s^2)
Gr	Grashof Number
h	convection heat transfer coefficient ($W/m^2 \cdot K$)
h_{trans}	transversal convective heat transfer coefficient
k	thermal conductivity (W/m·K)
L	characteristic length (m)
m	mass (kg)
Nu	Nusselt Number
Pr	Prandtl Number
q	heat transfer rate (W)
Q	heat source (W)
Q_1	heat transfer (Joule/s)
Q_2	amount of heat given off for a given change in temperature (Joules)
Ra	Rayleigh Number
t	time (s)
T	temperature (Kelvin)
T_0	initial temperature of the material's surface (Kelvin)
T_∞	surrounding air temperature (Kelvin)
T_a	surrounding air temperature (Kelvin)
T_{amb}	ambient temperature (Kelvin)
$T_{ambtrans}$	transversal ambient temperature (Kelvin)
T_f	final temperature (Kelvin)
T_{inf}	ambient bulk temperature (Kelvin)
T_{film}	film temperature (Kelvin)
T_s	surface temperature (Kelvin)
u	velocity field

Greek Letters	
α	thermal diffusivity (m^2/s)
β	volumetric thermal expansion (K^{-1})
μ	viscosity (kg/s·m)
ν	kinematic viscosity (m^2/s)
ρ	density (kg/m^3)

This independent study is accepted on behalf of the
Faculty of the Institute by the following committee:

_____

Advisor: Penelope J. Boston

_____

Phil Kyle

_____

Horton Newsom

_____

Eileen Ryan

_____

Student: Erin K. Kay

_____

Date

Introduction

This study considers the thermal effects of an impact cratering event into the Martian surface using a finite element modeling technique. Further, the environmental, speleological, and potential biological consequences of such an event are explored. A variety of different components of a large impact event were considered in order to constrain possible effects on the surrounding environment. Prior studies (*e.g.* Cockell and Pascal*,* 2002; Rodriguez, *et al.*, 2005; Wrobel, *et al.*, 2005) focused primarily on only one of the many aspects of the problem; however, this study encompasses the following: subsurface and surface composition, material properties of the impact target lithologies, and secondary geological effects (*e.g.* fracturing, release of volatiles, and speleogenesis), and possible implications for any subsurface microbiological communities. This study takes into account adjustments for the Martian surface and subsurface compositions as compared to Earth (

Table 1) as the input parameters for the model. The synthesis of previous studies helped to create a broader understanding of the consequences of an impact event. Data for these analyses came primarily from previous studies and the National Aeronautical and Space Administration (NASA) missions past and present. Surface composition information was acquired from results of the Mars Exploration Rovers (MER), Spirit and Opportunity, currently exploring the Martian areas of Gusev Crater and Meridiani Planum,

respectively, as well as the surrounding areas. Subsurface information is derived from orbiter data such as the Mars Reconnaissance Orbiter (MRO). An assessment from prior literature of potential microorganism types suitable for an environment like a terrestrial crater ecosystem comprised the microbiological aspect of this study.

We hypothesize that the liquid water released as a consequence of an impact event can be a potential mechanism for cave formation in the evaporite and basaltic sequences present on Mars, thus potentially creating a transient surface and subsurface ecosystem for possible microbiological activity. The combination of the calculated Martian geothermal gradient and the heat imparted during an impact event could allow for a temporary surface and subsurface ecosystem to develop capable of supporting microorganisms potentially present on Mars. If the energy associated with an impact event imparts a sufficient amount of heat to result in fluid release, any soluble rock units present could undergo dissolution along fractures (pre-existing or as a result of the impact) within reasonable proximity to the impact site (

Figure 1, part d). This theory is constrained through computer modeling of several impact scenarios into predetermined material compositions. Numerous material compositions and properties were used to simulate different locations on Mars. Follow up analyses of modeling results were then applied to the geologic surroundings as well as any possible microbiology to determine subsequent implications.

	Mars	Earth
Mass (kg)	6.421×10^{23}	5.976×10^{24}
Surface Gravity (m/sec^2)	3.72	9.78
Minimum Temperature (Kelvin)	133	
Mean Temperature (Kelvin)	336	288
Maximum Temperature (Kelvin)	293	
Atmospheric Composition (Mars top 6)		
Carbon Dioxide (%)	95.32	trace
Nitrogen (%)	2.7	77
Argon (%)	1.6	
Oxygen (%)	0.13	29.5
Carbon Monoxide (%)	0.07	trace
Water (%)	0.03	

Chemical Composition of Soil on Mars[1]	
Constituent	Concentration (%)
SiO_2	43.4
Fe_2O_3	18.2
Al_2O_3	7.2
SO_3	7.2
MgO	6.0
CaO	5.8
Na_2O	1.34
Cl	0.8
P_2O_5	0.68
TiO_2	0.6
MnO	0.45
Cr_2O	0.29
K_2O	0.10
CO_3	<2
H_2O	0-1

Table 1: Comparison of Mars and Earth. ([1]reproduced from Kieffer, *et al.,* 1992; Jakosky and Phillips, 2001; Hiscox, 2005; Arnet, 2005)

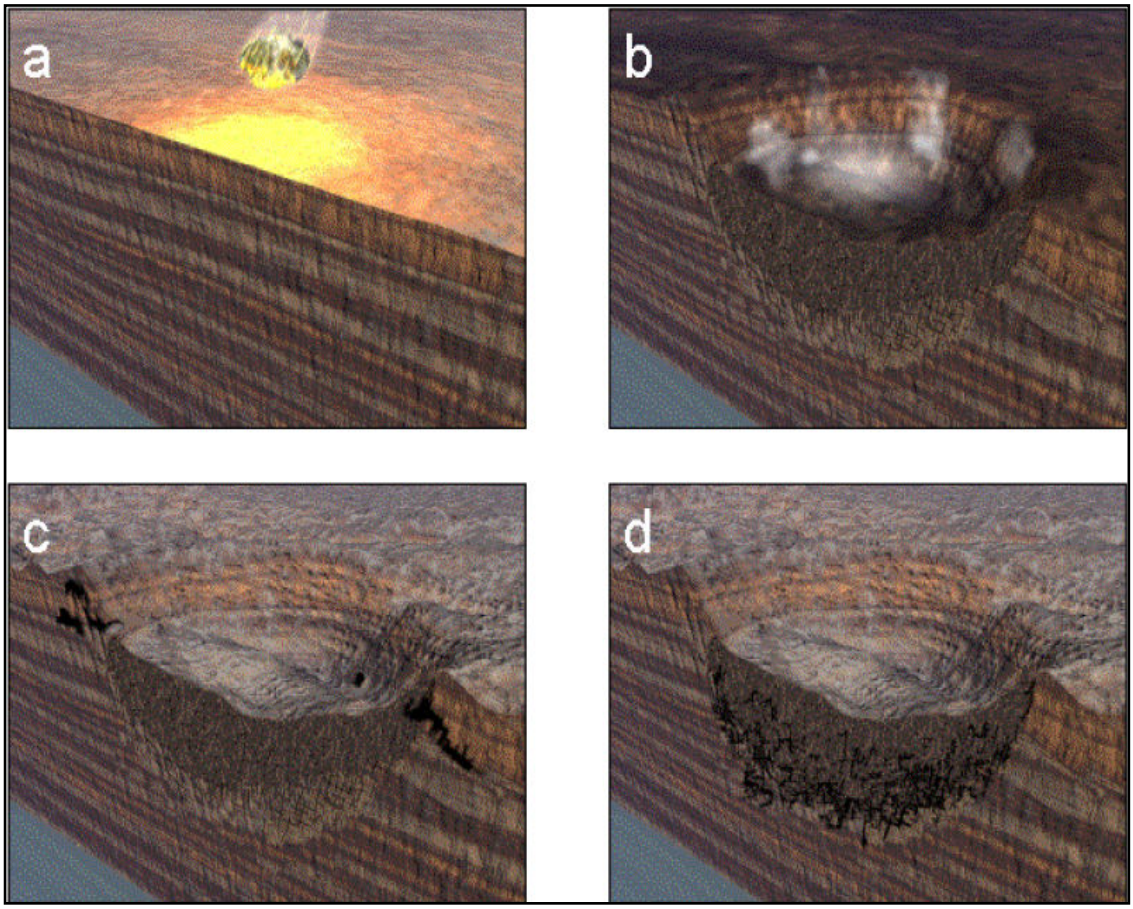

Figure 1: Sequence of impactor events. (a) Impactor approaching Martian surface; surface composed of alternating sediment- and ice-dominated layers. (b) Impact crater forming releasing volatile gases. (c) Within soluble lithologies, fractures widening due to dissolution. (d) Cave formation continuing in deeper layers where heat is retained from impact. Adapted from Johnston, *et al.*, 2006. Graphics © R. D. Frederick 2005.

Background

It is believed that Mars' early planetary history is similar in many regards to that of Earth's (McKay and Stoker, 1989). Surface features on Mars, such as gullies or river channels, indicate past periods of hydrological activity in which liquid water flowed freely on the surface (Jakosky and Phillips, 2001). Jakosky, *et al.* (2005) suggest that crater degradation, high erosion rates, and the presence of valley networks on the oldest surfaces are all evidence for a warmer and wetter Mars. The presence of smectites indicates a Martian hydrologic system with long-term contact with igneous rocks thus producing the smectite clays. This process usually requires a warm, wet environment to accumulate the amounts seen on Mars (Poulet, *et al.*, 2005). Due to Mars' apparent history, it is plausible that Mars had microbiological life sometime during its past (Boston, *et al*., 1992). Microbiology may even be present today in Mars' subsurface; possibly driven there by several factors, including extreme surface temperatures, lack of atmosphere, heavy bombardment of the surface, and high ultraviolet and ionizing radiation intensities (Boston, *et al*., 1992, 2001). One Earth analogy to Mars' possible subsurface geothermal habitats is the Haughton Crater on Devon Island in Canada where evidence of surface and potentially subsurface geothermal habitats have been observed (Cockell and Pascal, 2002).

If Mars was once warm, wet, and had liquid water present at the surface for a period of time (Poulet, *et al.,* 2005; Bullock, 2005; Baker, 2001; Titus, 2004; Paige, 2005; Nisbet and Sleep, 2001), what happened to all this water? The current leading hypothesis is that the water is trapped in a subsurface permafrost layer and/or possibly deeper still as liquid water. This theory is supported by the previous work of

Christensen, *et al.* (2003) that explains the existence of sulfate-rich layers sandwiched between ice-rich layers (Figure 2).

Computer generated simulations and research by Sleep (1994) provides evidence that Mars is still cooling thus creating a geothermal gradient. However, this gradient is only theoretically calculated and has not been measured directly (Zuber, 2001). Consequently, as an impactor hits the Martian surface, it has the potential to penetrate deep into the subsurface fracturing underlying lithologies and permafrost. This allows for subsequent fluid flow and formation of subsurface habitats sustainable for microbiology.

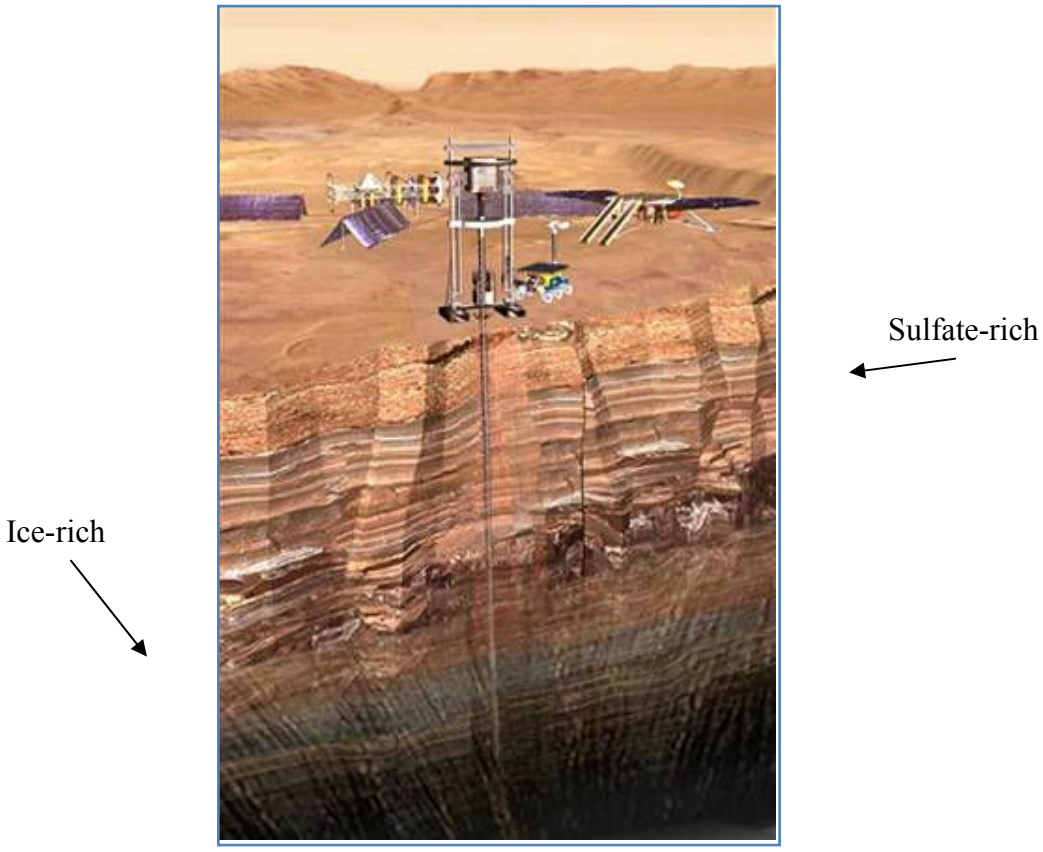

Figure 2: Artists rendition of possible interbedding of sulfate-rich and ice-rich layers on Mars. Image from NASA/JPL.

Surface Composition

In order to impart some realism into the Martian modeling scenarios, we must first establish the likely surface material compositions into which impact events will occur.

Dust particles present in the Martian atmosphere originated from source rocks presumably largely from the surface of Mars. Current findings indicate that wind erosion plays a significant role in the weathering of surface material (Goetz, *et al.*, 2005). Wind erosion abrades surface rocks, thereby facilitating continued rock particle incorporation into the atmospheric dust.

The MERs have collected dust particles that were attracted to filter, capture, and sweep magnets (Goetz, *et al.*, 2005). The filter magnet captured dust particles that were strongly magnetic, while the capture magnet contained dust particles with a wide range of magnetic properties. The sweep magnet acquired only non-magnetic particles (Goetz, *et al.*, 2005) that were blown in by wind. An analysis of these particles indicated that the dust is composed of magnetite, olivine, pyroxene (Goetz, *et al.,* 2005), goethite, and hematite (Yen, *et al*, 2005). Other elements have also been identified in these particles, including aluminum, calcium, iron, potassium, magnesium, sodium, silicon, and titanium (Goetz, *et al.,* 2005).

Gypsum has also been identified in the north polar region of Mars as part of the polar dune sea (Fishbaugh, *et al.*, 2007). Fishbaugh, *et al*. (2007) attribute the presence of gypsum in these dunes to a combination of the pore space evaporation of gypsum crystals and the direct alteration of sulfide- and high -calcium-pyroxene containing dunes. Also note that a gypsum deposit of this kind has not been found anywhere else, nor has

gypsum been found in association with any other dunes on Mars (Fishbaugh, *et al*., 2007). However, other sulfates have been found in abundance in other locations on Mars (Newsom, 2005; Golden, *et al..,* 2005).

Six major constituents have been identified in the surface soils of Mars at Gusev Crater and Meridiani Planum. Gusev revealed bright dust, dark soil, bedform armor (rounded, millimeter sized grains that are well sorted that create a protective layer on the lithology), and lithic fragments, while Meridiani Planum revealed the same bright dust and dark soil with the addition of spherules (apparent concretions named "blueberries"), and clasts (Yen, *et al*., 2005). Using on-board instrumentation on MER's Spirit and Opportunity, an *in situ* analysis of the soils was performed (Yen, *et al*., 2005). The bright dust composition was determined to be several primary minerals including olivine, magnetite, and pyroxene. Less abundant were secondary minerals including oxidized crystallites and nanocrystallites of ferric iron (Goetz, *et al*., 2005). The dark soil is composed primarily of olivine and pyroxene with other elements including iron (Yen, *et al.,* 2005). The bedform armor has magnetite-rich millimeter sized grains that are believed to originate from the basaltic plains surrounding the lander sites. This belief is based on the sample's enrichment in calcium, chromium, and iron and its depletion in chlorine, potassium, sulfur, nickel, titanium, and zinc (Yen, *et al.,* 2005). The lithic fragments are similar in composition to the bedform armor, however the fragments had larger grain sizes (Yen, *et al.,* 2005). The spherules are hematite-rich with an abundance of millimeter-sized grains of nickel and iron (Yen, *et al.,* 2005). The clasts are subangular and vesicular in nature (Yen, *et al.,* 2005). Results from the atmospheric dust particles and soil composition studies reveal that both the spherules and clasts are of

similar origins. The surface layers on Mars are assumed to be the primary contributor to the dust, thus representative of the variety of materials seen in the dust particles (Yen, *et al.,* 2005). Therefore material properties can be reasonably inferred based on the dust composition and used in the models.

Subsurface Composition

The bulk surface composition of Mars is generally assumed to be chondritic (Zuber, 2001). This assumption is based on meteorite compositions believed to be Martian in origin in conjunction with density distribution with depth models (Zuber, 2001). For potential microbiological subsurface habitats under investigation, two categories of rock are being considered: evaporites/carbonates and volcanic basalts. The evaporites (*e.g.* gypsum, sodium sulfates, etc.) and carbonates are potentially in thick sequences and highly soluble, which potentially could support large caves. The presence of thick carbonate sequences on Mars has not yet been proven; however, small amounts of carbonates have been found in Martian meteorites (Lindsay and Brasier, 2006; Wentworth, *et al.*, 2002) and in surface dust (Fairén, *et al.,* 2004). It has been argued that any carbonates on Mars would have precipitated early in Mars' history and may exist in thick sequences overlain by other lithologies such as volcanic and other evaporite sequences and thus not detectable by remote methods (Manning, *et al.*., 2006). Sulfates (*e.g.* gypsum, anhydrite, and jarosite) and phyllosilicates (*e.g.* clay minerals, smectites, and kaolin-serpentines) have also been identified on Mars (Bishop, 2005; Golden, 2005; Newsom, 2005; Poulet *et al.*, 2005). Some of the minerals included in this category are halite, brucite, and apatite (Bishop, 2005; Tosca and McLennan, 2006). Due to the high

solubility of evaporites and carbonates, such lithologies could support the formation of large cavernous bodies that have been dissolved.

Also considered as a type of speleogenesis (cave formation origin) were both the subsequent dissolutional widening of fractures and the melting and release of a permafrost layer due to released heat energy during an impact event. Once fractures are formed as a result of an impact, liquid water travels through the fractures dissolving the host rock thus enlarging the fractures to produce macroporosity including caves.

Volcanic sequences, such as basalt, are theorized to be very thick deposits on Mars over a great deal of the planet's surface. Volcanics are considerably less soluble than carbonates and evaporites, thereby hosting potentially smaller caves (possibly not much more than fractures) and influenced more by hydrothermal water-rock interactions (Haskin, *et al.*, 2005). Caves formed in basalt would likely be constructional due to the force of an impact event rather than the solutional counterparts that would be present in evaporites and carbonates (White, 1988). For example, pre-existing lava tubes may simply be modified and/or breached as a result of an impact cratering event. Table 2 illustrates the different formation processes in different types of caves.

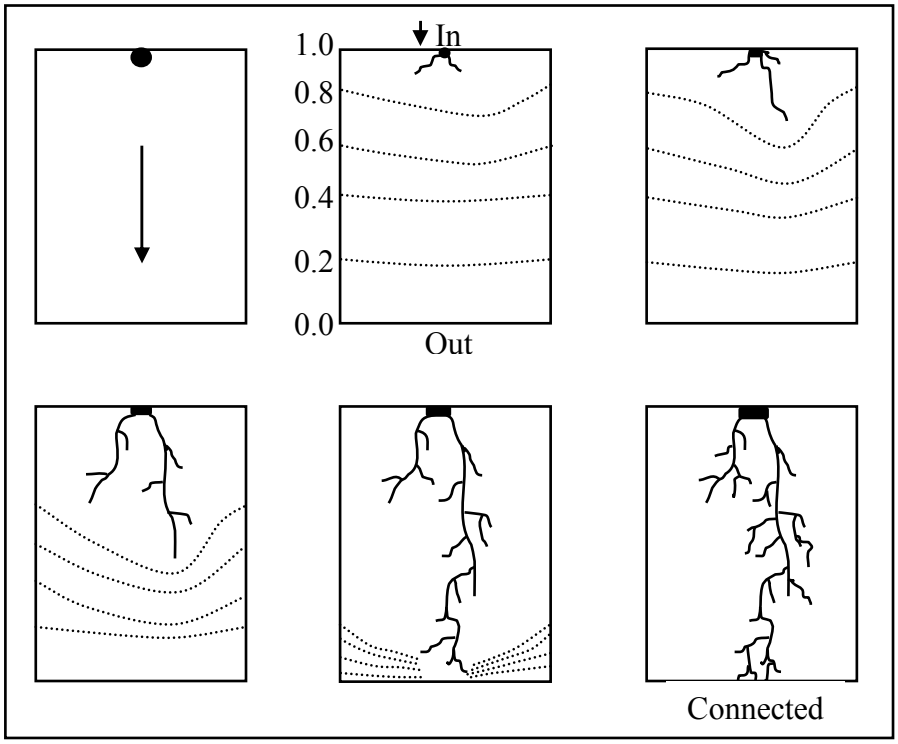

Figure 3: An over-simplification of the propagation of a single point fracture into a protocave. The dashed lines are equipotentials. The "In" and "Out" represent the input and output points, respectively. Reproduced from Ford, 1988.

Cave formation strongly dependent on composition of host rock and formation driven primarily by chemical processes		
Type of Cave	*Process*	*Optimum host rock*
Solutional Caves	**Chemical solution of rock**	**Soluble rocks such as limestone, dolomite, and gypsum**
Lava Caves	**Freezing of wall rock around channel**	**Pahoehoe basalts**
Ice Caves	Melting of ice along channel	Glacial ice
Cave formation independent of host rock composition and formation driven primarily by mechanical processes		
Type of Cave	*Process*	*Optimum host rock*
Aeolian Caves	Scour by wind-driven sand	Massive sandstone, loosely cemented
Sea Caves	Scour by wave action on sea cliffs	Massive rock with well developed jointing
Tectonic Caves	Bulk movement of rock mass	Any rock; good jointing and lubricating beds
Suffosion caves	Soil piping	Fine-grained, poorly consolidated sediments
Erosion caves	Erosion and slumping	Alternating resistant and nonresistant beds
Talus caves	Pileup of boulders	Massive rocks

Table 2: Cave classification. Cave types highlighted in black are focused on in this research. Reproduced from White, 1988.

Evaporite and Carbonate Caves

Karst and cave formation in evaporite (*e.g.* gypsum, anhydrite, and halite) and carbonate (*e.g.* limestone and dolomite) sequences are common on Earth, thus, we believe that similar environmental conditions on Mars have the potential to create similar cavernous porosity. In this study, we take an in-depth look at the formation of caves into three different soluble lithologies: gypsum, halite, and limestone. We can surmise that the presence of gypsum/anhydrite, also known collectively as sulfates (Klimchouk and Andrejchuk, 1996), in the subsurface of Mars is probable, given the existence of sulfates on the surface. One of the Mars rovers, *Opportunity*, found what is believed to be a sulfate rock on the surface (Klingelhöfer, *et al.*, 2004; Christensen, *et al*., 2004; Kerr, 2004). However, due to the nature of the rovers' instrumentation it was not determinable the depth to which this rock type may exist. The presence of sulfate rock on the surface may also indicate the presence of sulfate at depth (Stafford and Boston, 2005). Supported by little scientific evidence, the presence of carbonates and evaporites in large sequences on Mars is still heavily debated.

Both the dissolutional and mechanical formation of caves is similar in both the lithologies considered here. The impact event itself could provide the kinetic energy necessary for the creation or enlargement of fractures in the surrounding rock. The water released due to the transfer of heat energy during an impact cratering event could enable the dissolutional process. In order for cave networks to form, bedrock heterogeneity must be present. This heterogeneity can be in the form of a pre-existing fracture network (Palmer, 1991), bedding planes, or slight compositional variations in the lithology. Palmer (1991) suggests that dissolution rates for limestone caves formed epigenically

(*e.g.* formed by fluid input from precipitation or shallow ground water) on Earth are approximately 10-100 mm per thousand years; however, this rate can be significantly higher based on fluid composition. A source of very undersaturated waters, with respect to the dominant mineral in the lithology, can greatly speed the dissolution process. Since there is no known surface precipitation to speed the dissolution process on Mars, this Earth-derived estimation is likely to be far faster than actual Martian dissolution rates for any epigenic process even in Mars' wetter ancient past. Thus, the probability that human traversable epigenic caves exist on Mars is low due to the likely lack of an active hydrologic cycle for a geologically significant period of time. There could, however, be smaller dissolutional caves, essentially small vugs, adequate to house any possible microbiological life. Dissolution could occur episodically with the occasional release of subsurface fluids by mechanisms other than the impact processes described here.

Basaltic Caves

Cave formation in basaltic terrains is different than the carbonate and evaporite terrains, thus the implications are also different. Basaltic cave formation is generally associated with primary processes such as lavatube formation and lava cooling and fracturing via mechanical processes. Basaltic caves are poorly associated with dissolution and erosive forces. The solutional kinetics of basaltic caves is not well understood, in contrast to carbonate and evaporite caves. Kempe and Werner (2003) report that Kuka'iau Cave in Mauna Kea, Hawaii is erosional in origin. They made this suggestion based on the absence of typical lava tube morphology, such as secondary ceilings, lava falls, and lava stalactites (Kempe and Werner, 2003; Kempe, *et al*., 2003). The presence

of several right angle turns along the length of the cave as well as geological evidence of erosional features down through underlying lava layers confirms this cave is erosional in origin (Kempe and Werner, 2003). Based on this evidence, it seems unlikely for dissolutionally enhanced basaltic caves to form on Mars through erosion alone given the lack of a suitable erosional force such as liquid water at least in relatively recent times.

Extreme Earth Environmental Analogs for Microbiological Implications on Mars

Caves have the potential to house an enormously diverse ecosystem. On Earth, there are organisms that live their entire life cycle within a cave and never see sunlight (Palmer, 2007). Through evolutionary adaptations, they are able to thrive in such environmental conditions. The nutrients for these organisms can come from a number of sources, including: organic debris carried in by animals and/or flood waters, roots from surface plants invading shallow caves, and organic material blown in by surface winds (Palmer, 2007). However, there is no evidence to date that plant or animal life has ever existed on the surface of Mars, and indeed, organic compounds themselves seem to be actively destroyed in the modern Mars atmosphere (Biemann, *et al..,* 1977). There is evidence of liquid water being present in the past on the surface of Mars (Jakosky and Phillips, 2001; Bullock, 2005), but it is presumed that the water does not last long before it sublimates due to low atmospheric pressures and surface air temperatures below the triple point for water, thus it is unlikely that water borne nutrients could percolate into such systems. Therefore, the most plausible way nutrients from surface sources could be introduced into a subsurface void is through wind blown processes into a surface entrance to the subsurface cavity. However, it has been suggested that a subsurface Martian

microbiota could be driven by entirely non-organic materials in the form of subsurface gas percolation of chemically reduced gases from the deeper layers of the planet or from mining oxidizable energy sources from the bedrock itself (Boston, *et al..,* 1992).

It has been suggested that acidic waters once existed on Mars (Benison and Laclair, 2003), allowing for potential acidophiles to exist in an environment similar to those found on Earth that harbor such organisms. Cavicchioli (2002) states that extremophiles exist in atypical locations such as a nuclear reactor core and within toxic wastes, habitats not previously thought inhabitable. These previous studies are a few examples of the various extreme environments on Earth that microorganisms are able to inhabit that were once thought uninhabitable. Such Earth analogs can be applied to the present and past extreme environmental conditions on Mars. If caves exist on Mars they could potentially be habitable for microbiological organisms present on Mars assuming the nutrients to support such microorganisms are present.

Modeling an Impact Cratering Event

Introduction

Computer modeling inspired by some of the MER compositional data was used to determine the outcome of an extraterrestrial object impacting into different surface lithologies including those underlain by permafrost. Modeling was done using finite element-based computer modeling software: COMSOL Multiphysics version 3.3. The multiphysics heat transfer through convection and conduction module in COMSOL was used to determine the heat energy transferred during an impact event. The built-in solve equations were implemented. Appropriate material properties for the target site, including the surface and subsurface, as well as two different depths and thicknesses of underlying permafrost were used as model input parameters. The details of the COMSOL software are included in Appendix A.

Crater and Ejecta Blanket Scaling

Crater and ejecta blanket scaling was necessary in order to account for the various impact crater sizes. A large impact crater would presumably produce a thicker ejecta blanket because a greater amount of material is mobilized in some proportion to the total energetics of the impact event. Thus, larger events with thicker ejecta blankets will take a longer time to cool compared to thinner ejecta blankets around smaller impact events.

Melosh (1989) states that the ejecta blanket is thicker near the crater and thins as the distance from the crater center increases (Figure 5). Unsurprisingly, Horedt and Neukum (1984) determined that the larger the mass of an impactor, the larger the crater diameter. This is also evident in Table 3 compiled by Melosh (1989).

	Transient Crater Diameter (kilometers)		
Projectile Diameter	Yield Scaling (1962)	Gault (1974)	Schmidt (1987)
1 m	0.034	0.028	N/A
10 m	0.26	0.21	0.38
100 m	2.0	1.1	2.3
1 km	16.0	7.6	14.0
10 km	120.0	53.0	84.0
100 km	975.0	364.0	510.0

Table 3: Final crater diameter for an Earth-based impactor with a velocity of 20 km/sec for three different crater scaling laws. Reproduced from Melosh 1989.

Melosh (1989) also points out that the determination of the impact energy based on crater size is an imprecise calculation. This is evident in the difference in calculations in the previous table (Table 3), especially for larger projectile/crater diameters. There is a factor of three difference in the crater diameter size for a 100 km diameter projectile, thus the determination of the energy imparted can not be accurately calculated based on this type of evidence alone.

An ejecta blanket created as a result of an impact cratering event decays exponentially in thickness with distance from the crater rim. Housen, *et al.* (1983) calculated the variation of ejecta blanket thickness with distance from an impact crater rim. Their predicted values correspond well with their experimental results. Figure 4 clearly illustrates ejecta blanket thinning as a function of distance from the crater. This

figure also shows the well-correlated calculated and experimental values. This leads to the resulting morphology illustrated in Figure 5 based on Melosh's (1989) work.

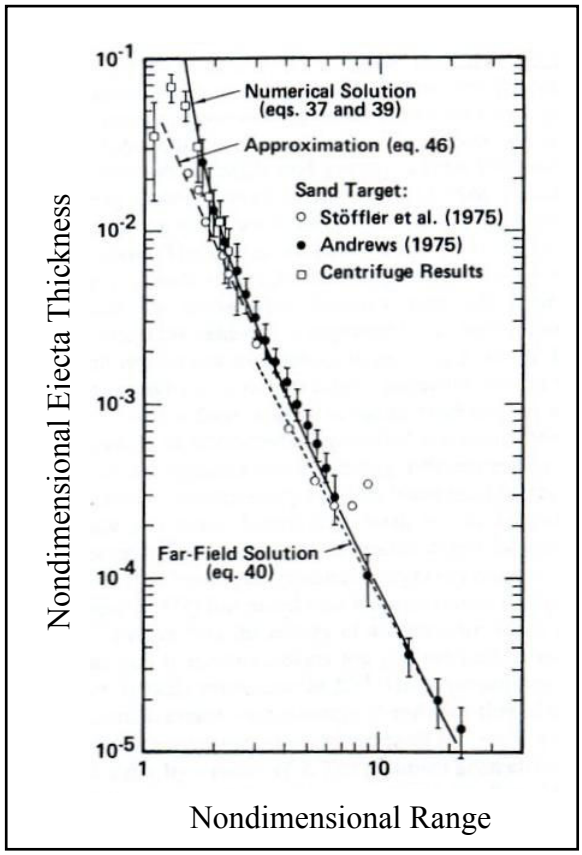

Figure 4: Graph illustrating the correlation between the calculated (numerical solution) and experimental (approximation) ejecta blanket thicknesses. The calculated solutions are based on the ejecta scaling model; the experimental results are based on explosions in sand, both discussed in Housen, *et al.* (1983). Modified from Housen, *et al.* (1983).

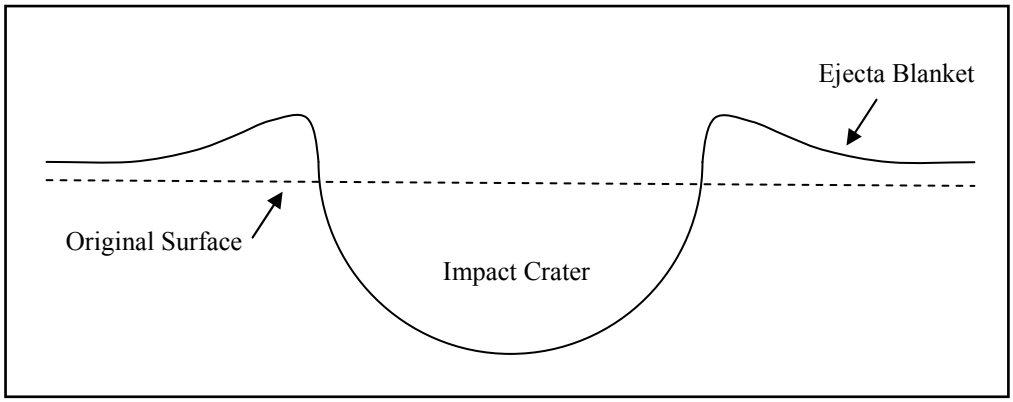

Figure 5: Resulting impact crater morphology based on Melosh (1989). Diagram also illustrates the results by Housen, *et al.* (1983) illustrated in the previous figure.

In this research, there are three impact sizes discussed: small, medium, and large. We emphasize that this size designation is based solely on the impact temperatures used in the modeling process, thus the size designations are a reflection of the size of the amount of energy imparted and cannot be directly related to the physical size of the crater in this study. There are so many variables that impinge on the physical diameter of actual impact craters that, for this study, relative energy is a more meaningful way to understand the processes. For example, incident angle of the impactor, density and physical structure of the impactor, impact velocity, and specific properties of the impacted materials all play a part in the precise shape and size of the resulting feature (Schultz, 1992; Pierazzo and Melosh, 2000).

Table 4 illustrates the correlation between the size and corresponding temperatures for each of the five lithologies. The physical size of the stratigraphic column considered is also in the small/medium/large designations.

Table 5 shows this relationship. These designations were based on the physical material properties for each lithology (*e.g.* melting temperatures and material property values available in current literature).

	Small Impact	Medium Impact	Large Impact
Basalt	1250	3750	7500
Epsomite	500	1500	3000
Gypsum	250	1750	-
Halite	1250	1500	-
Limestone	500	-	-

Table 4: Table shows the temperature (in degrees Kelvin) correlations with impact size designations.

	Small Impact	Medium Impact	Large Impact
All lithologies	40 m wide 20 m deep	120 m wide 60 m deep	240 m wide 120 m deep

Table 5: Table shows stratigraphic size used in models in relation to the impact size designations.

Cooling Rates

The cooling rate for lithologies used was determined by the following three equations:

$$Q_1 = hA\left(T_0 - T_a\right), \qquad \text{Equation 1}$$

$$Q_2 = mC\Delta T, \qquad \text{Equation 2}$$

$$t = \frac{Q_2}{Q_1}, \qquad \text{Equation 3}$$

where Q_1 is the heat transferred; A is the surface area in contact with the surrounding air; T_0 is the temperature of the rock's surface; T_a is the temperature of the surrounding air; Q_2 is the amount of heat given off for a given ΔT; m is the mass of the entire piece of

rock; ΔT is the change in temperature; and t is the time required for the rock to cool down based on the given ΔT. The seconds are converted to years using the following values: for Earth, 23.94 hours per day and 365.24 days per year; for Mars, 24.6 hours per day and 686.98 days per year. With these conversion values, the cooling rates for the different lithologies including the ejecta blankets are illustrated in the following tables (Table 6 - Table 13). The models whose impact temperatures were equal to or less than 500 degrees Kelvin were given a final temperature of zero degree Kelvin. This temperature range was assigned in order to demonstrate the heat propagation through the lithology. Table 9 illustrates the cooling rates for all the lithologies to zero degrees Kelvin, however, the models that used a zero degree Kelvin final temperature were the small impact size for epsomite, gypsum, and limestone all other models used 336 degrees Kelvin as a final temperature.

Lithology	Impact Size	T_o (K)	Years to cool to 400K	
			Earth	Mars
Basalt	small	1250	1.45	0.77
	medium	3750	4.60	2.37
	large	7500	9.29	4.80
Epsomite	small	500	4.72	2.44
	medium	1500	22.01	11.38
	large	3000	45.45	23.51
Gypsum	small	250	-	-
	medium	1750	1.92	0.99
Halite	small	1250	2.99	1.55
	medium	1500	2.77	1.43
Limestone	small	500	1.65	0.86

Table 6: Time in years (both Earth years and Martian Sols) that it will take for the materials to cool down to 400 degrees Kelvin from the given starting temperatures.

Lithology	Impact Size	T_o (K)	Years to cool to 350K	
			Earth	Mars
Basalt	small	1250	1.53	0.79
	medium	3750	4.67	2.41
	large	7500	9.35	4.84
Epsomite	small	500	7.08	3.67
	medium	1500	23.01	11.90
	large	3000	46.33	23.96
Gypsum	small	250	-	-
	medium	1750	1.99	1.03
Halite	small	1250	3.16	1.64
	medium	1500	2.89	1.50
Limestone	small	500	2.48	1.29

Table 7: Time in years (both Earth years and Martian Sols) that it will take for the materials to cool down to 350 degrees Kelvin from the given starting temperatures.

Lithology	Impact Size	T_o (K)	Years to cool to 336K	
			Earth	Mars
Basalt	small	1250	1.56	0.81
	medium	3750	4.69	2.42
	large	7500	9.37	4.85
Epsomite	small	500	7.74	4.01
	medium	1500	23.29	12.04
	large	3000	46.57	24.09
Gypsum	small	250	-	-
	medium	1750	2.01	1.04
Halite	small	1250	3.21	1.67
	medium	1500	2.92	1.52
Limestone	small	500	2.71	1.41

Table 8: Time in years (both Earth years and Martian Sols) that it will take for the materials to cool down to 336 degrees Kelvin (ambient temperature) from the given starting temperatures.

Lithology	Impact Size	T_o (K)	Years to cool to 325K	
			Earth	Mars
Basalt	small	1250	1.58	0.82
	medium	3750	4.70	2.43
	large	7500	9.39	4.85
Epsomite	small	500	8.26	4.28
	medium	1500	23.51	12.15
	large	3000	46.77	24.19
Gypsum	small	250	-	-
	medium	1750	2.03	1.05
Halite	small	1250	3.25	1.69
	medium	1500	2.95	1.53
Limestone	small	500	2.90	1.50

Table 9: Time in years (both Earth years and Martian Sols) that it will take for the materials to cool down to 325 degrees Kelvin from the given starting temperatures.

Lithology	Impact Size	T_o (K)	Years to cool to 300K	
			Earth	Mars
Basalt	small	1250	1.62	0.84
	medium	3750	4.73	2.45
	large	7500	9.42	4.87
Epsomite	small	500	9.44	4.98
	medium	1500	24.01	12.41
	large	3000	47.20	24.41
Gypsum	small	250	-	-
	medium	1750	2.06	1.07
Halite	small	1250	3.34	1.73
	medium	1500	3.02	1.56
Limestone	small	500	3.31	1.72

Table 10: Time in years (both Earth years and Martian Sols) that it will take for the materials to cool down to 300 degrees Kelvin from the given starting temperatures.

Lithology	Impact Size	T_o (K)	Years to cool to 0K	
			Earth	Mars
Basalt	small	1250	2.14	1.10
	medium	3750	5.15	2.66
	large	7500	9.81	5.07
Epsomite	small	500	23.67	12.24
	medium	1500	30.01	15.52
	large	3000	52.45	27.13
Gypsum	small	250	6.05	3.13
	medium	1750	2.50	1.29
Halite	small	1250	4.41	2.28
	medium	1500	3.78	1.95
Limestone	small	500	8.30	4.29

Table 11: Time in years (both Earth years and Martian Sols) that it will take for the materials to cool down to zero degrees Kelvin from the given starting temperatures.

	T_o (K)	Yrs to 400K	Yrs to 350K	Yrs to 336K	Yrs to 325K	Yrs to 300K
Basalt	1250	0.36	0.38	0.39	0.40	0.41
Epsomite	1250	1.80	1.19	1.94	1.96	2.02
Gypsum	1250	0.47	0.50	0.50	0.51	0.52
Halite	1250	0.75	0.79	0.81	0.82	0.84
Limestone	1250	0.63	0.67	0.68	0.69	0.71

Table 12: Time in Earth years for an ejecta blanket of uniform thickness, composed of the materials listed here, to cool from the initial temperature of 1250 degrees Kelvin to the final temperatures (in Kelvin) also listed.

	T_o (K)	Yrs to 400K	Yrs to 350K	Yrs to 336K	Yrs to 325K	Yrs to 300K
Basalt	1250	0.19	0.20	0.20	0.20	0.21
Epsomite	1250	0.93	1.00	1.00	1.02	1.04
Gypsum	1250	0.24	0.26	0.26	0.26	0.27
Halite	1250	0.39	0.41	0.42	0.42	0.43
Limestone	1250	0.33	0.35	0.35	0.36	0.37

Table 13: Time in Mars years for an ejecta blanket of uniform thickness, composed of the materials listed here to cool from the initial temperature of 1250 degrees Kelvin to the final temperatures (in Kelvin) also listed.

Model Example - Basalt

The basalt models will be used as a detailed example to demonstrate how COMSOL was implemented to obtain the results. Other materials were simulated using the same exact procedure. The basalt models were chosen as the example due to the clear evidence of widespread basaltic sequences on Mars. The impact cratering models are first, followed by the ejecta blanket model. Three different sized impact situations were simulated impacting into five different stratigraphic column examples. Only the small impact size situations will be shown here for all five stratigraphic column examples. All modeling results are found in Appendix C, including impact scenarios and ejecta blanket simulations for all three impact sizes and all five lithologies.

This first COMSOL generated image shows a homogeneous basaltic stratigraphic column. This scenario was modeled to obtain a baseline for the propagation of heat through a simple uniform lithology with no interference from a subsurface permafrost layer. This image illustrates the depth to which the impact heat penetrates within the stratigraphic column. The horizontal axis is the distance in meters from the center of the impact site, while the vertical axis is the depth from the surface. The temperature legend on the right is color-coded to match the colors in the model pictured. The light blue contours show temperature (Kelvin) intervals; the specific contour interval temperatures are given in the figure caption. The contours at the bottom indicate the cooler temperatures while the contours at the top indicate the hotter temperatures. The vertical black lines seen in the model are artifacts of the modeling process and in no way affect the results.

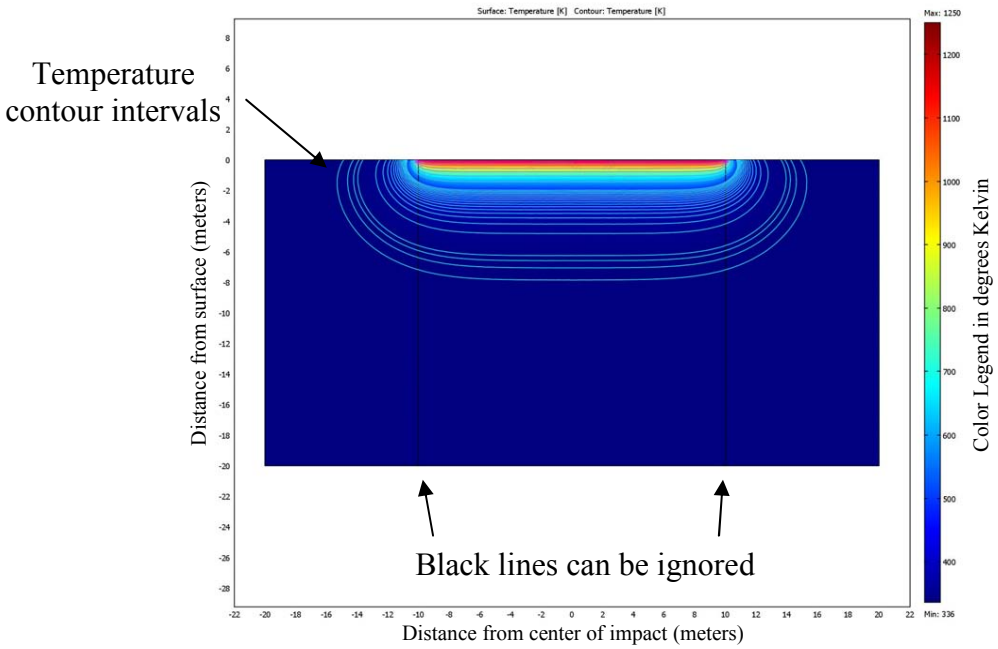

Figure 6: COMSOL generated image of a homogeneous basalt stratigraphic column. The basalt layer is 20 meters thick. The vertical black lines can be ignored and in no way effect the resulting model.

Contour Intervals: 1200, 1100, 1000, 900, 800, 700, 600, 500, 490, 480, 470, 460, 450, 440, 430, 420, 410, 400, 390, 380, 370, 360, 350, 340, 339, 338, 337, 336

Once the baseline was established and a comparison could be made with the other models, a permafrost layer was added to the stratigraphic column. The next four figures illustrate the four different scenarios involving a permafrost layer at depth. The first figure is a COMSOL generated image illustrating how a thin, near-surface permafrost layer affects the depth to which heat energy imparted by the impact event penetrates into the stratigraphic column. The horizontal and vertical axes are the same as in Figure 6 above. In Figure 7 the vertical black lines above and below the permafrost layer can be ignored. The horizontal black lines indicate the contact boundary between the basalt and

permafrost layers. Also note that the presence of the permafrost layer allows the heat generated during the impact event to propagate deeper into the stratigraphic column.

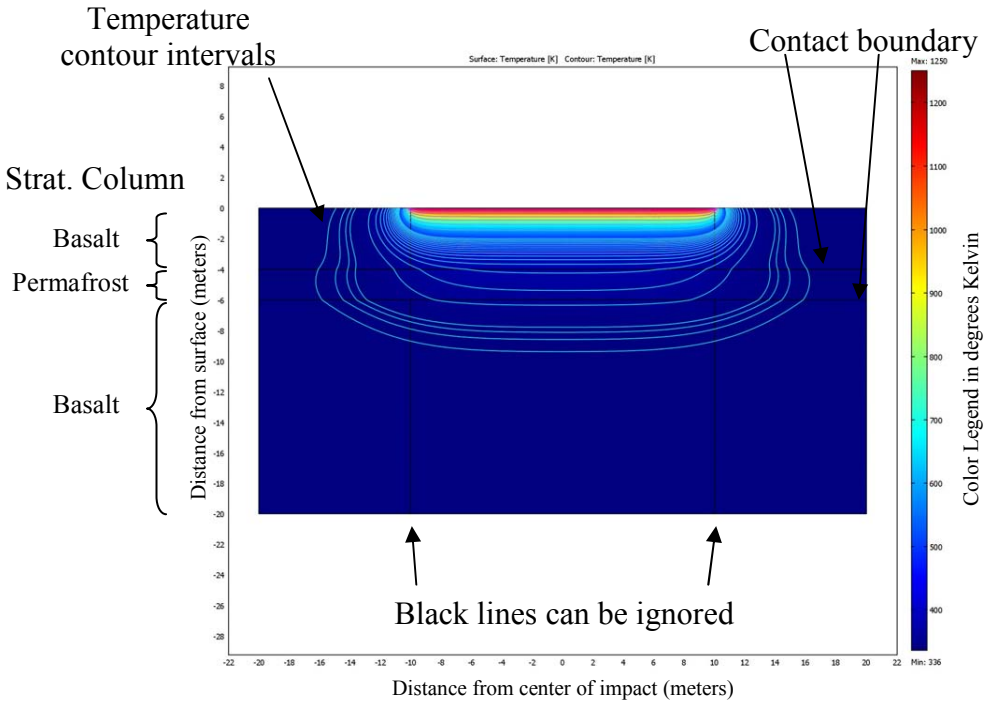

Figure 7: COMSOL generated image of a basalt, permafrost, basalt stratigraphic column. The permafrost layer is 2 meters thick at a depth of 4 meters. The vertical black lines can be ignored and in no way effect the resulting model. The horizontal black lines indicate the contact boundary between the basalt and permafrost layers.

Contour Intervals: 1200, 1100, 1000, 900, 800, 700, 600, 500, 490, 480, 470, 460, 450, 440, 430, 420, 410, 400, 390, 380, 370, 360, 350, 340, 339, 338, 337, 336

The second COMSOL generated image, shows the effect of a thin permafrost layer deeper in the stratigraphic column. The depth of heat penetration in Figure 8 differs from Figure 7 because of the permafrost layer is deeper in the stratigraphic column. The depth to which the heat propagates is similar to that of Figure 6.

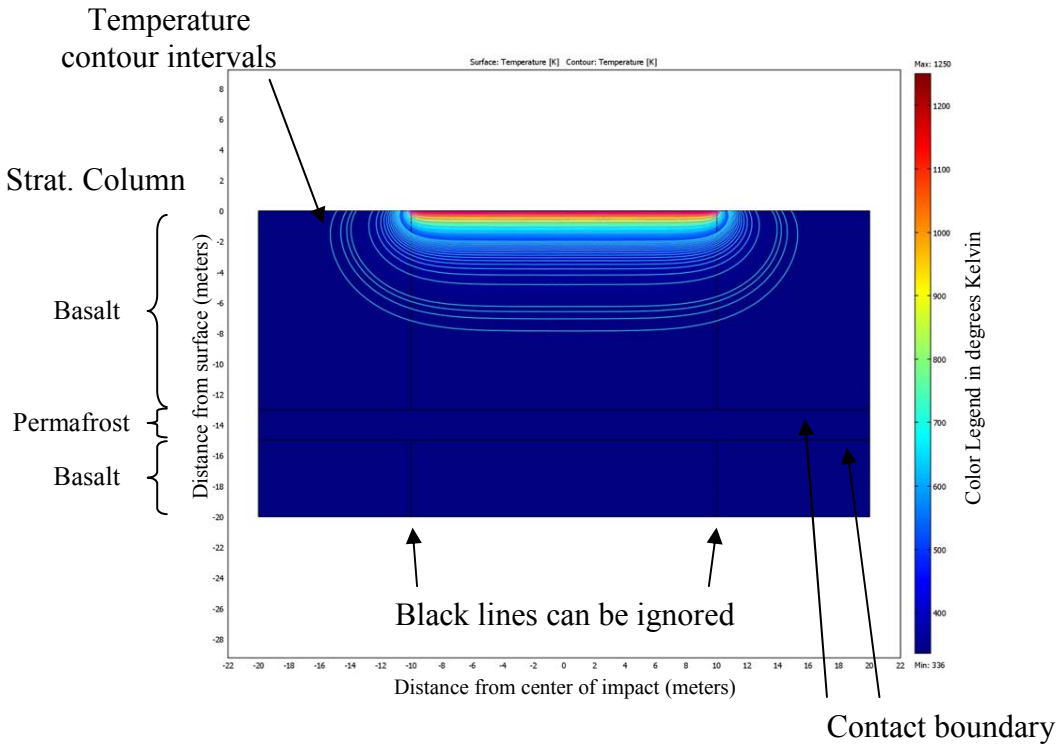

Figure 8: COMSOL generated image of a basalt, permafrost, basalt stratigraphic column. The permafrost layer is 2 meters thick at a depth of 13 meters. The vertical black lines can be ignored and in no way effect the resulting model. The horizontal black lines indicate the contact boundary between the basalt and permafrost layers.

Contour Intervals: 1200, 1100, 1000, 900, 800, 700, 600, 500, 490, 480, 470, 460, 450, 440, 430, 420, 410, 400, 390, 380, 370, 360, 350, 340, 339, 338, 337, 336

The third figure, also a COMSOL generated image, shows the effect of a thick, near-surface permafrost layer in the stratigraphic column. The presence of a thick, near-surface permafrost layer has a similar effect as a thin, near-surface permafrost layer in that the layer aids in the propagation of heat through the stratigraphic column.

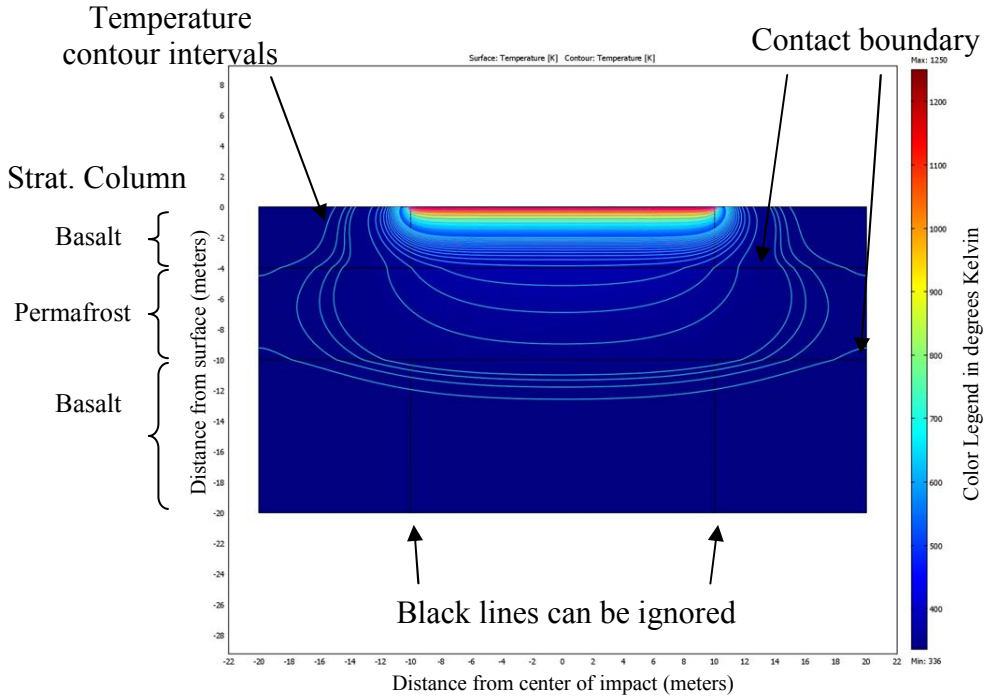

Figure 9: COMSOL generated image of a basalt, permafrost, basalt stratigraphic column. The permafrost layer is 6 meters thick at a depth of 4 meters. The vertical black lines can be ignored and in no way effect the resulting model. The horizontal black lines indicate the contact boundary between the basalt and permafrost layers.

Contour Intervals: 1200, 1100, 1000, 900, 800, 700, 600, 500, 490, 480, 470, 460, 450, 440, 430, 420, 410, 400, 390, 380, 370, 360, 350, 340, 339, 338, 337, 336

The fourth COMSOL figure shows the effect of a thick permafrost layer deeper in the stratigraphic column. As with the thin permafrost layer at depth (Figure 8) a thicker permafrost layer at depth also seems to have a minimal effect on the depth to which the heat propagates because it is beyond the influence of the event.

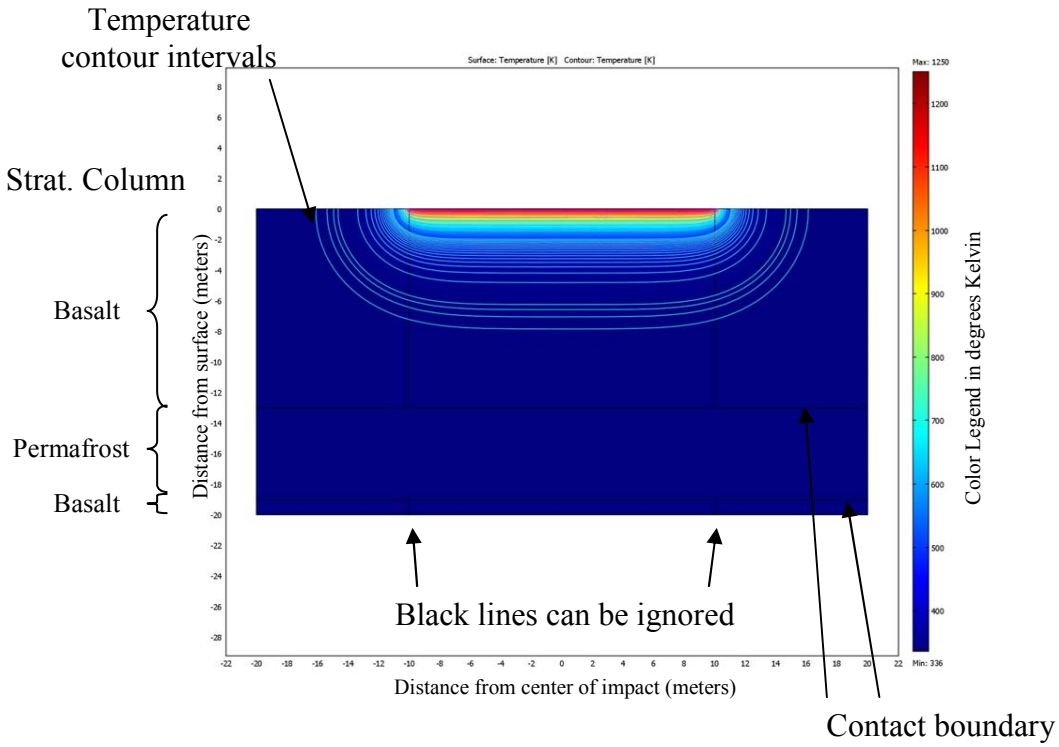

Figure 10: COMSOL generated image of a basalt, permafrost, basalt stratigraphic column. The permafrost layer is 6 meters thick at a depth of 13 meters. The vertical black lines can be ignored and in no way effect the resulting model. The horizontal black lines indicate the contact boundary between the basalt and permafrost layers.

Contour Intervals: 1200, 1100, 1000, 900, 800, 700, 600, 500, 490, 480, 470, 460, 450, 440, 430, 420, 410, 400, 390, 380, 370, 360, 350, 340, 339, 338, 337, 336

The comparison of these five models indicates that not only does the depth of a permafrost layer play a role, but the thickness of a permafrost layer also plays a vital role in the depth to which heat energy penetrates into the stratigraphic column.

The next step of the modeling process involved an ejecta blanket created as a result of an impact event. The following COMSOL generated image shows the transfer of heat from the ejecta blanket into the underlying bedrock as well as the cooled ejecta blanket material above the heated ejecta blanket. The temperature contour intervals for the ejecta blanket figure radiate from the heated ejecta blanket material into the cooler

basaltic material above and below. This makes the higher temperature contours in the center of the figure with the contours cooling toward the top and bottom of the figure, differing from the previous figures contour intervals.

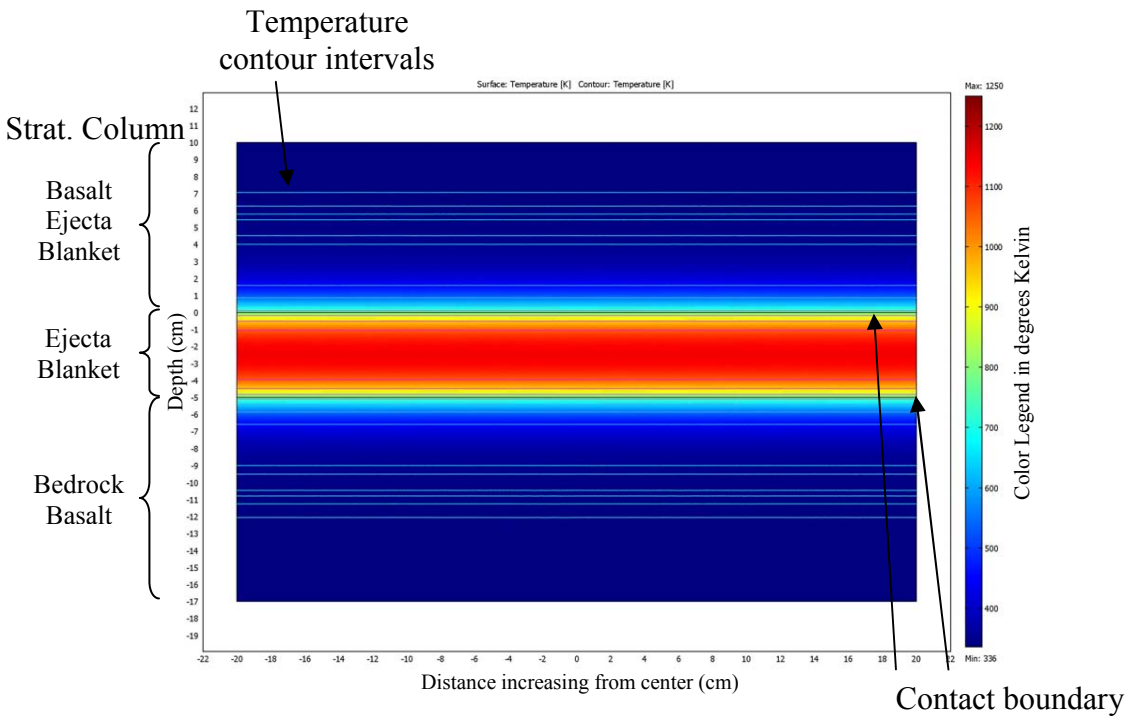

Figure 11: COMSOL generated image of a basalt ejecta blanket. The stratigraphic column is basalt ejecta blanket, heated basalt ejecta blanket, basalt bedrock. The horizontal black lines indicate the contact boundary between the (top to bottom) cool ejecta blanket, heated ejecta blanket, and bedrock. This figure illustrates the propagation of heat through the bedrock as well as the overlying ejecta blanket that has been deposited cold rather than heated.

Contour Intervals: 1150, 1050, 950, 850, 750, 650, 550, 450, 350, 345, 340, 339, 338, 337

Effect of Permafrost Layer

Because basalt was not the only lithology modeled and due to the several impact sizes simulated, there is a plethora of information that was attained from the modeling process. Those direct results can be seen in Appendix C. However for greater clarity, the

following graphs are included to better illustrate a summarized interpretation of the results gained from the models. The vertical scale bars for each of the following four graphs is kept the same for ease of comparison purposes.

The first graph shows the temperature at three meters depth for a homogeneous stratigraphic column for all five lithologies. This temperature data was compared against the temperature data for those stratigraphic columns containing a permafrost layer. This comparison was done to determine the effect a permafrost layer has on the temperature and therefore the effect on the melting of both the lithology and the permafrost layer. Clearly, epsomite is the most responsive rock type to the event.

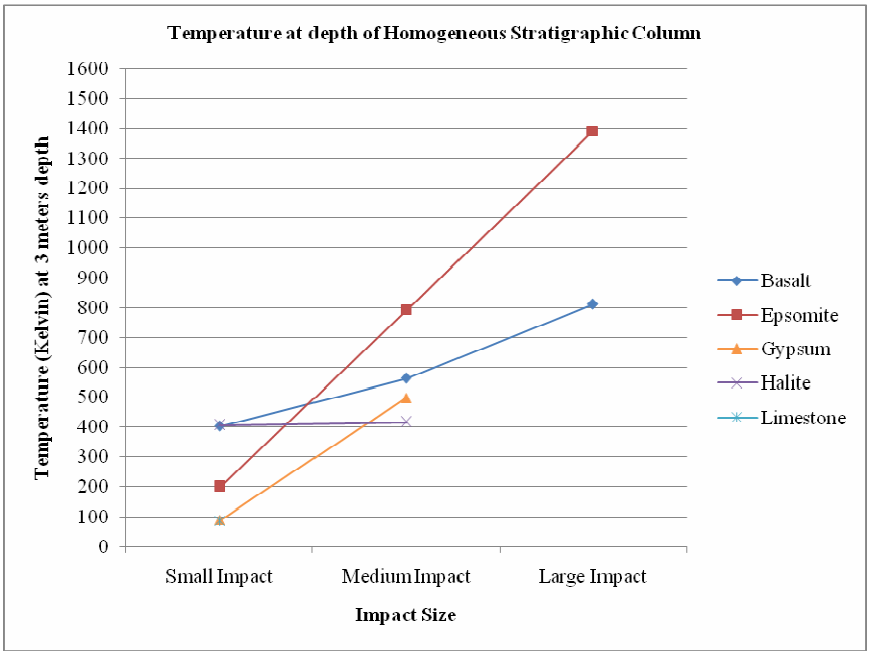

Figure 12: Graph showing temperature differences at three meters depth across lithologies and impact crater size. NOTE: The marker for limestone overlaps the lines for gypsum as the small impact location.

The following three graphs show a small, medium, and large impact size, respectively, into the four stratigraphic columns that include a permafrost layer. Notice that in the medium impact and large impact size graphs not all lithologies are represented.

This is due to the melting temperatures of the lithologies and the restrictions of the COMSOL modeling software. If the material is not in a melted state such that there is a viscosity value available to calculate the convective heat transfer coefficient the model could not be run for that lithology at that temperature, hence the absence of the lithology at that impact size.

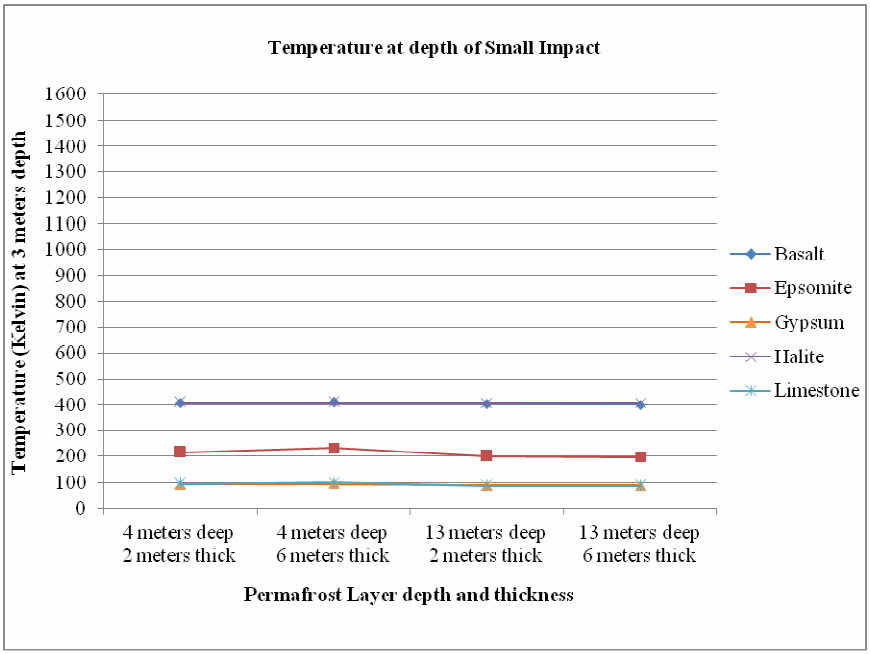

Figure 13: Graph showing temperature differences at three meters depth across various lithologies and permafrost depth and thickness for a small impact. NOTE: The basalt and halite trend lines overlap each other (top lines) as well as the gypsum and limestone trend lines (bottom lines).

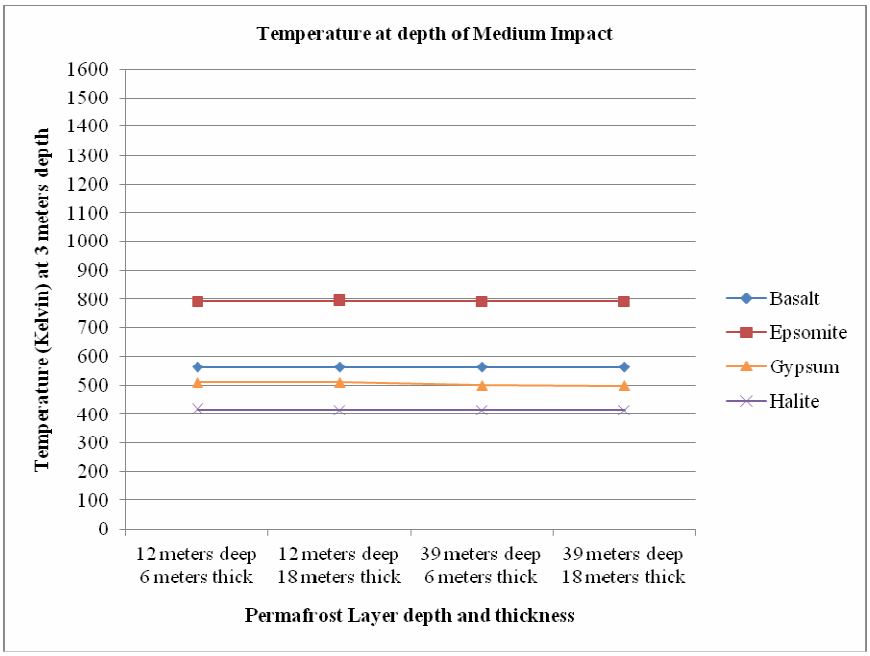

Figure 14: Graph showing temperature differences at three meters depth across various lithologies and permafrost depth and thickness for a medium impact.

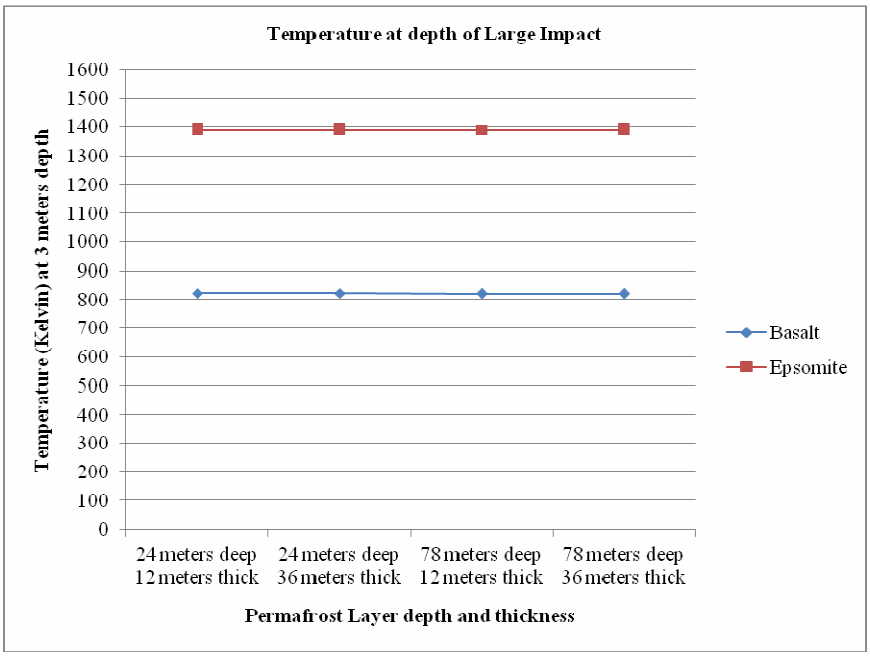

Figure 15: Graph showing temperature differences at three meters depth across various lithologies and permafrost depth and thickness for a large impact.

From these data, based on the modeling results, conclusions indicate that a permafrost layer does have an effect on the propagation of heat through the lithology. However, the near-surface permafrost layer had a much larger effect on the temperature than the deeper permafrost layer. And, the thicker permafrost layers have more influence on the lithology temperature than the thinner permafrost layers.

Lithology Melting Depth

The following four graphs show the depth at which the transition between solid material and melted material exists. These data allow for the determination of the plausibility of liquid water being released and enabling bedrock dissolution and therefore fracture enlargement. Of course, the creation of caves can proceed if dissolution and fracture enlargement exists.

The following four graphs do not include all the lithologies for all impact sizes. The absence of some lithologies occurs because the impact temperatures used in the models for those lithologies were cooler than the melting temperature for those lithologies. The cooler temperatures were used due to the lack of lithology viscosities in the literature; therefore, a value for the convective heat transfer coefficient cannot be calculated and hence no model could be constructed for those cases using this approach.

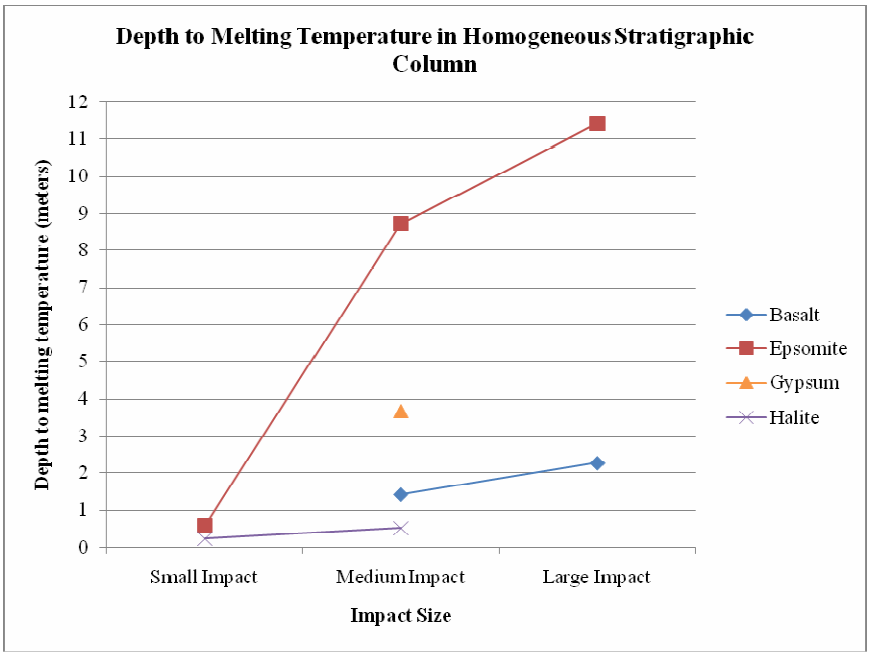

Figure 16: Depth to the melting temperature in a homogeneous stratigraphic column for the given lithologies for the four permafrost scenarios. The gypsum is only represented in the medium impact size due to the small impact size initial temperature being below the melting temperature for gypsum.

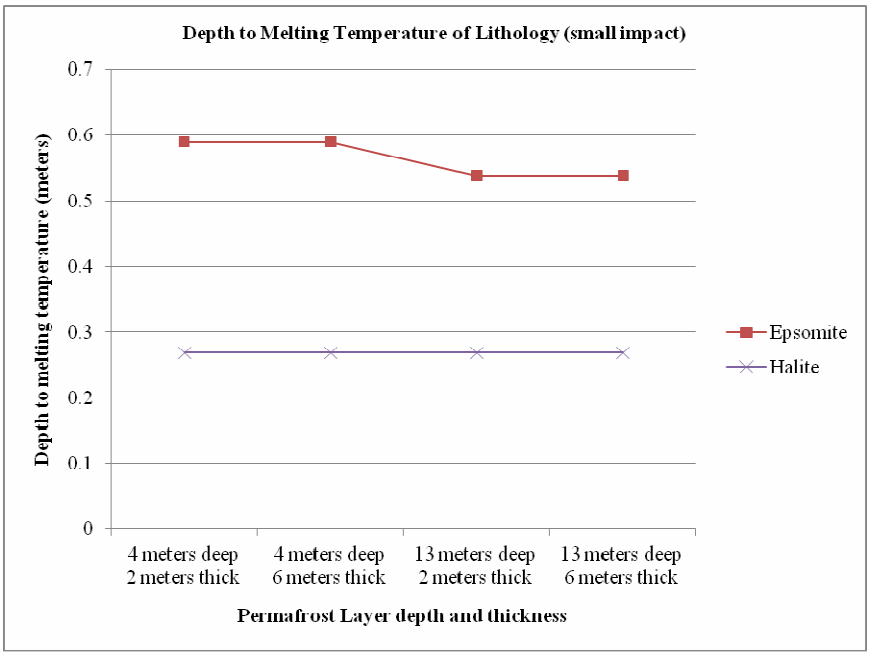

Figure 17: Depth to the melting temperature in a small sized impact for the given lithologies for the four permafrost scenarios.

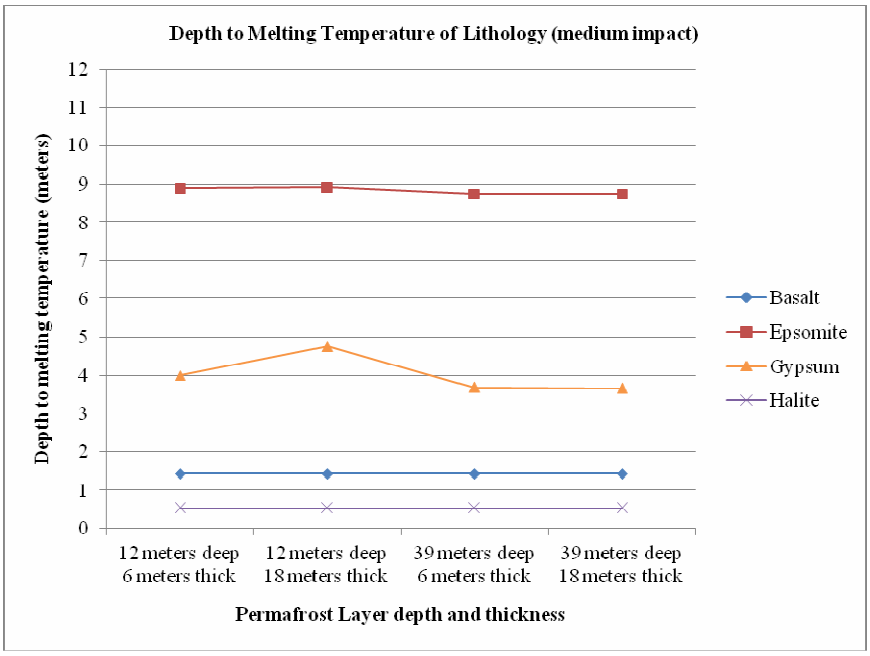

Figure 18: Depth to the melting temperature in a medium sized impact for the given lithologies for the four permafrost scenarios.

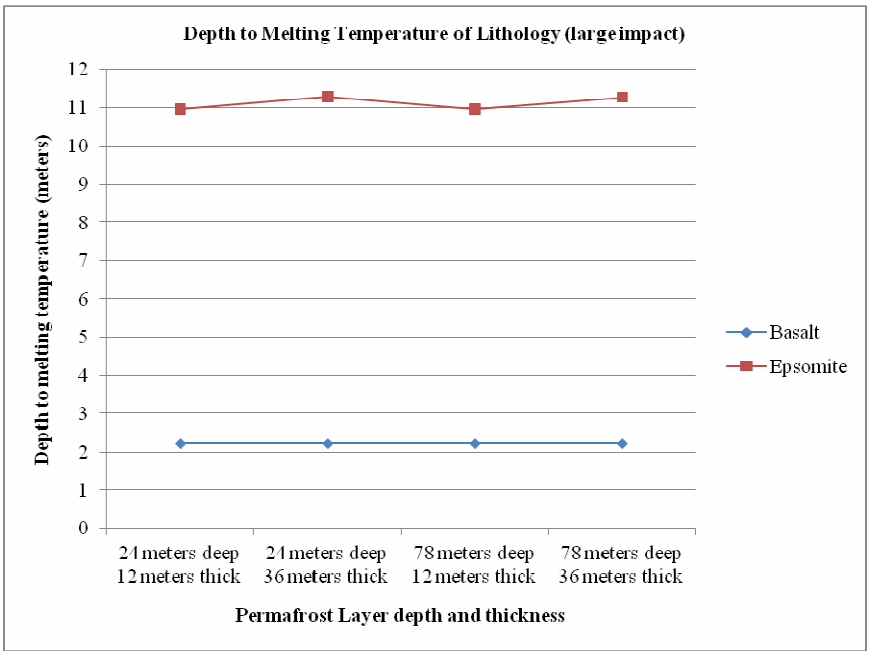

Figure 19: Depth to the melting temperature in a large sized impact for the given lithologies for the four permafrost scenarios.

Depth of Heat Penetration Comparison

Once all the models were completed for all five lithologies and all five situations a comparison was done to help interpret the different results from the models. A compilation of all the models is illustrated in Table 14 below.

To summarize the data in Table 14, the depth and thickness of a permafrost layer affects the depth to which heat will propagate within a lithologic unit. For the small impact scenario, the epsomite transmitted the impact heat the deepest; however, basalt was more effective with the transmission of heat in the medium impact scenario. The simulations with the deeper permafrost layer seemed to insulate the overlying bedrock layer; as seen in the large impact situation for epsomite. The deeper permafrost unit kept the heat from penetrating deeper than approximately 30 meters, but the shallower permafrost layer aided in the propagation of the heat allowing the heat to penetrate down to approximately 95 meters. When these depths are compared to the homogeneous baseline depth of about 90 meters, these results are significant. This same effect is seen in all the models, the shallow permafrost layer of both thicknesses aids the heat transmission. Whereas the deeper permafrost layer, again of both thicknesses, retarded the depth to which the heat penetrated.

Small Impact					
Permafrost Location	Homogeneous (no permafrost)	4 meters deep 2 meters thick	4 meters deep 6 meters thick	13 meters deep 2 meters thick	13 meters deep 6 meters thick
Basalt	~8	~10	~13	~8	~8
Epsomite	20+	20+	20+	20+	20+
Gypsum	~16	~18	20+	~18	20+
Halite	~8	~10	~14	~8	~8
Limestone	~12	~12	~16	~12	~12
Medium Impact					
Permafrost Location	Homogeneous (no permafrost)	12 meters deep 6 meters thick	12 meters deep 18 meters thick	39 meters deep 6 meters thick	39 meters deep 18 meters thick
Basalt	~30	~35	~45	~30	~30
Epsomite	~25	~25	~35	~25	~25
	Homogeneous (no permafrost)	4 meters deep 2 meters thick	4 meters deep 6 meter thick	13 meters deep 2 meter thick	13 meters deep 6 meter thick
Gypsum	~10	~12	~14	~10	~10
Halite	~8	~10	~14	~8	~8
Limestone	-	-	-	-	-
Large Impact					
Permafrost Location	Homogeneous (no permafrost)	24 meters deep 12 meters thick	24 meters deep 36 meters thick	78 meters deep 12 meters thick	78 meters deep 36 meters thick
Basalt	~30	~40	~60	~30	~30
Epsomite	~90	~95	~35	~30	~30
Gypsum	-	-	-	-	-
Halite	-	-	-	-	-
Limestone	-	-	-	-	-

Table 14: Table shows how a permafrost layer affects the depth (in meters) to which impact generated heat penetrates in the given lithologies. For the medium impact size of gypsum and halite the scale was kept the same as the small impact in order to get more accurate readings for the depth of penetration.

Discussion of Model Results

The model results here show that the temperatures associated with an impact cratering event could facilitate the melting of subsurface volatiles which in turn could increase subsurface porosity as a result, as originally hypothesized. For example, Figure 9 (a thick, near-surface permafrost layer) shows that the heat imparted during the impact event penetrated through the permafrost layer into the underlying basaltic bedrock. This depth of penetration could allow for the melting of the permafrost layer thus, enabling bedrock dissolution and fracture enlargement. However, in comparison to Figure 10 (a thick permafrost layer at depth) one can see that the same size impact event with the same amount of heat imparted potentially lacks the ability to allow for bedrock dissolution and fracture enlargement due to the lack of liquid water released from the permafrost layer. The example in Figure 9 has a greater potential for cave formation than the example in Figure 10. This conclusion is based solely on the absence of liquid water.

It is also apparent from an inspection of the results that in order for a permafrost layer to play a significant role in heat propagation, the impactor must punch nearly all the way into, if not completely through a permafrost layer. The thickness of the permafrost layer also affects the depth to which the heat penetrates. It can be seen in Figure 7 that a thin, near-surface permafrost layer allows for the propagation of the heat imparted during the impact event to a depth of approximately 10 meters. The same impact event into an area with a thick, near-surface permafrost layer allows for heat propagation to a greater depth of approximately 13 meters as seen in Figure 9. In comparison, Figure 6 shows a homogeneous basaltic stratigraphic column with heat propagation to a depth of approximately 8 meters. An overall trend seen in all models with a permafrost layer is

that a shallow permafrost layer aids in the propagation of heat to depth, in contrast to a deeper permafrost layer that retards the propagation of heat and acts as an insulator to the overlying bedrock.

The ability of the permafrost to aid or hinder the propagation of heat is probably due to the difference in material properties (Table 19 in Appendix B) between the permafrost and the other lithologies. The permafrost has a lower density and lower convective heat transfer coefficient value than the other lithologies used in this study. However, the permafrost has a higher heat capacity than the lithologies and a higher thermal conductivity than all the lithologies except epsomite. Epsomite has a higher thermal conductivity than the permafrost thus allowing the heat propagation to penetrate further into the stratigraphic column than any of the other lithologies in this study.

The heat generated due to an impact cratering event is also adequate to vaporize and/or plasticize rock material. The inspection of Figures 7, 8, and 9 shows that impact temperatures greatly exceed the melting point of both water ice and the permafrost layer represented.

The results of this study are clearly limited in terms of the suite of real possible parameters. However, they are sufficient to indicate that formation and/or increase in size of subsurface fractures and voids as a result of dissolutional processes carried out by the liquid water released from shallow permafrost layers is a plausible scenario. However, fractures in the rock material must either be present at the target site, or they must be created as a result of the impact for released water to increase the size of the fractures through dissolutional processes.

In summary, the modeling results are consistent with the notion of Martian subsurface cave formation as a result of an impact cratering event.

How models translate to actual craters

Since modeling results indicate that subsurface cave formation is a plausible result of an impact cratering event, the next step is to compare Earth and Mars crater morphologies to determine which, if any, Martian craters could potentially have impact induced cave formations. The Chicxulub Crater on the Yucatan peninsula (Figure 20) is used here as an example for comparison to Mars craters. The southern edge of the Chicxulub Crater is marked by a ring of cenotes, or fluid filled sinkholes, formed by the dissolution of the limestone bedrock (Pope, *et al.*, 1993; Connors, *et al.*, 1996; Hildebrand, *et al.,* 1991). This ring of cenotes also delineates the boundary between the unfractured limestone within the crater and the fractured limestone outside the crater (Pope, *et al.*, 1993; Connors, *et al.*, 1996; Hildebrand, *et al.,* 1991).

By taking this crater as an example of one whose creation apparently led to the formation of subsurface cavities and comparing the morphology to those crater formations on Mars, conclusions may be made about the possible formation of subsurface voids in association with impact structures on Mars. HiRISE images, taken aboard the Mars Observer Mission, were examined and one was found that showed some promise. Figure 21 shows some circular features that look very similar to sinkholes or collapse pits on Earth.

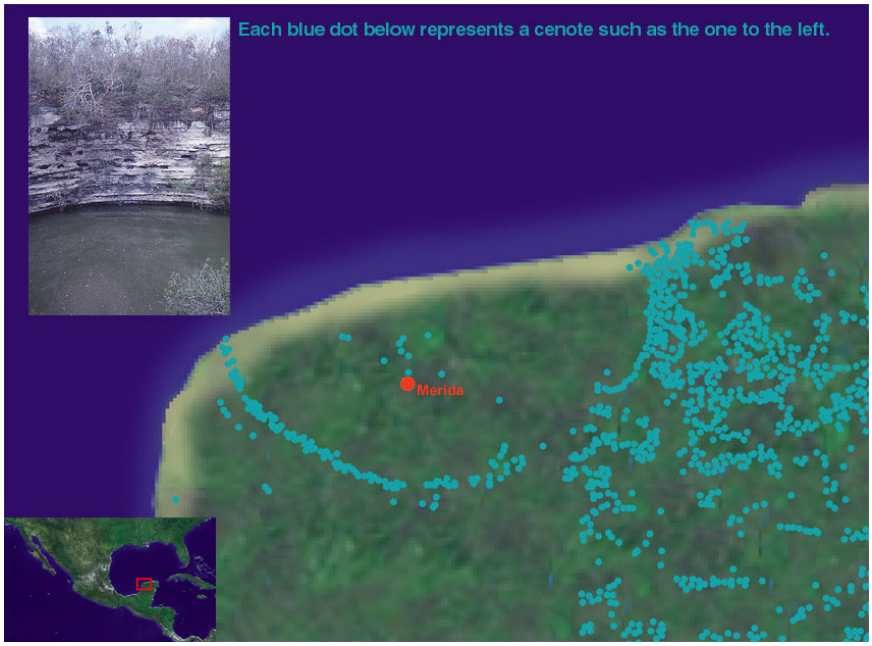

Figure 20: Image shows outline of the southern part of the Chicxulub Crater delineated by blue circles. Each blue circles also represents the location of a cenote. Image on the top left shows a close up view of one of the cenotes. Bottom left image shows location of the full image. Image credit: www.lpl.arizona.edu.

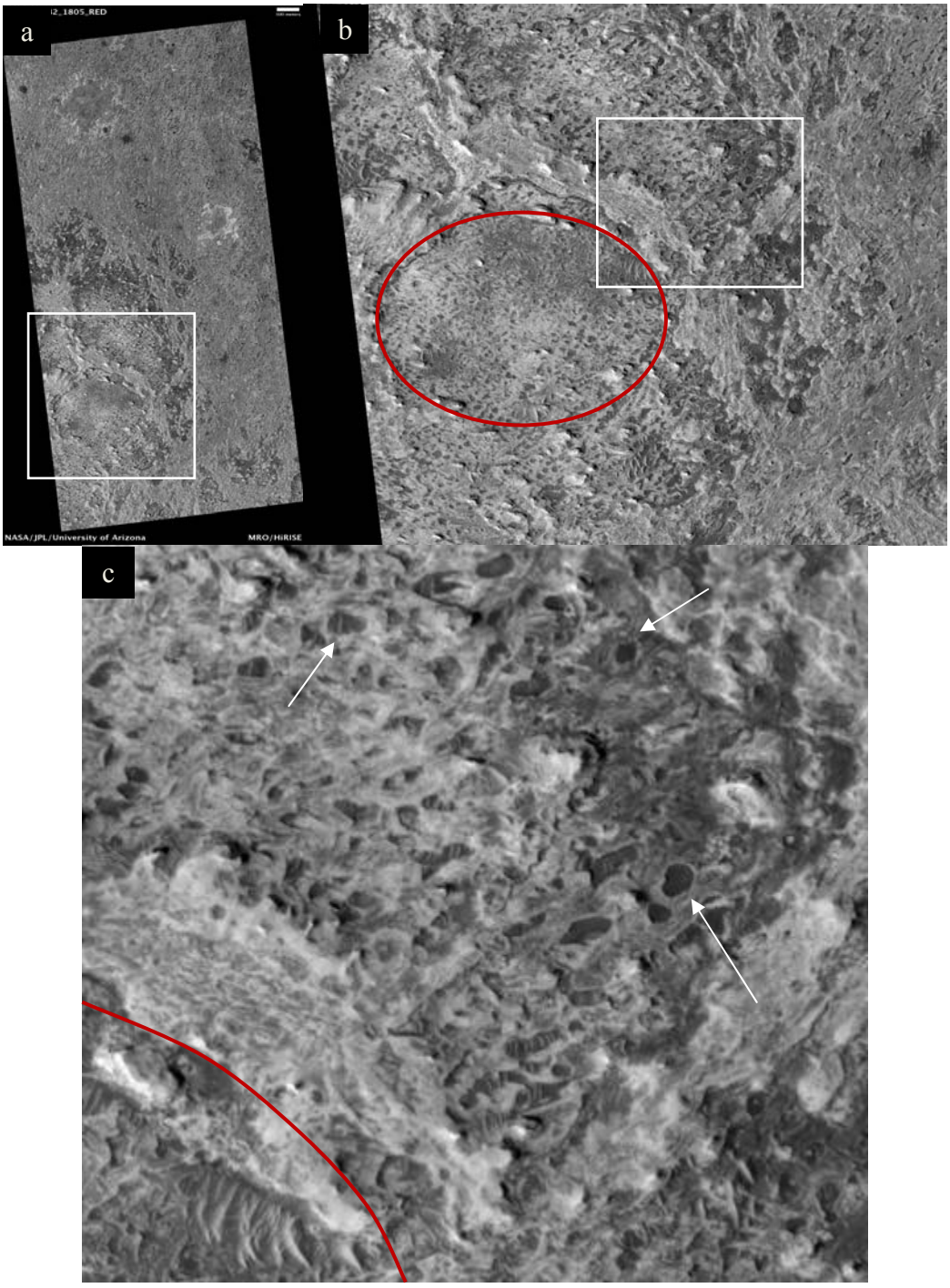

Figure 21: a) Entire image showing white box around area shown in b. b) Shows old crater outline with surrounding terrain. Red circle delineates what appears to be an old crater structure. White box indicates area shown in c. c) Shows edge of crater in lower left corner surrounded with what appears to be sinkhole type features (indicated with white arrows). These features are numerous and encircle the entire crater structure. Image Credit: NASA/JPL/University of Arizona

Figure 22: Image of some Earth cenotes (white arrows) associated with the Chicxulub Crater on the Yucatan Peninsula, Mexico. Image Credit: Google Earth.

The comparison process indicates that the round features found around a probable crater on Mars could be analogous in origin to the terrestrial cenotes. This Martian analog is only a hypothetical morphological analog due to the lack of subsurface data for Mars. Nevertheless, sites where these morphologic features exist should be further investigated as potential examples of the Martian features indicating possible subsurface voids.

Microbiological Implications & Significance

Given the possible scenarios illustrated by the results of the modeling effort, what is the potential for microbiological activity occurring in subsurface void habitats? On Earth, caves are called home by numerous microbiological species. If there is any form of microbiology present on Mars, when and for how long are the temperatures associated with an impact event in the correct temperature range to plausibly sustain such microbiological communities?

Due to extremely high temperatures and pressures associated with an impact event, any biology that is present at or immediately adjacent to the target site would likely be terminated on impact (Melosh, 1989). However, some organisms on Earth can survive transient high temperatures such as those found in association with deep sea black smokers (Wellsbury, *et al.,* 2002) and in alkaline hot springs found at Yellowstone National Park (Ward and Cohan, 2005). Hypothetically, after an impact event occurs, there are presumably no biological organisms present at the center of the impact crater, and the organisms that survive are along the outskirts of the target site. Depending on what one assumes as to the origin of such a biota, it may be in either an active or dormant state already. If the cratered material is within the desired temperature range, a dormant microbiological community may begin to become active. Microorganisms might be able to migrate in order to stay within their tolerable temperature range as the target site and

surrounding material cools over time, particularly through fluids in fractures. Once the habitat temperature drops below their possible active temperature ranges, the microorganisms could go back into a dormant state in an effort to stay alive. Even though one group of microorganisms goes into a dormant state, other groups of microorganisms whose tolerance range is cooler could be active until the temperature range drops below their temperature ranges. A hydrothermally adapted biological community, also possibly present in the warmer Martian subsurface in selected hot spots, could thrive courtesy of the hydrothermal heating of fluids in the impacted area (Cockell and Pascal, 2002; Cockell and Lim, 2005). The completion of the cooling process can be geologically short or long depending on the energy emplaced and details of the rock units into which the impactor strikes.

For each microorganism type, there are three cardinal temperatures at which growth can occur: minimum, optimum, and maximum (Madigan and Martinko, 2006). The temperature range is dependant on a combination of the intrinsic properties of the organism and its particular surroundings, thus temperature ranges can go up or down depending on nutrient availability and many other environmental stressors (*e.g.* limiting nutrients, ultraviolet light, etc.). The adaptable temperature range for many microorganisms adapted to highly variable soil environments varies between approximately a 30 to 40 degree window around its optimal growth temperature; however, growth may not occur over the entire range (Madigan and Martinko, 2006).

Microorganism Classes

Madigan and Martinko (2006) describe four classes of microorganisms based on their optimal temperature for growth: psychrophiles, mesophiles, thermophiles, and hyperthermophiles. Table 15 shows the desired temperature range for the four different groups of microorganisms. Psychrophiles are cold loving microorganisms and are typically found in unusually cold environments such as polar ice cap regions and polar or high altitude deserts. Mesophiles prefer more moderate temperatures and are typically found in temperate and tropical locations in both terrestrial and aquatic environments. Thermophiles and hyperthermophiles are heat loving microorganisms typically found in unusually warm or hot environments such as hot springs, hydrothermal vents in deep sea locations, and geysers.

Earth Analogs

The May 18th, 1980 Mount St. Helens volcanic eruption drastically changed the ecological balance of the north flank of the volcano where 500 km^2 were stripped of all visible life (Larson, 1993). After this catastrophic event, the once pristine low temperature Spirit Lake provided an opportunity for scientists to study the biological effects of such an event. Spirit Lake was originally a low-nutrient classic oligotrophic cold alpine mountain lake. Located only eight kilometers from the volcano, post-eruption it became the resting place of superheated volcanic rock, trees, burnt forest plants, vast quantities of avalanche debris, as well as large amounts of surrounding forest debris (Larson, 1993). With the introduction of superheated materials, the lake temperature rose from approximately 10 degrees Celsius to over 30 degrees Celsius within minutes of the

eruption event. Pre-eruption microbiology in Spirit Lake included an array of zooplankton and phytoplankton species (Larson, 1993). These organisms thrive in a well-oxygenated environment. Due to the drastic and rapid drop in oxygen availability, the post-eruption microbiological presence was composed primarily of bacteria and archaea which are far more resistant to chemical and thermal extremes than any eukaryotic organisms like the phytoplankton and zooplankton. Larson (1993) also states that by June 1980 the lake was anoxic and six different anaerobic microbiological groups were identified: *Karatella, Filinia, Kexarthra*, various amoeba, *Thiobacillus,* and *Enterobacter*. By April 1981 the oxygen levels in Spirit Lake were almost recovered with 6-9 milligrams per liter compared with pre-eruption levels around 9-10 milligrams per liter. This time frame for recovery is also supported by Baross, *et al.* (1982) who reports that various lakes in the blast zone of Mount St. Helens quickly became anaerobic. Microbiological populations were high within weeks of the eruption; however, not all communities were typical for the area. Baross, *et al.* (1982) attribute the increase in bacterial activity to the rising concentrations of dissolved organic carbon in the water column. Ward, *et al.* (1983) also report a drastic increase in certain algal communities as a result of eutrophication within the lakes of the Mount St. Helens blast zone.

One of the most striking features of the rapid and extreme changes in the Mt. St. Helen's lakes was the short timescales over which these changes occurred, literally within a couple of weeks. The Mt. St. Helen's example raised the question of the origin of thermophilic organisms in a setting that had previously been inhospitable to such organisms. It has been suggested that the Mt. St. Helen's case demonstrates the fact that

many different organism types can be present in populations at low levels when they are outside their optimum conditions. The combination of outside events may then enable such organisms to spring into action when catastrophic events radically alter the environment in their favor. Such a rapid response may or may not be a feature of any Martian microbiology, but it has been demonstrated in a number of instances here on Earth.

An Earth example of the formation of biological ecosystems associated with an impact crater structure is Haughton Crater in Canada. Haughton Crater is located on Devon Island within the Canadian Arctic Archipelago (Cockell and Pascal, 2002). The target lithology consists of Precambrian granites and gneisses overlain by a sequence of Paleozoic sedimentary rocks composed primarily of carbonates (Cockell and Pascal, 2002). In the past, a lake existed within this crater structure. As geologic time progressed and the crater structure was eroded, the microbiological community changed. As the crater infilled and/or the structure eroded, the lacustrine microbiological community became more indistinguishable from the surrounding environment (Cockell and Pascal, 2002). During this time the biological and geological uniqueness of the impact crater was lost. However, residual possible biosignatures of the earlier biological activity were identified by these authors.

Martian Crater Lake

On modern Mars, the likelihood of a liquid crater lake being present is probably remote (Cockell and Lim, 2005), but recent studies (Lindsay and Brasier, 2006; Cabrol and Grin, 2005) show crater lake remnants present today and suggest crater lakes may

have been present in greater abundance in the past. However, clear indication of a frozen crater lake has been seen recently on Mars (Figure 23). If crater lakes existed on Mars, this environment could have served as a potential habitat for microbiology. The heat from an impact that melts surrounding ice would allow for the creation of the lake as well as the water and heat necessary to sustain any possible biology that is present. Once the surface of the lake froze, it would provide some thermal shelter from the cold surface temperatures and retard further loss of water as well as help retain the heat necessary for the survival of organisms. The heat generated during the impact event and the geothermal gradient believed to be present on Mars would provide enough heat energy for a period of time to prevent the lake from freezing solid (Abramov and Kring, 2005). However, if some of the potential organisms present are not thermophilic (Cockell and Pascal, 2002; Cockell and Lim, 2005) in nature and do not require high temperatures to survive, but are instead cold loving organisms, an ideal environment would be within or directly under the frozen lake surface. A crater lake would be an ideal place for organisms to live given that present day Mars' surface is most likely not habitable for organisms due to cold temperatures and little or no water. Future Mars missions could investigate further these frozen crater lakes to determine if microbiological activity is present.

Figure 23: Image of frozen crater lake in the north polar region of Mars. Image was taken by ESA/DLR/FU Berlin.

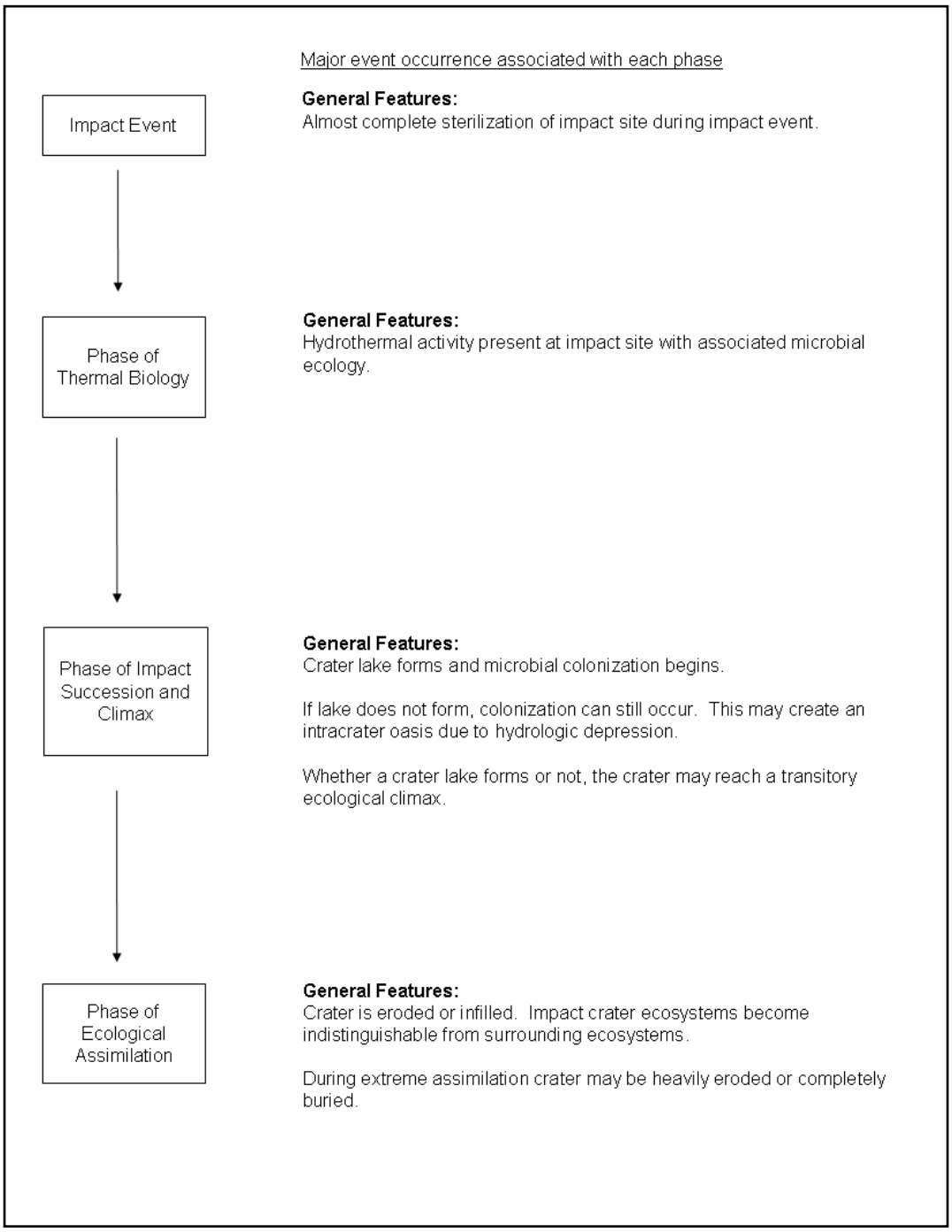

Figure 24: Progression of major phases of biological recovery during and after an impact event. After Cockell and Pascal, 2002.

In the previous example at Haughton Crater there existed a crater lake consisting of liquid water associated with extremely high temperatures and probably thermophilic microorganisms. If an impact event occurred in evaporite facies, these environmental conditions could allow for the possible formation of a crater lake and metabolism of any sulfate reducing microorganisms to feed on sulfur compounds liberated from the gypsum or an alteration product of the gypsum. With presumably no other forms of nutrients available other microorganisms may survive on the biomass created by the sulfur reducing organisms, or the microorganisms may not survive. In order to determine if microorganisms existed in the crater structure, a fossil record is necessary. Frozen crater lakes could provide the necessary means for such preservation of a fossil record. Lindsay and Brasier (2006) suggest that the global dust storms present on Mars could be a mechanism for quick burial of microorganisms and/or any evidence of microbiological activity. Since impact crater structures may be a suitable location for any possible microbiology, these structures may be an ideal location for finding a fossil record for Mars (Cockell and Lim, 2005; Hode, *et al..,* 2003; Lindsay and Brasier, 2006).

	Example Microorganism	**Minimum Temp. (K)**	**Optimal Temp. (K)**	**Maximum Temp. (K)**
Psychrophiles	Polaromonas vacuolata	273	288	293
Mesophiles	Escherichia coli	281	312	321
Thermophiles	Bacillus stearothermophilus	~314	318	~341
Hyperthermophiles	Thermococcus celer	~338	353	~386

Table 15: Microbiologically desirable temperature ranges based on Madigan and Martinko (2006).

The microorganisms living in a crater lake could be driven into the subsurface as the lake sublimates. With the increased porosity, widened fracture networks, and possible caves present in the subsurface, microorganisms could use these as a refuge from the harsh surface conditions of Mars and persist for some period of time. Since there are far more impact crater structures that do not presently have a crater lake, the best place to look for any microbiology would likely be in the subsurface.

Summary

Microbiology can be highly sensitive to rapid temperature changes, especially if the temperature rises or falls outside of tolerable adaptable ranges. With that in mind, when an impact event occurs all microbiology to some depth would be wiped out within the center of the cratered material at the very instant the event occurred due to the rapid increase in temperature and potential vaporization of some of the target material. Microorganisms present at some distance from the target site could survive and become active if the temperatures were in the tolerable range and sufficient nutrients were available. Further, organisms in a subsurface rock-fracture habitat could be released into the vicinity. However, the tolerable temperature ranges for Martian microbiology is obviously guesswork since the very existence of such microbiology is unconfirmed; these results are based on Earth analogs and Earth microbiology.

The Earth analogs described in this research provided insight into the probable recovery period necessary for microbiologic communities after a catastrophic event. The Mount St. Helen's example, although very different than the Martian environment, indicated that a period of approximately 24 days is adequate for a microbiological

community to recover from such a catastrophic event and take advantage of radically different conditions by extreme population shifts in favor of organisms adapted to the new conditions. However, this adaptation occurred amidst a fully developed global biosphere with abundant biomass on the surface. The recovery time in the volcanically affected lakes included having vast quantities of nutrients suddenly readily available, whereas, the Martian environment has a presumably smaller conceivable nutrient source unless an impact event resulted in thermal reduction of sulfates producing H_2S which could then be used as an energy source, or the release of other reduced gases (*e.g.* CH_4, COS, SO_2, or H_2). Therefore, any microbiology on Mars could take a much longer period of time to flourish to the same degree as the Mount St. Helen's example.

Conclusion

Impact cratering and ejecta blanket heat propagation was modeled using a finite element modeling software package, COMSOL. The models implemented the convection and conduction heat transfer equations in order to simulate the propagation of impact-induced heat through five different lithologies. The models assumed a steady state situation and neglected any geothermal gradient possibly present on Mars. Although the models have highly simplified geometries compared to actual Mars stratigraphy, the modeling did provide valuable insight into the possibility of a transient microbiological habitat created as a result of an impact cratering event and ejecta blanket emplacement. The modeling also provided constraints for the potential duration of significant heating as a result of an impact cratering event.

A large impact should melt the immediate material closest to the impact site; however, with the atmospheric pressures and temperatures currently present on Mars, the time period required for the cooling and solidification of the material is presumably much shorter than that on Earth. The modeling process helped to constrain the temperature effects enabling the assessment of the thermal environment microorganisms would be exposed to in these scenarios.

Impact-induced brittle fracturing and pressure changes play an important role in the modeling process. Pressure changes during an impact event are large and could have

a significant effect on the surrounding area. Fracturing that is induced as a direct result of the impact event can play a key role in the possible creation of caves; however, if small fractures are absent in the surrounding rock or are not created by the impact itself, the water released during the impact event will not be able to dissolve the rock material necessary to create caves. These subsurface fractures could ultimately allow for the transportation of fluids and thus the dissolution and eventual enlargement of fractures into actual caves. Impact-induced fracturing was looked at during preliminary modeling, however, it was determined that COMSOL is unable to solve for the random distribution and occurrence of subsurface fracture patterns based on target material properties. Because of this software limitation, the random generation of impact-induced fractures was assumed in order to facilitate the thought experiment of thinking about possible cave formation. Consultation with several investigators familiar with impact modeling revealed that the processes of fracturing are very difficult to model. This problem is at the forefront of modeling methodologies and beyond the scope of this present study.

The impact event itself would likely sterilize the immediate surroundings causing the wide extinction of any microbiology that was present due to the high temperatures associated with an impact cratering event. Any microorganisms transported to the site after the initial impact would have to adapt to the constantly changing surroundings: the high temperatures associated with the event, phase changes of the rock material, and the release of the trapped water, to name a few. The assumed geothermal gradient, coupled with the heat energy associated with the impact, would allow for a short amount of time in which any microbiology present could establish a colony.

The amount of cooling required to reach a tolerable temperature range for microbiology could take anywhere from a very short amount of time (days) to an extended amount of time (months) depending on the size of the crater formed. After a sufficient period of time to allow cooling, hyperthermophiles could begin to repopulate the area once the temperature of the surrounding rock cooled to approximately 400 Kelvin. The time necessary for the rock material to cool down enough to be tolerable for the next lower optimum temperature group of microorganisms could be anywhere from a matter of days up to possibly a week or more. For smaller impacts, over the course of approximately a month all phases of microbiological colonization and growth would be active and then be forced ultimately back into a dormant state as the temperatures slowly returned back to ambient. For larger impacts, the time constant for this sequence of processes is on the order of a few months. Because the temperature ranges are so close to the ambient temperature assumed for the rock material, it would take almost the entire cooling period for the rock material to be cool enough to sustain any kind of microbiological community. Based on these simplistic results, we could conclude that microbiological activity might not be present until just before the rock material has reached an equilibrium state with the surrounding environment.

Using results from the modeling and the microbiological considerations previously discussed, the duration of microbiologically tolerable temperature ranges was determined. These data constrain the period of time available for microbiology to become established. Here is an example using basalt with times taken from Table 6. Using a starting temperature of 1250 Kelvin, the length of time required for the basalt to cool down to 400 Kelvin would take 1.45 Earth years. This translates to a time period of

roughly 24 days during which the temperatures would be within a single group of microorganism's tolerable temperature range. The question arises, is 24 days enough time for a microorganism to take hold and survive long enough to leave behind a biosignature that can be detected with instrumentation? Based on the lithological cooling rates, a large impact would be necessary in order for the cooling rates to be long enough for the establishment of a microbiological community.

Our conclusions indicate that an environment suitable for the existence of microbiology on Mars is plausible. This information could help determine which sites on Mars would be the best place to search for microbiology. During future missions, landers could carry appropriate instrumentation in order to detect the presence of any of a suite of potential biosignatures at a pre-determined crater site based on analysis of its history as a potential ancient pool . If the environmental conditions suitable for microbiology include the possibility of large subsurface voids, the landers could also investigate the existence and extent of such voids with the possible implementation of ground penetrating radar. If the voids exist and are large enough for humans, future human missions to Mars could potentially inhabit them and use them as a form of shelter from the harshness of the Martian surface.

Future Work

To our knowledge, this is the first attempt to determine the plausibility of a transient microbiological habitat as a result of either an impact cratering event or the emplacement of an impact crater ejecta blanket. While carrying out this research it became evident that additional work must be done in order to fully understand the

subsurface effects of an impact cratering event. One such area that requires additional work is the determination of the physical size of the crater as well as the energy size dealt with here, and therefore the size of the impactor, necessary to allow for all the pieces of the puzzle to be present for subsurface cave formation to occur. The second area requiring more attention is the issue of impact cratering effects on any pre-existing cave systems and microbiology in the subsurface. This could be carried out for both Earth and Mars possibly through laboratory experiments and further modeling.

Appendix A

COMSOL Modeling

COMSOL Computer Software

The governing equation used for modeling purposes was the convection and conduction steady state heat balance equation, which is expressed as:

$$\nabla\cdot(-k\nabla T + \rho C_p T u) = 0, \qquad \text{Equation 4}$$

where k is the thermal conductivity; T is the temperature; ρ is the density; C_p is the specific heat capacity (COMSOL, 2005a); and u is the velocity field. The subdomain used the heat transfer equation:

$$-\nabla(k\nabla T) = Q + h_{trans}(T_{ext} - T) + C_{trans}\,(T_{ambtrans}{}^4 - T^4), \qquad \text{Equation 5}$$

where Q is the heat source and h is the heat transfer coefficient.

The following series of equations was used based on boundary designations of the model. Each boundary is identified in Figure 25 and Figure 26 with the spatial relationships to which each equation was applied. The heat flux equation is:

$$\mathrm{n}\cdot(k\nabla T) = q_0 + h(T_\infty - T) + (T_{amb}{}^4 - T^4), \qquad \text{Equation 6}$$

where T_∞ is the surrounding air temperature and T_{amb} is the ambient temperature. The continuity equation was used for geometric boundaries that have no effect on the resulting outcome. The continuity equation is expressed as:

$$\mathrm{n}\cdot(k_1\nabla T_1 - k_2\nabla T_2) = 0. \qquad \text{Equation 7}$$

The temperature equation is expressed as:

$$T = T_{0,} \qquad \text{Equation 8}$$

where T_0 is the initial temperature. This equation allowed for different impact sizes and different temperatures. Figure 25 illustrates the single layer models and Figure 26 illustrates the triple layer models. Both figures show all boundaries labeled with their respective designation. The single layer consists of a homogeneous lithology to depth, whereas, the triple layer employs two different lithologies for each model simulation with a permafrost layer varying in depth and thickness between two layers of the same rock type (*e.g.* basalt, permafrost, basalt). The initial values for all these boundaries are dependant on the material and impact temperature being modeled. These values along with the permafrost values are given in Table 19 located at the end of Appendix B.

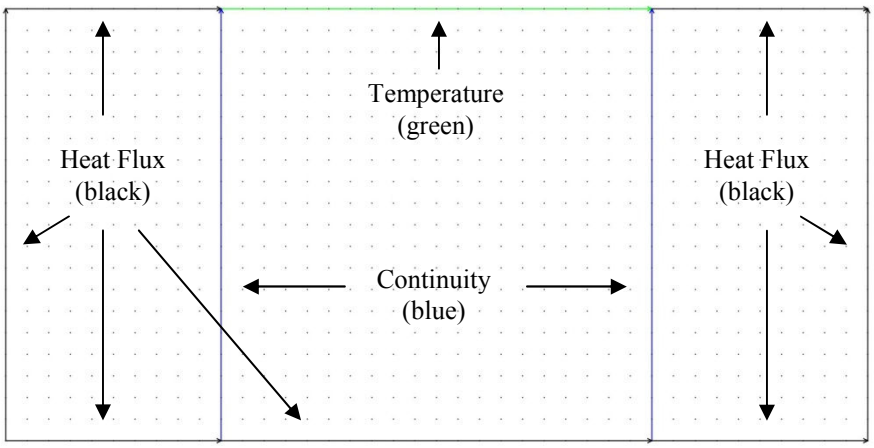

Figure 25: Single layer stratigraphic column with boundary designations labeled.

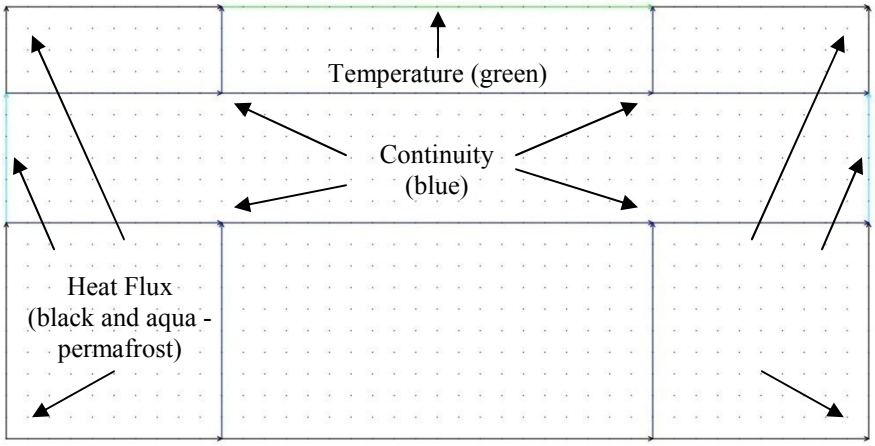

Figure 26: Triple layer stratigraphic column with boundary designations labeled.

In order to determine the amount of heat transferred to the surrounding area, estimation of the energy associated with an impact event was determined by COMSOL and was illustrated as an increase in temperature to the surrounding area.

COMSOL Solvers

In COMSOL the *heat transfer by conduction* module was used in a two-dimensional fashion. All models have a stationary analysis type and the lagrangian-quadratic element type. The geometries for the homogeneous lithology consisted of separate rectangles placed appropriately to create one large rectangle. This was done to facilitate the establishment of boundary conditions as well as the impact temperature location. The rectangles are considered the subdomain and are given the respective values for the particular lithology being modeled. The line boundaries of the rectangles are assigned values appropriate for the specific function that the boundary performs, whether the function is temperature, heat flux, or an internal boundary considered to be continuous. The mesh was refined to accurately display the associated heat propagation

through the subdomain geometry. Once this information was entered as model parameters and the mesh was acceptable, the model was solved using the *Direct UMFPACK*, a built-in linear system solver.

During the post-processing stage, the surface temperature was modeled. This characteristic was chosen in order to determine how deep into the target lithology the heat from an impact cratering event would propagate. The temperature also illustrated the effect that permafrost layers could have on the overall heat propagation in the different lithologies.

Modeling Assumptions

Some unsubstantiated assumptions were made due to sparse information for the Martian surface and subsurface as well as the limitations of the software. All the material properties are based on terrestrial measurements and environmental conditions rather than under Martian conditions. The difference in gravitational force was not accounted for in COMSOL; however, it was accounted for in the calculations of the material properties. In addition, the Martian geothermal gradient was also not considered in the modeling process due to input parameter limitations. Models could only be evaluated for materials that had a viscosity value in order to determine the convective heat transfer coefficient, so all lithologies could not be used for every temperature. The lithologies were included in the model temperature range if the material was in a melted state. The melting and boiling temperatures are listed in Table 16 for the five materials considered in this project.

Lithology	Melting Temperature [Kelvin]	Boiling Temperature [Kelvin]
Basalt	1351	1482
Epsomite	423	-
Gypsum	436	1723
Halite	1073	1738
Limestone	825	1743

Table 16: Property temperatures used for the modeling process. (Perry and Phillips, 1995; Lide, 2004)

Sensitivity Test

A sensitivity test was done on the mesh resolution within COMSOL in order to acquire the best degree of resolution suitable to the scientific questions in this study. The model that was chosen for the sensitivity test was the small impact into a homogeneous basalt stratigraphic section. The mesh resolution was initiated at the coarsest setting and was refined one step at a time until a statistically identical temperature resulted at the same location for two consecutive mesh resolutions. The location used to acquire the temperature reading was at approximately the center of the model, zero meters from the impact site, and approximately three meters deep. The data for the sensitivity test is illustrated in Table 17. As evident by the data the third and fourth refinement of the mesh resulted in the same temperature at the same location, for that reason the third mesh resolution was deemed adequate for the purposes of the models discussed here.

Mesh Statistics	Initial	Refine 1	Refine 2	Refine 3	Refine 4
Degrees of freedom	1017	3969	15681	62337	248577
Number of mesh points	267	1017	3969	15681	62337
Number of elements	484	1936	7744	30976	123904
Minimum element quality	0.7707	0.7707	0.7707	0.7707	0.7707
Element area ratio	0.1890	0.1890	0.1890	0.1890	0.1890
Temperature	405.27	403.56	403.67	403.69	403.69

Table 17: Mesh statistics with corresponding temperature (Kelvin) readings. Temperatures were evaluated at the center of the impact crater site and approximately 3 meters deep.

The purpose of conducting this sensitivity test is to determine how fine the mesh resolution needs to be in order to get the most accurate results. Since the results of the modeling process are going to be used to determine the plausibility of the existence of microbiological communities on Mars, these results need to be fairly accurate.

Appendix B

Material Properties

Known Martian lithologies were considered in order to determine appropriate material properties for use in the computer modeling. Selections of highly idealized situations were made and comprise the known lithology types on Mars. Properties of these lithologies will include, but are not limited to: thermal conductivity, density, and specific heat. The material properties are used in the model to help create a planet wide set of results.

Carbonatite lavas were used to determine the viscosity of epsomite, gypsum, limestone, and halite. Using carbonatite lava properties for the viscosities of the four other lithologies was based on the similarities of all five materials in specific gravity and hardness. The hardness and specific gravity of the other four lithologies were similar to the limestone yet different enough that the same viscosity value could be used to calculate the convective heat transfer coefficient and still get accurate results in the modeling software. This is because the calculation of the heat transfer coefficient considers the values listed here as well as others (see Equation 13). The viscosity value of limestone was based on Treiman and Schedl's (1983) limestone carbonatite lava viscosity listed as $5x10^{-2}$ Pa·s. The material properties listed in Table 18 are very similar, therefore the same viscosity value was assumed for the other four lithologies.

Rock Material	Hardness	Specific Gravity
Gypsum	2	1.52
Epsomite	2-2.5	1.46
Halite	2.5	1.54
Limestone	2.5-3	1.66

Table 18: Comparison of hardness and specific gravity for gypsum, epsomite, halite, and limestone. (values from Klein, 2002)

The convective heat transfer coefficient values for all lithologies were calculated using the viscosity values and a series of equations. These equations include the Grashof Number (Gr), Prandtl Number (Pr), Rayleigh Number (Ra), and Nusselt Number (Nu) (Incropera, *et al.*, 2007):

$$Gr_L = \frac{g\beta(T_s - T_\infty)L^3}{v^2}, \quad \text{Equation 9}$$

$$Pr = \frac{v}{\alpha}, \quad \text{Equation 10}$$

$$Ra = Gr \cdot Pr = \frac{g\beta(T_s - T_\infty)L^3}{v\alpha}, \quad \text{Equation 11}$$

$$Nu = \frac{hL}{k} = CRa^n, \quad \text{Equation 12}$$

where g is the gravitational acceleration for Mars; β is the volumetric volume expansion; T_s is the temperature of the rock surface; T_∞ is the temperature of the surrounding air; L is the characteristic length; v is the kinematic viscosity; α is the thermal diffusivity; and assuming turbulent flow, C = 0.1 and n=1/3. The convective heat transfer coefficient was determined using the following equation:

$$h = \frac{C_g\beta(T_s - T_\infty)L^2 k}{v^2 \alpha}, \quad \text{Equation 13}$$

where C is the heat capacity rate. A complete list of material properties used as input parameters can be found in Table 6. After the values were determined for all materials,

the values were then put into COMSOL and each scenario was solved using the built-in solvers.

	k [W $m^{-1}K^{-1}$]	**ρ** [kg m^{-3}]	$\mathbf{C_p}$ [J $kg^{-1}K^{-1}$]	**h** [W $m^{-3}K^{-1}$]
For all Temperatures				
Permafrost	2.24	920	2120	0.030
Basalt	1.15	1950	1090	0.865
Epsomite	2.43	1755	1510	0.217
Gypsum	1.30	1954	1088	0.145
Halite	0.60	1914	1150	0.434
Limestone	1.60	1914	1050	0.519

Table 19: Table gives all material property values used in COMSOL modeling for all temperatures discussed here. Permafrost properties were kept the same throughout all models. Epsomite, Gypsum, and Halite viscosities are based on Limestone viscosities due to the similarities of the rock properties. (All values compiled from the following: Perry and Phillips, 1995; Incropera, et al., 2006 used to calculate convective heat transfer coefficient; Palliser and McKibbin, 1998; Thompsom and Gavelis, 1956; Touloukian, Judd, and Roy, 1989; Klein, 2002; Murase and McBirney, 1970; Noritomi, 1956; Sass and Muntoe, 1974; Lindroth and Krawza, 1971; Dmitriev, Derbenev, and Goncharov, 1969; Somerton and Boozer, 1960; Birch and Clark, 1940; Rossini, *et al.*, 1956; Yang, 1979; Kieffer, 1971; Sinke, 1959; Treiman and Schedl, 1983; Bartlett, 1969; Huppert and Sparks, 1980; Dunn, 1986; Scarfe22, 1986)

Appendix C

COMSOL Modeling Figures

Impact Crater Modeling Results

The impact crater modeling results are shown here to illustrate the interaction of various situations involving a permafrost layer. All models illustrate similar stratigraphic locations for the permafrost layer. Each figure shows heat propagation through the material with contour lines indicating different temperatures in the material. The contour intervals are the same for each figure for ease of comparison. Figure captions provide further explanations for each individual case.

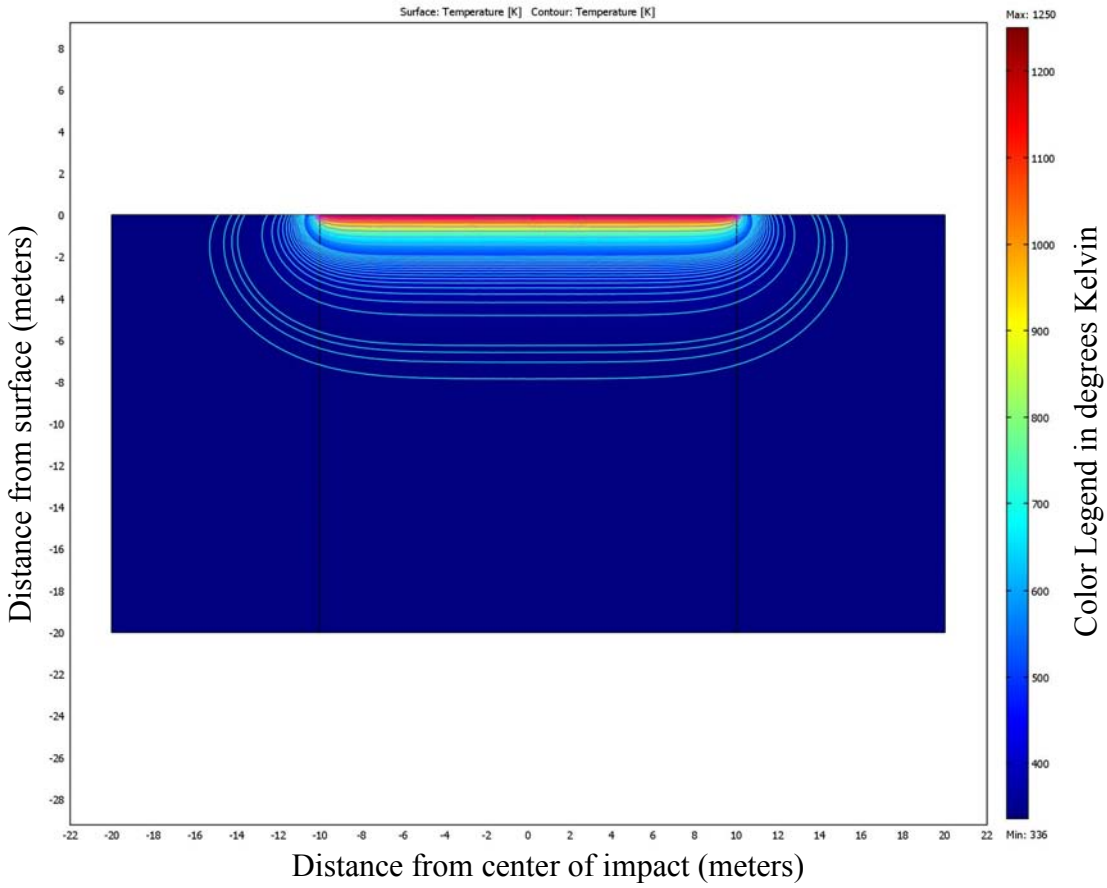

Figure 27: COMSOL generated image of a homogeneous basalt stratigraphic column. The basalt layer is 20 meters thick. The vertical black lines can be ignored and in no way effect the resulting model.

Contour Intervals: 1200, 1100, 1000, 900, 800, 700, 600, 500, 490, 480, 470, 460, 450, 440, 430, 420, 410, 400, 390, 380, 370, 360, 350, 340, 339, 338, 337, 336

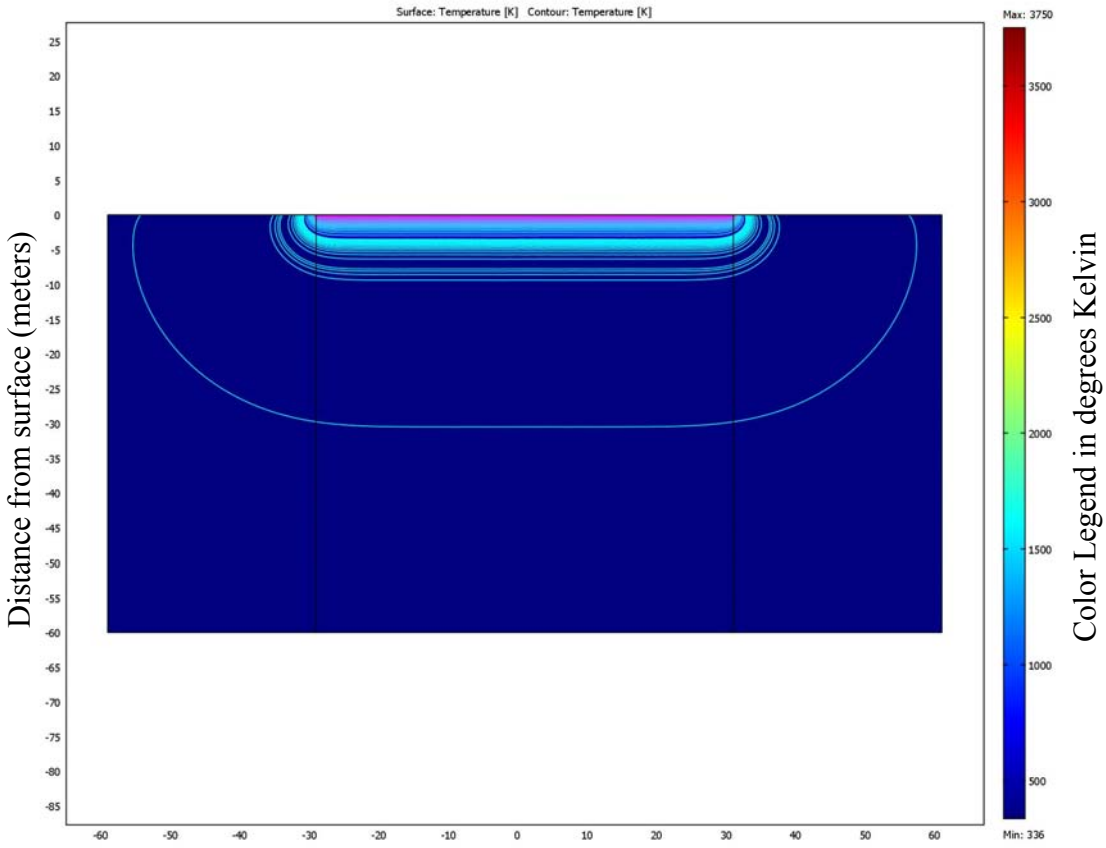

Figure 28: COMSOL generated image of a homogeneous basalt stratigraphic column. The basalt layer is 60 meters thick. This model is 3 times that of Figure 27. The vertical black lines can be ignored and in no way effect the resulting model.

Contour Intervals: 3700, 3600, 3500, 3400, 3300, 3200, 3100, 3000, 2900, 2800, 2700, 2600, 2500, 2400, 2300, 2200, 2100, 2000, 1900, 1800, 1700, 1600, 1500, 1400, 1300, 1200, 1100, 1000, 900, 800, 700, 600, 500, 490, 480, 470, 460, 450, 440, 430, 420, 410, 400, 390, 380, 370, 360, 350, 340, 339, 338, 337, 336

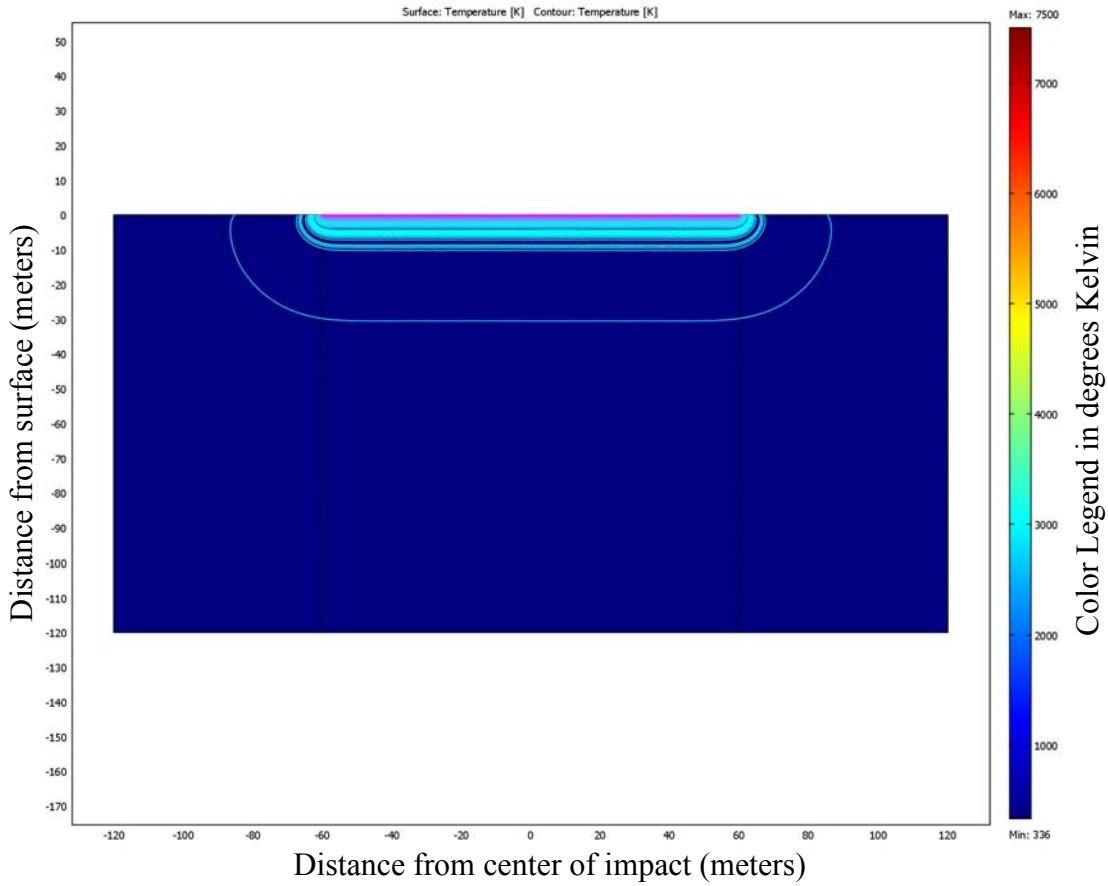

Figure 29: COMSOL generated image of a homogeneous basalt stratigraphic column. The basalt layer is 120 meters thick. This model is 6 times that of Figure 27. The vertical black lines can be ignored and in no way effect the resulting model.

Contour Intervals: 7500, 7400, 7300, 7200, 7100, 7000, 6900, 6800, 6700, 6600, 6500, 6400, 6300, 6200, 6100, 6000, 5900, 5800, 5700, 5600, 5500, 5400, 5300, 5200, 5100, 5000, 4900, 4800, 4700, 4600, 4500, 4400, 4300, 4200, 4100, 4000, 3900, 3800, 3700, 3600, 3500, 3400, 3300, 3200, 3100, 3000, 2900, 2800, 2700, 2600, 2500, 2400, 2300, 2200, 2100, 2000, 1900, 1800, 1700, 1600, 1500, 1400, 1300, 1200, 1100, 1000, 900, 800, 700, 600, 500, 490, 480, 470, 460, 450, 440, 430, 420, 410, 400, 390, 380, 370, 360, 350, 340, 339, 338, 337, 336

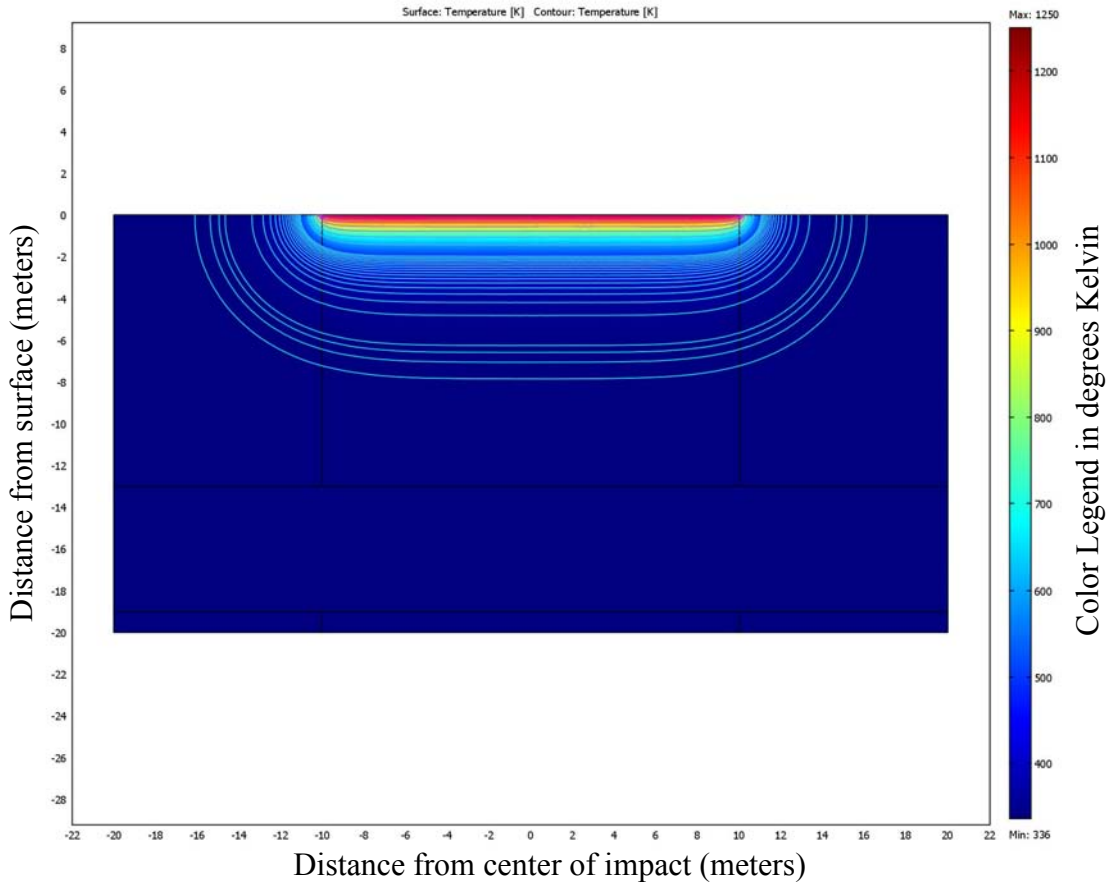

Figure 30: COMSOL generated image of a basalt, permafrost, basalt stratigraphic column. The permafrost layer is 6 meters thick at a depth of 13 meters. The vertical black lines can be ignored and in no way effect the resulting model. The horizontal black lines indicate the contact boundary between the basalt and permafrost layers.

Contour Intervals: 1200, 1100, 1000, 900, 800, 700, 600, 500, 490, 480, 470, 460, 450, 440, 430, 420, 410, 400, 390, 380, 370, 360, 350, 340, 339, 338, 337, 336

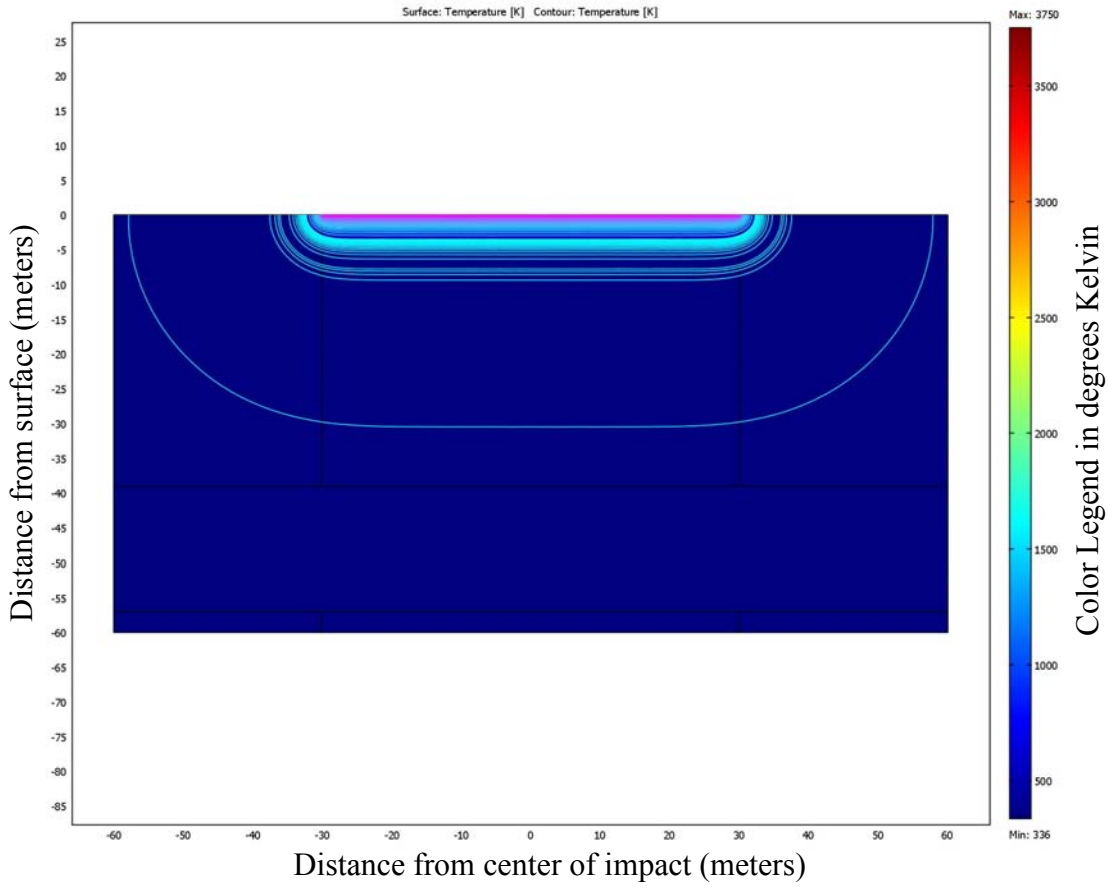

Figure 31: COMSOL generated image of a basalt, permafrost, basalt stratigraphic column. The permafrost layer is 18 meters thick at a depth of 39 meters. This model is 3 times that of Figure 30. The vertical black lines can be ignored and in no way effect the resulting model. The horizontal black lines indicate the contact boundary between the basalt and permafrost layers.

Contour Intervals: 3700, 3600, 3500, 3400, 3300, 3200, 3100, 3000, 2900, 2800, 2700, 2600, 2500, 2400, 2300, 2200, 2100, 2000, 1900, 1800, 1700, 1600, 1500, 1400, 1300, 1200, 1100, 1000, 900, 800, 700, 600, 500, 490, 480, 470, 460, 450, 440, 430, 420, 410, 400, 390, 380, 370, 360, 350, 340, 339, 338, 337, 336

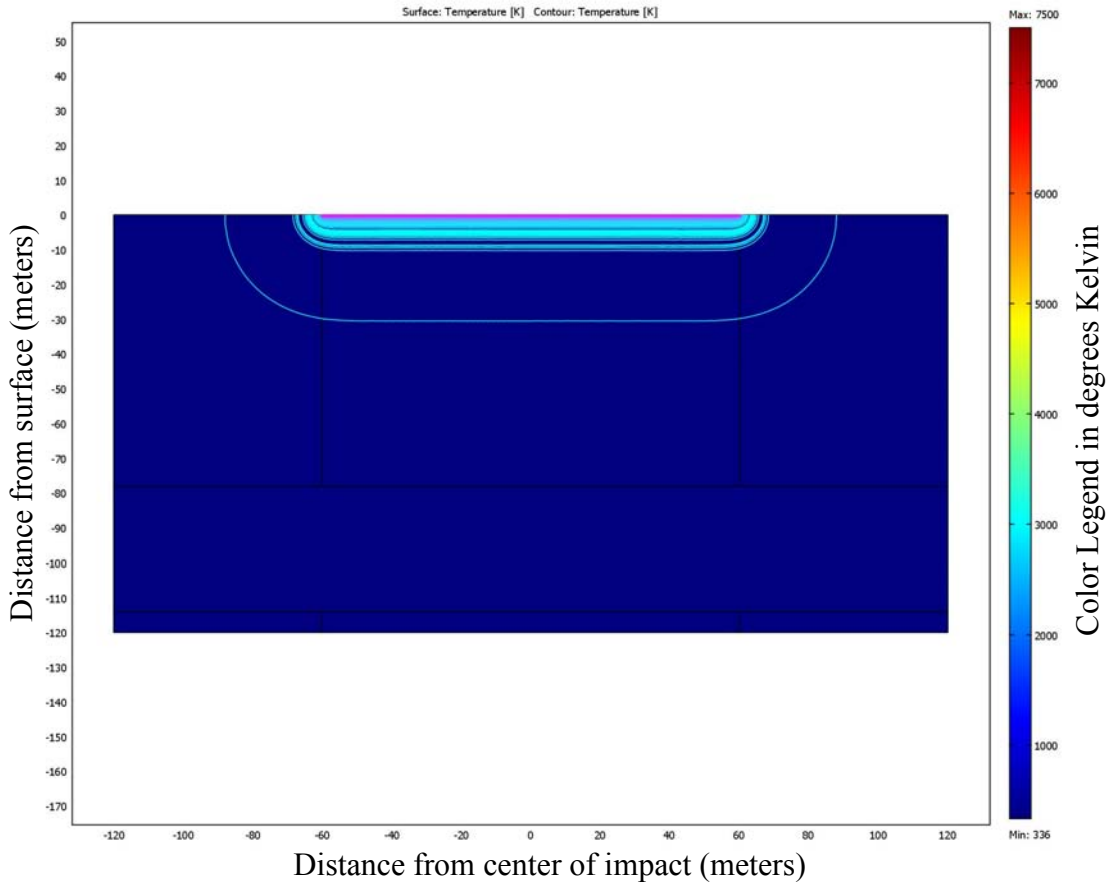

Figure 32: COMSOL generated image of a basalt, permafrost, basalt stratigraphic column. The permafrost layer is 36 meters thick at a depth of 78 meters. This model is 6 times that of Figure 30. The vertical black lines can be ignored and in no way effect the resulting model. The horizontal black lines indicate the contact boundary between the basalt and permafrost layers.

Contour Intervals: 7500, 7400, 7300, 7200, 7100, 7000, 6900, 6800, 6700, 6600, 6500, 6400, 6300, 6200, 6100, 6000, 5900, 5800, 5700, 5600, 5500, 5400, 5300, 5200, 5100, 5000, 4900, 4800, 4700, 4600, 4500, 4400, 4300, 4200, 4100, 4000, 3900, 3800, 3700, 3600, 3500, 3400, 3300, 3200, 3100, 3000, 2900, 2800, 2700, 2600, 2500, 2400, 2300, 2200, 2100, 2000, 1900, 1800, 1700, 1600, 1500, 1400, 1300, 1200, 1100, 1000, 900, 800, 700, 600, 500, 490, 480, 470, 460, 450, 440, 430, 420, 410, 400, 390, 380, 370, 360, 350, 340, 339, 338, 337, 336

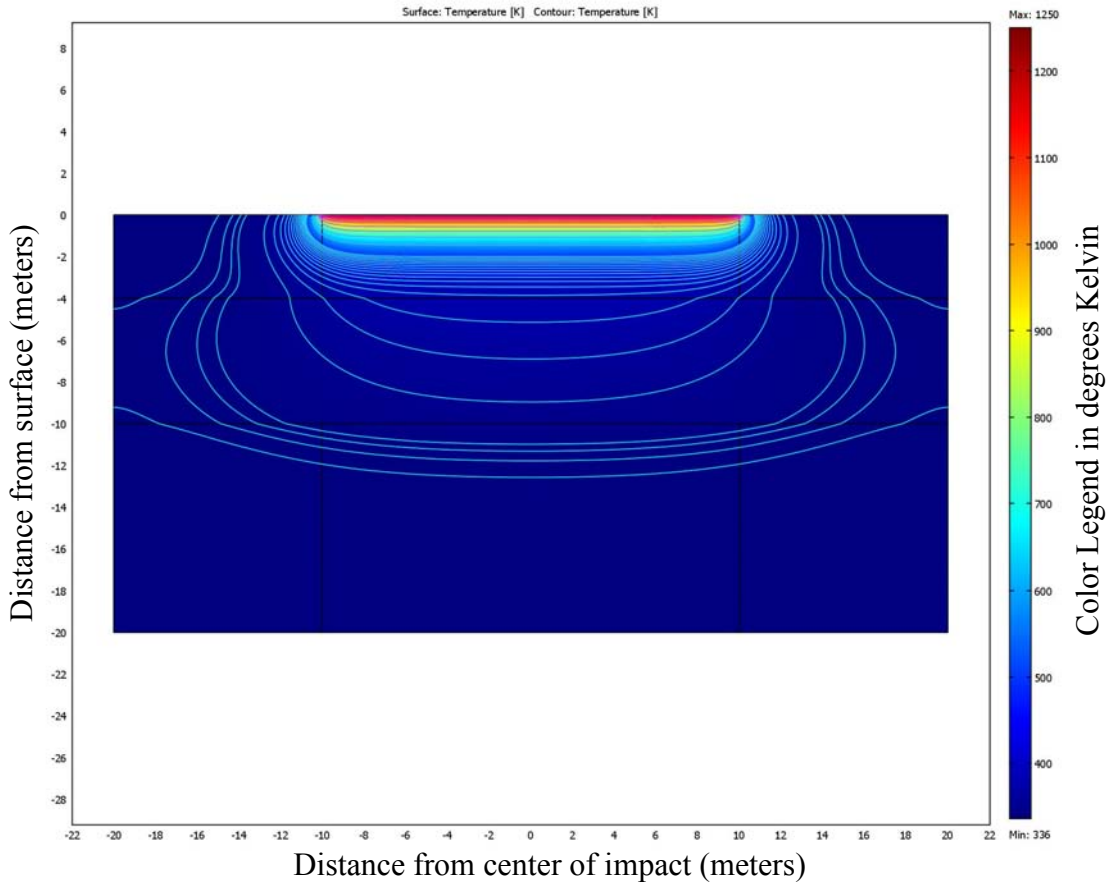

Figure 33: COMSOL generated image of a basalt, permafrost, basalt stratigraphic column. The permafrost layer is 6 meters thick at a depth of 4 meters. The vertical black lines can be ignored and in no way effect the resulting model. The horizontal black lines indicate the contact boundary between the basalt and permafrost layers.

Contour Intervals: 1200, 1100, 1000, 900, 800, 700, 600, 500, 490, 480, 470, 460, 450, 440, 430, 420, 410, 400, 390, 380, 370, 360, 350, 340, 339, 338, 337, 336

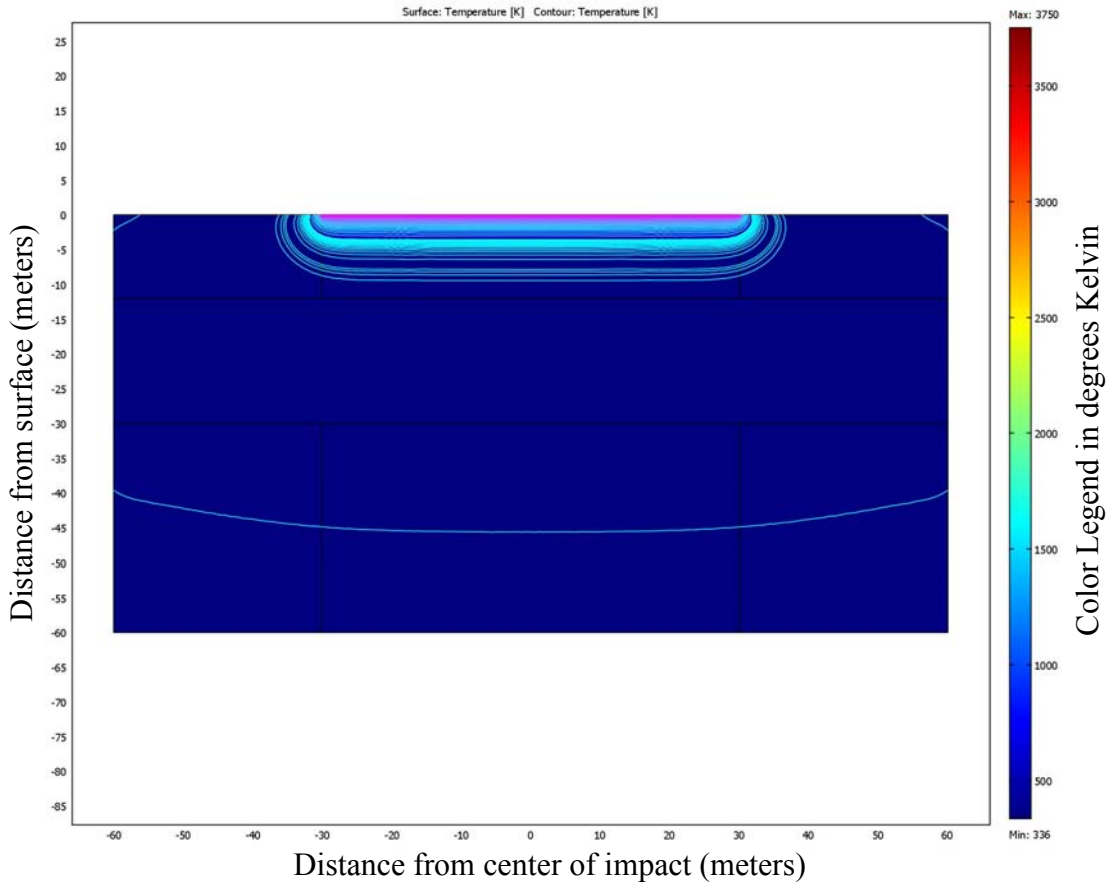

Figure 34: COMSOL generated image of a basalt, permafrost, basalt stratigraphic column. The permafrost layer is 18 meters thick at a depth of 12 meters. This model is 3 times that of Figure 33. The vertical black lines can be ignored and in no way effect the resulting model. The horizontal black lines indicate the contact boundary between the basalt and permafrost layers.

Contour Intervals: 3700, 3600, 3500, 3400, 3300, 3200, 3100, 3000, 2900, 2800, 2700, 2600, 2500, 2400, 2300, 2200, 2100, 2000, 1900, 1800, 1700, 1600, 1500, 1400, 1300, 1200, 1100, 1000, 900, 800, 700, 600, 500, 490, 480, 470, 460, 450, 440, 430, 420, 410, 400, 390, 380, 370, 360, 350, 340, 339, 338, 337, 336

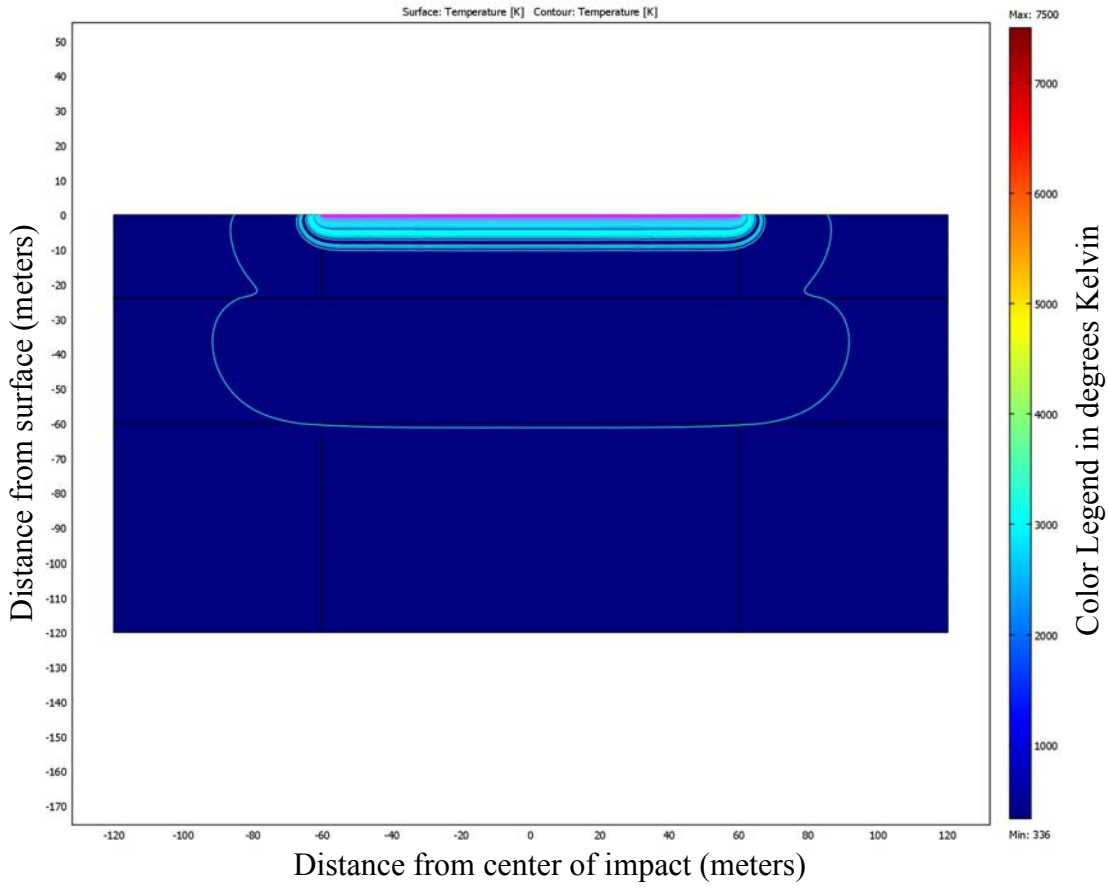

Figure 35: COMSOL generated image of a basalt, permafrost, basalt stratigraphic column. The permafrost layer is 36 meters thick at a depth of 24 meters. This model is 6 times that of Figure 33. The vertical black lines can be ignored and in no way effect the resulting model. The horizontal black lines indicate the contact boundary between the basalt and permafrost layers.

Contour Intervals: 7500, 7400, 7300, 7200, 7100, 7000, 6900, 6800, 6700, 6600, 6500, 6400, 6300, 6200, 6100, 6000, 5900, 5800, 5700, 5600, 5500, 5400, 5300, 5200, 5100, 5000, 4900, 4800, 4700, 4600, 4500, 4400, 4300, 4200, 4100, 4000, 3900, 3800, 3700, 3600, 3500, 3400, 3300, 3200, 3100, 3000, 2900, 2800, 2700, 2600, 2500, 2400, 2300, 2200, 2100, 2000, 1900, 1800, 1700, 1600, 1500, 1400, 1300, 1200, 1100, 1000, 900, 800, 700, 600, 500, 490, 480, 470, 460, 450, 440, 430, 420, 410, 400, 390, 380, 370, 360, 350, 340, 339, 338, 337, 336

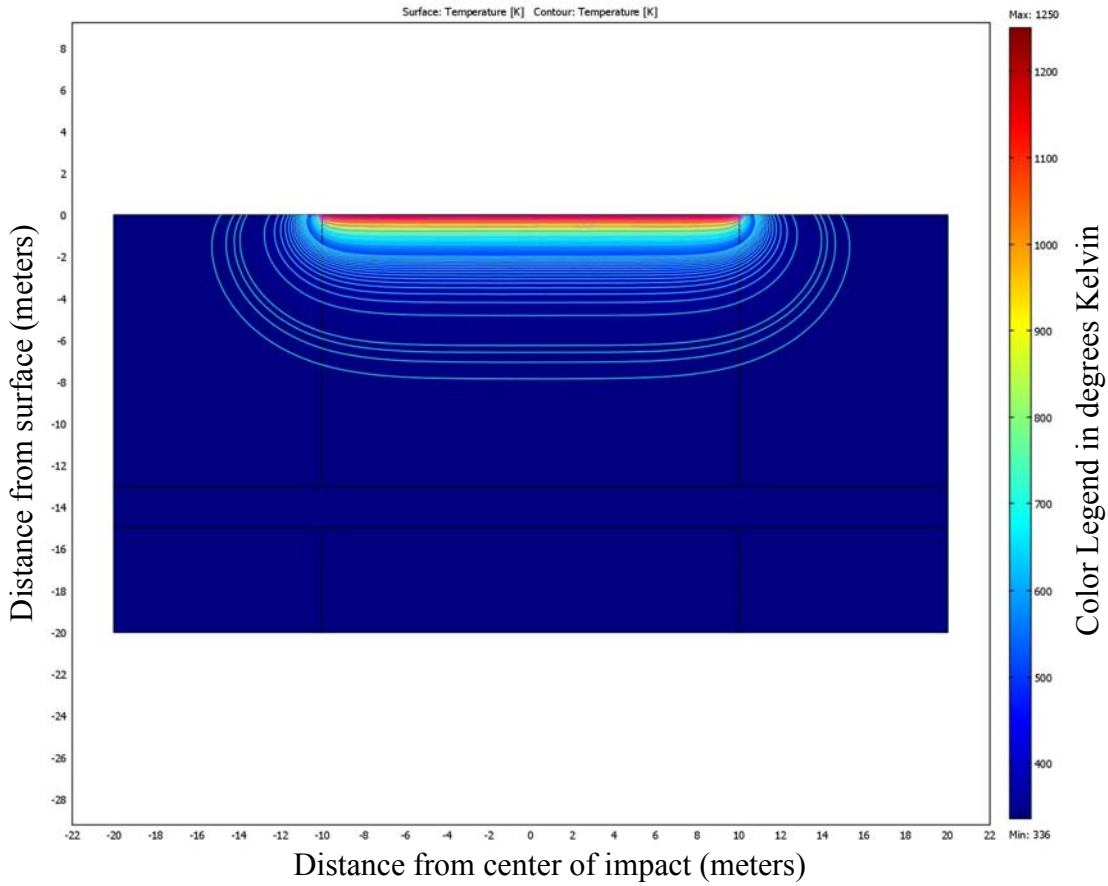

Figure 36: COMSOL generated image of a basalt, permafrost, basalt stratigraphic column. The permafrost layer is 2 meters thick at a depth of 13 meters. The vertical black lines can be ignored and in no way effect the resulting model. The horizontal black lines indicate the contact boundary between the basalt and permafrost layers.

Contour Intervals: 1200, 1100, 1000, 900, 800, 700, 600, 500, 490, 480, 470, 460, 450, 440, 430, 420, 410, 400, 390, 380, 370, 360, 350, 340, 339, 338, 337, 336

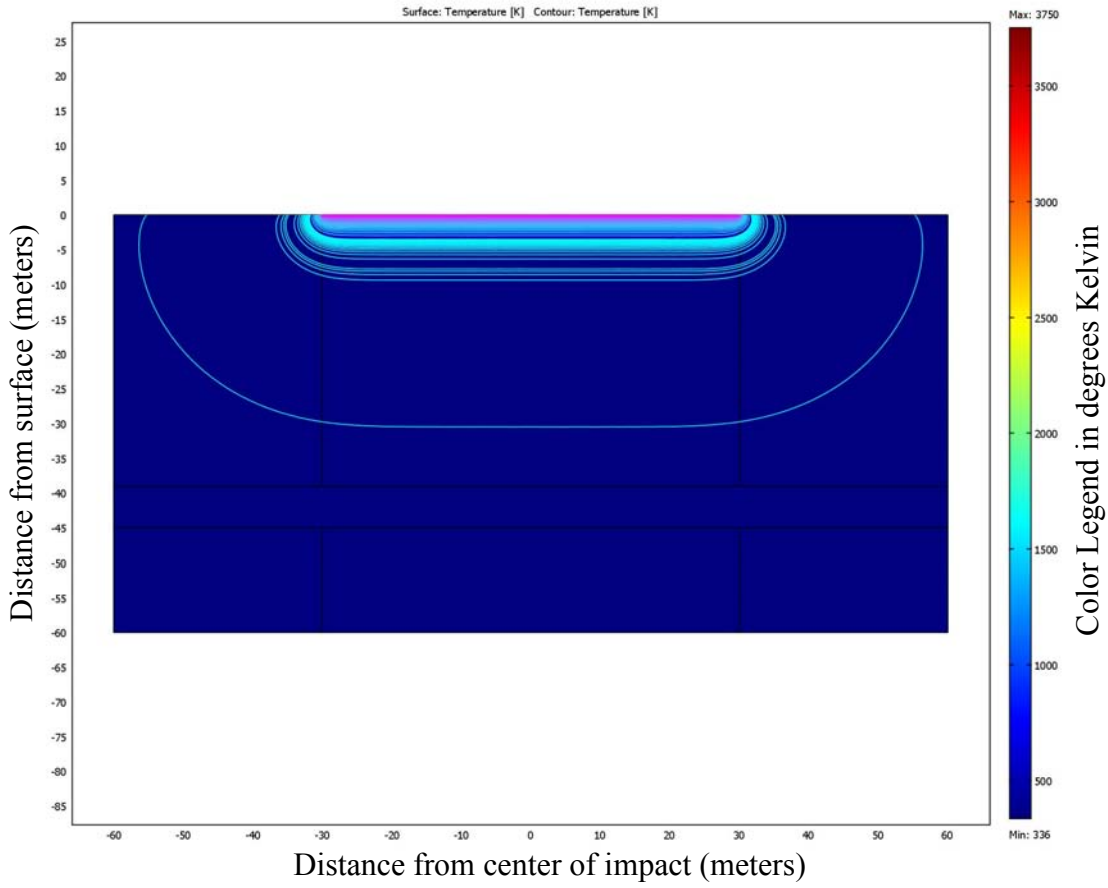

Figure 37: COMSOL generated image of a basalt, permafrost, basalt stratigraphic column. The permafrost layer is 6 meters thick at a depth of 39 meters. This model is 3 times that of Figure 36. The vertical black lines can be ignored and in no way effect the resulting model. The horizontal black lines indicate the contact boundary between the basalt and permafrost layers.

Contour Intervals: 3700, 3600, 3500, 3400, 3300, 3200, 3100, 3000, 2900, 2800, 2700, 2600, 2500, 2400, 2300, 2200, 2100, 2000, 1900, 1800, 1700, 1600, 1500, 1400, 1300, 1200, 1100, 1000, 900, 800, 700, 600, 500, 490, 480, 470, 460, 450, 440, 430, 420, 410, 400, 390, 380, 370, 360, 350, 340, 339, 338, 337, 336

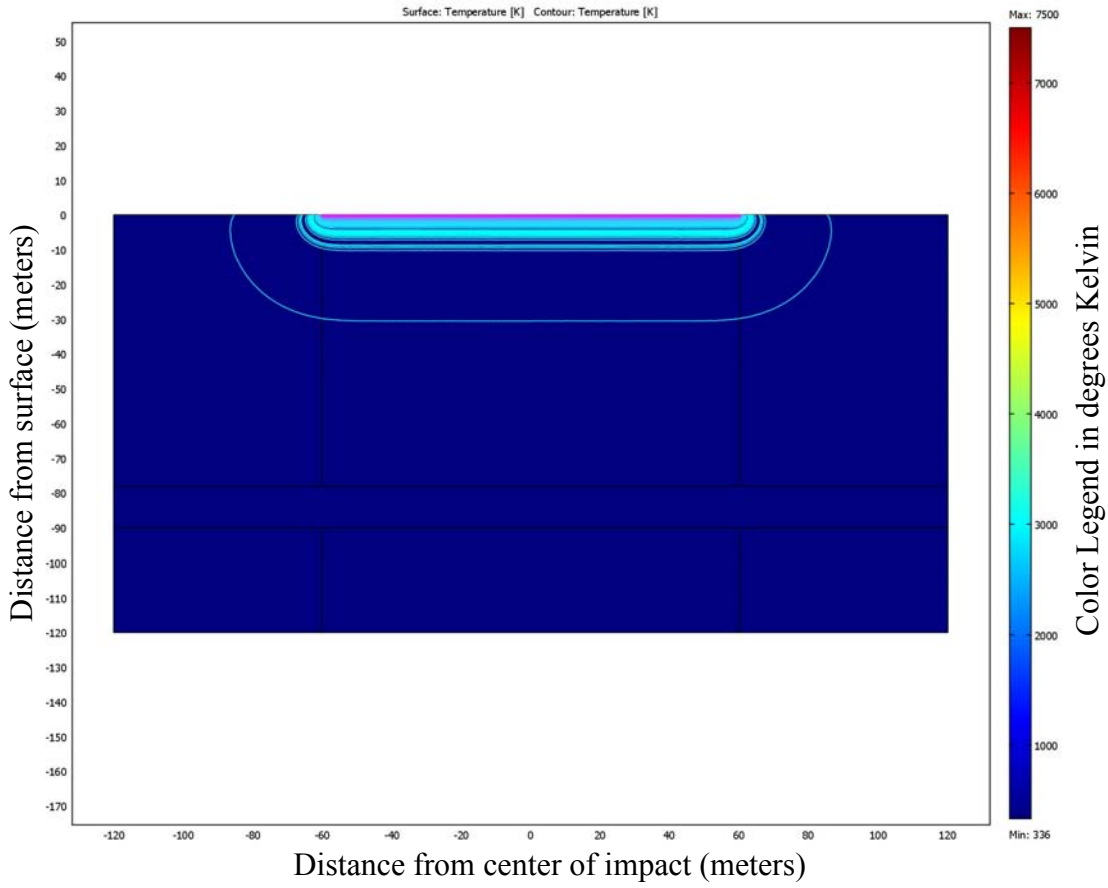

Figure 38: COMSOL generated image of a basalt, permafrost, basalt stratigraphic column. The permafrost layer is 12 meters thick at a depth of 78 meters. This model is 6 times that of Figure 36. The vertical black lines can be ignored and in no way effect the resulting model. The horizontal black lines indicate the contact boundary between the basalt and permafrost layers.

Contour Intervals: 7500, 7400, 7300, 7200, 7100, 7000, 6900, 6800, 6700, 6600, 6500, 6400, 6300, 6200, 6100, 6000, 5900, 5800, 5700, 5600, 5500, 5400, 5300, 5200, 5100, 5000, 4900, 4800, 4700, 4600, 4500, 4400, 4300, 4200, 4100, 4000, 3900, 3800, 3700, 3600, 3500, 3400, 3300, 3200, 3100, 3000, 2900, 2800, 2700, 2600, 2500, 2400, 2300, 2200, 2100, 2000, 1900, 1800, 1700, 1600, 1500, 1400, 1300, 1200, 1100, 1000, 900, 800, 700, 600, 500, 490, 480, 470, 460, 450, 440, 430, 420, 410, 400, 390, 380, 370, 360, 350, 340, 339, 338, 337, 336

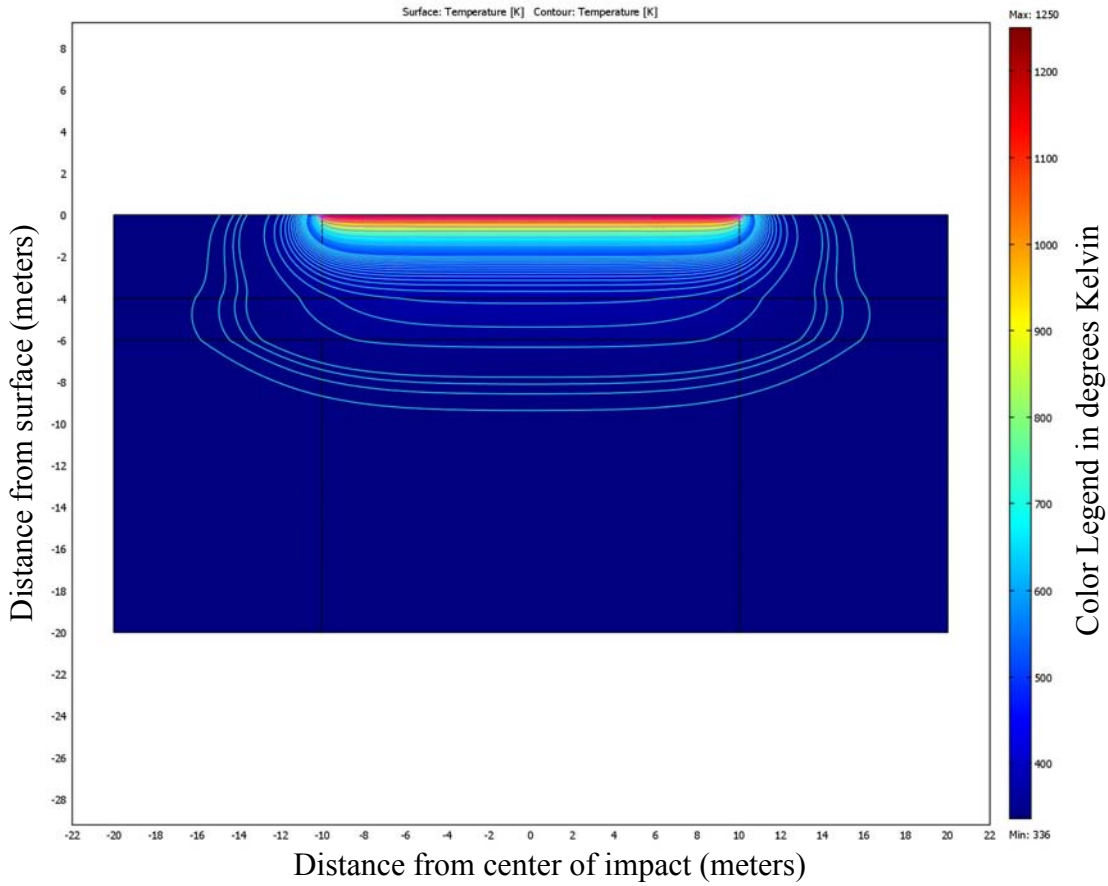

Figure 39: COMSOL generated image of a basalt, permafrost, basalt stratigraphic column. The permafrost layer is 2 meters thick at a depth of 4 meters. The vertical black lines can be ignored and in no way effect the resulting model. The horizontal black lines indicate the contact boundary between the basalt and permafrost layers.

Contour Intervals: 1200, 1100, 1000, 900, 800, 700, 600, 500, 490, 480, 470, 460, 450, 440, 430, 420, 410, 400, 390, 380, 370, 360, 350, 340, 339, 338, 337, 336

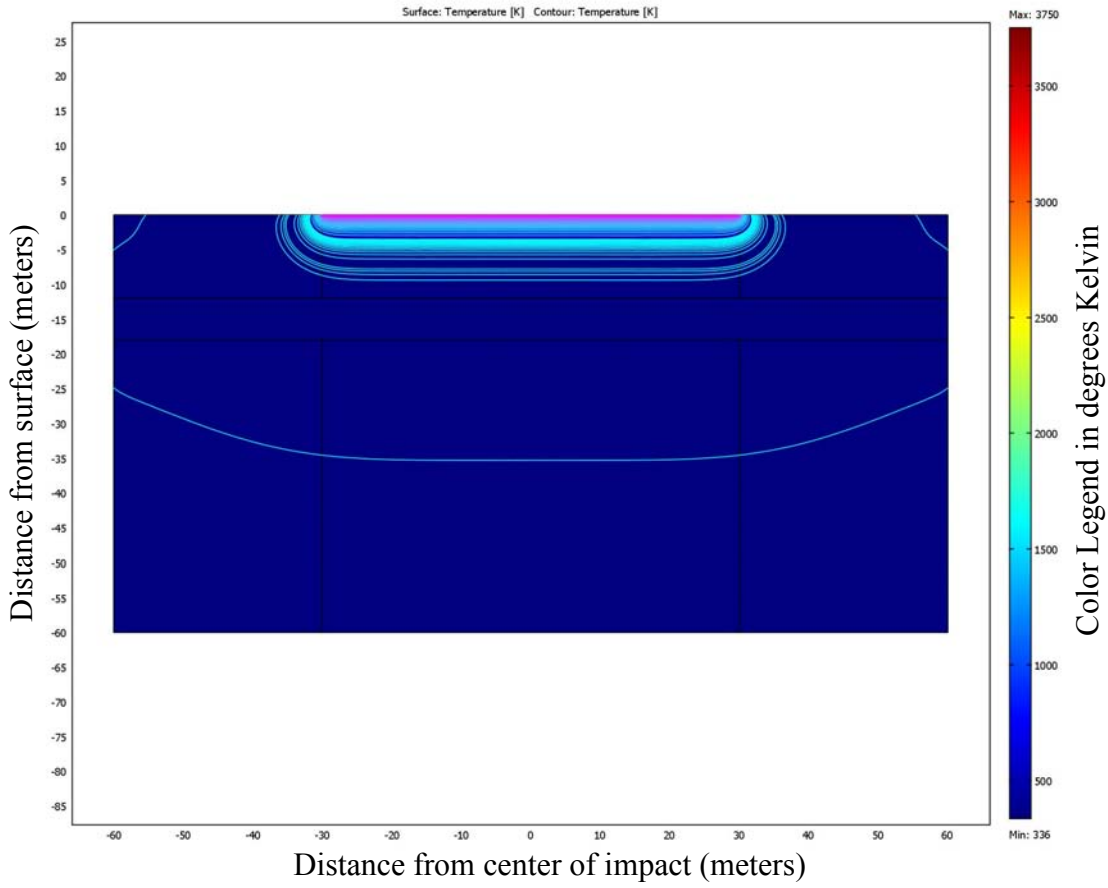

Figure 40: COMSOL generated image of a basalt, permafrost, basalt stratigraphic column. The permafrost layer is 6 meters thick at a depth of 12 meters. This model is 3 times that of Figure 39. The vertical black lines can be ignored and in no way effect the resulting model. The horizontal black lines indicate the contact boundary between the basalt and permafrost layers.

Contour Intervals: 3700, 3600, 3500, 3400, 3300, 3200, 3100, 3000, 2900, 2800, 2700, 2600, 2500, 2400, 2300, 2200, 2100, 2000, 1900, 1800, 1700, 1600, 1500, 1400, 1300, 1200, 1100, 1000, 900, 800, 700, 600, 500, 490, 480, 470, 460, 450, 440, 430, 420, 410, 400, 390, 380, 370, 360, 350, 340, 339, 338, 337, 336

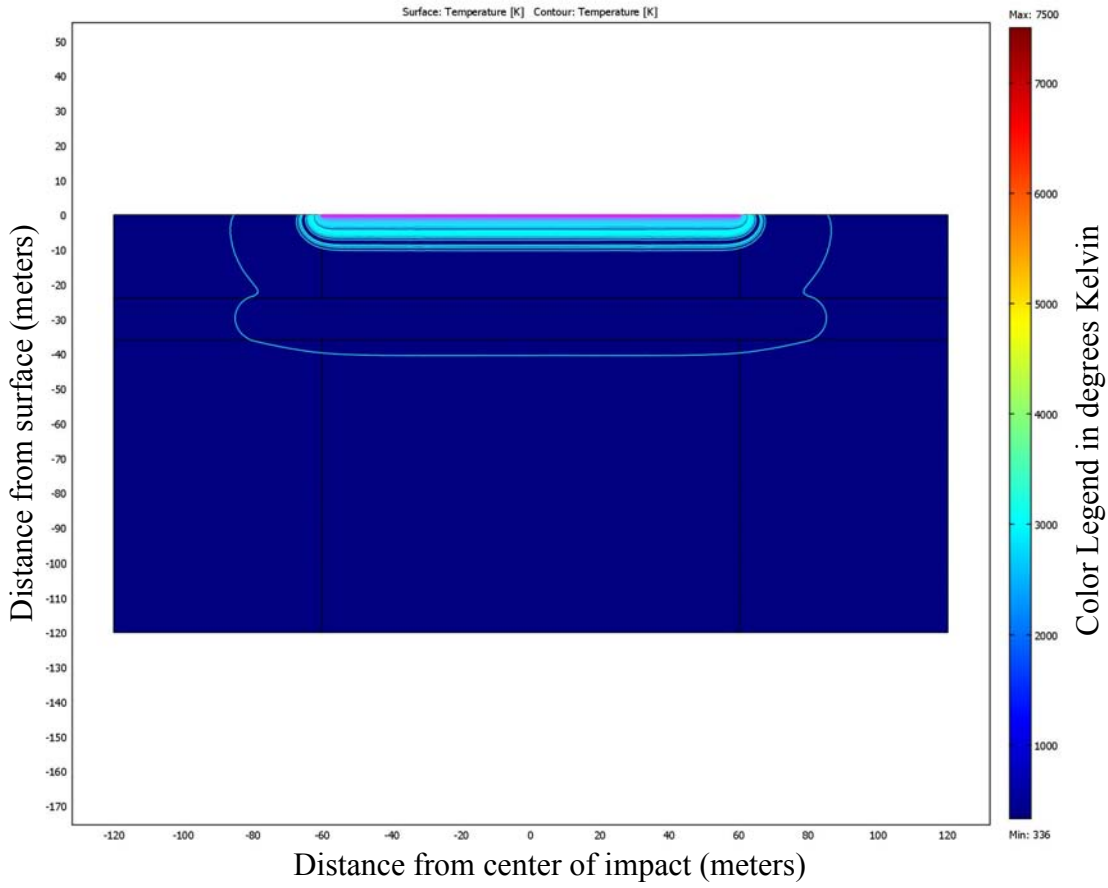

Figure 41: COMSOL generated image of a basalt, permafrost, basalt stratigraphic column. The permafrost layer is 12 meters thick at a depth of 24 meters. This model is 6 times that of Figure 39. The vertical black lines can be ignored and in no way effect the resulting model. The horizontal black lines indicate the contact boundary between the basalt and permafrost layers.

Contour Intervals: 7500, 7400, 7300, 7200, 7100, 7000, 6900, 6800, 6700, 6600, 6500, 6400, 6300, 6200, 6100, 6000, 5900, 5800, 5700, 5600, 5500, 5400, 5300, 5200, 5100, 5000, 4900, 4800, 4700, 4600, 4500, 4400, 4300, 4200, 4100, 4000, 3900, 3800, 3700, 3600, 3500, 3400, 3300, 3200, 3100, 3000, 2900, 2800, 2700, 2600, 2500, 2400, 2300, 2200, 2100, 2000, 1900, 1800, 1700, 1600, 1500, 1400, 1300, 1200, 1100, 1000, 900, 800, 700, 600, 500, 490, 480, 470, 460, 450, 440, 430, 420, 410, 400, 390, 380, 370, 360, 350, 340, 339, 338, 337, 336

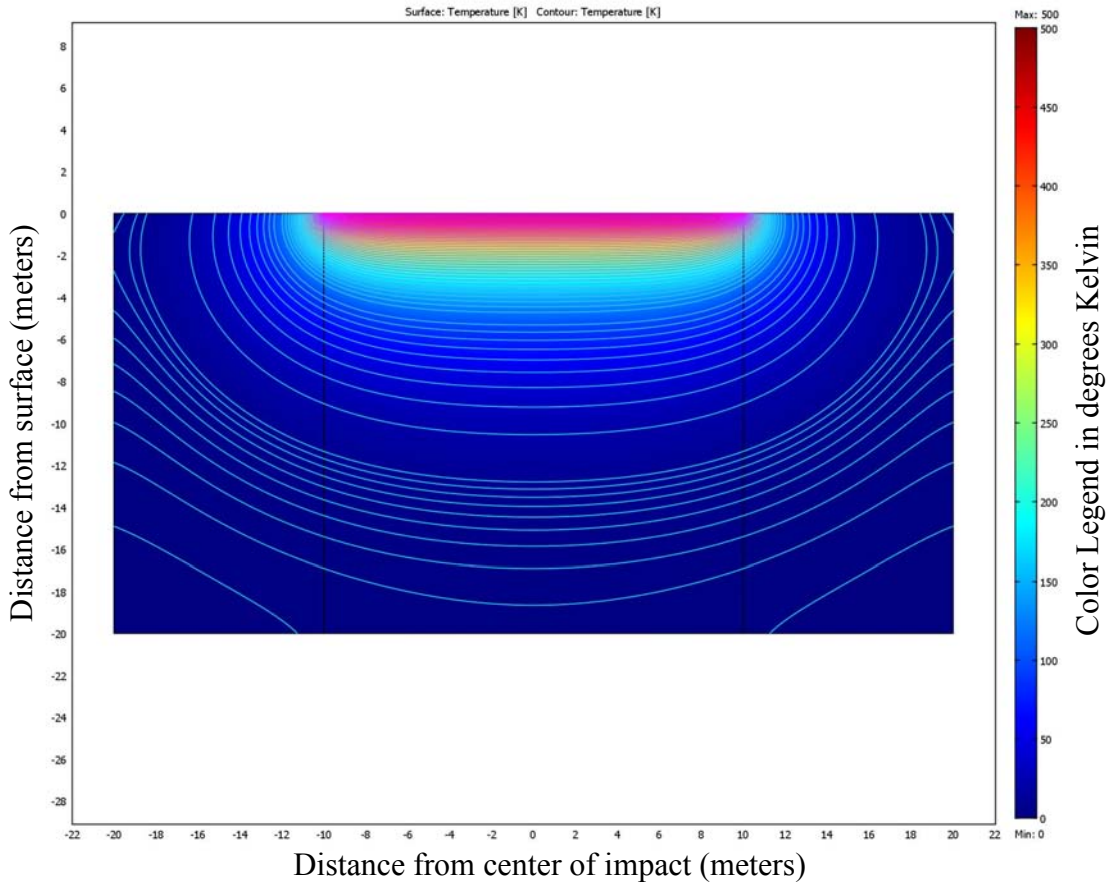

Figure 42: COMSOL generated image of a homogeneous epsomite stratigraphic column. The epsomite layer is 20 meters thick. The vertical black lines can be ignored and in no way effect the resulting model.

Contour Intervals: 500, 490, 480, 470, 460, 450, 440, 430, 420, 410, 400, 390, 380, 370, 360, 350, 340, 330, 320, 310, 300, 290, 280, 270, 260, 250, 240, 230, 220, 210, 200, 190, 180, 170, 160, 150, 140, 130, 120, 100, 90, 80, 70, 60, 50, 40, 30, 20, 10, 9, 8, 7, 6, 5, 4, 3, 2, 1

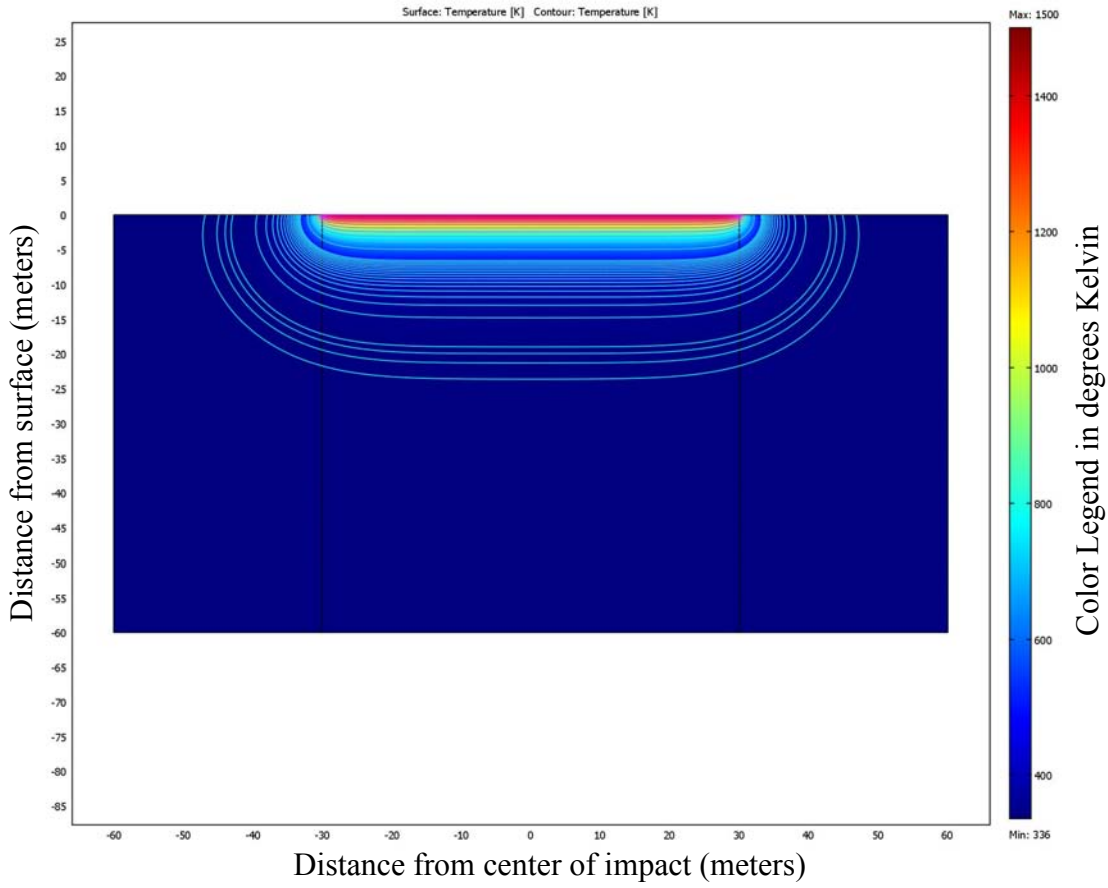

Figure 43: COMSOL generated image of a homogeneous epsomite stratigraphic column. The epsomite layer is 60 meters thick. This model is 3 times that of Figure 42. The vertical black lines can be ignored and in no way effect the resulting model.

Contour Intervals: 1500, 1400, 1300, 1200, 1100, 1000, 900, 800, 700, 600, 500, 490, 480, 470, 460, 450, 440, 430, 420, 410, 400, 390, 380, 370, 360, 350, 340, 339, 338, 337, 336

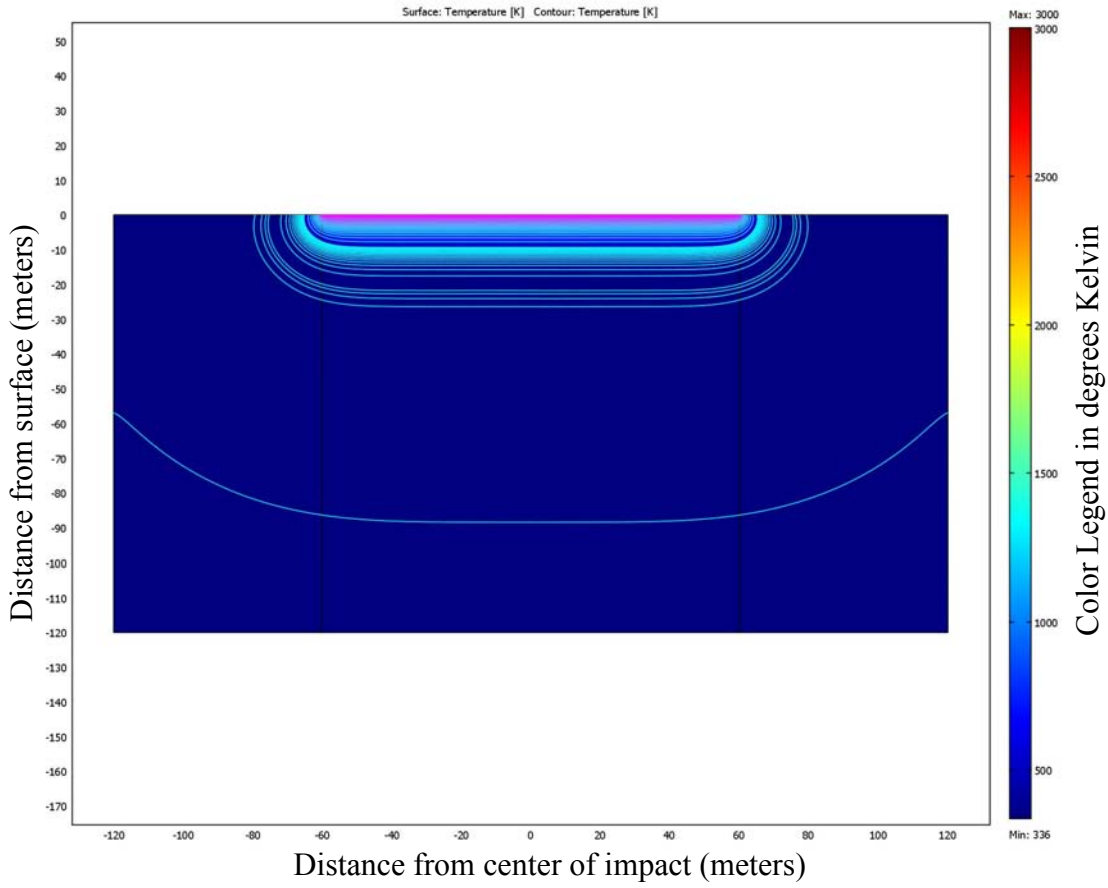

Figure 44: COMSOL generated image of a homogeneous epsomite stratigraphic column. The epsomite layer is 120 meters thick. This model is 6 times that of Figure 42. The vertical black lines can be ignored and in no way effect the resulting model.

Contour Intervals: 3000, 2900, 2800, 2700, 2600, 2500, 2400, 2300, 2200, 2100, 2000, 1900, 1800, 1700, 1600, 1500, 1400, 1300, 1200, 1100, 1000, 900, 800, 700, 600, 500, 490, 480, 470, 460, 450, 440, 430, 420, 410, 400, 390, 380, 370, 360, 350, 340, 339, 338, 337, 336

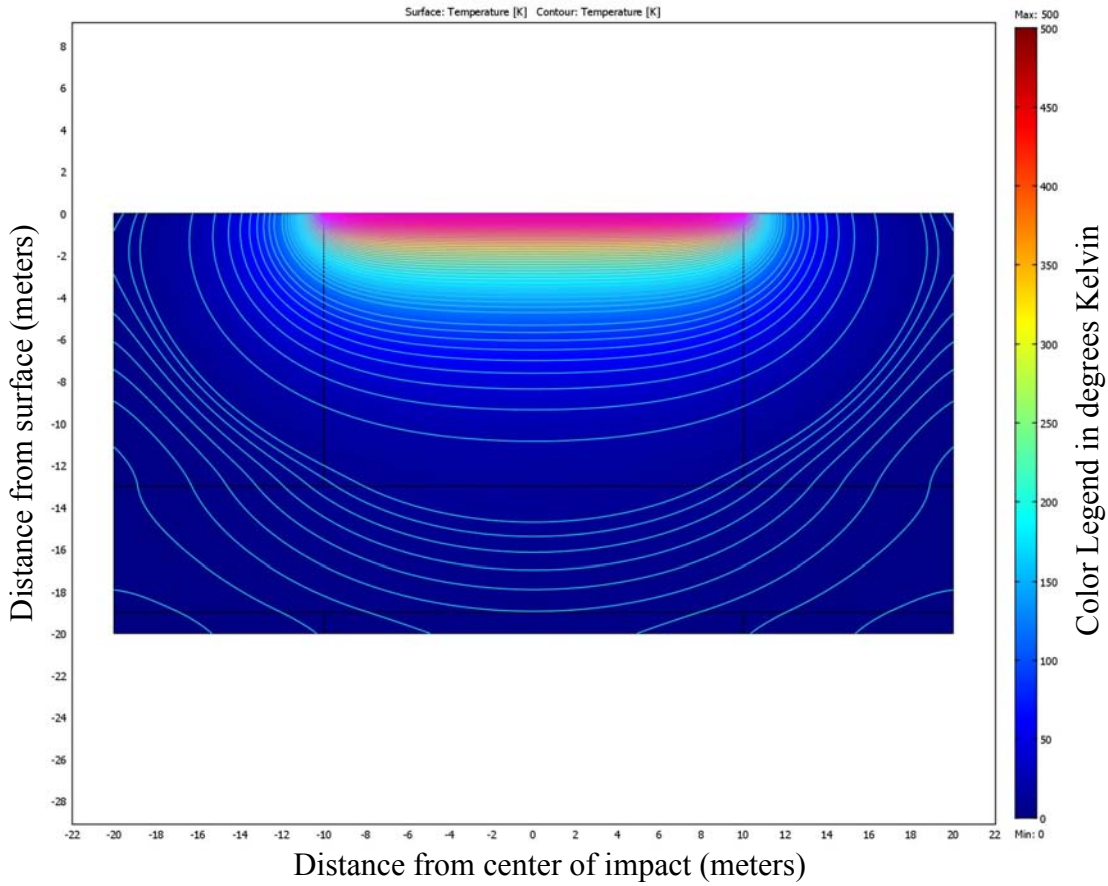

Figure 45: COMSOL generated image of an epsomite, permafrost, epsomite stratigraphic column. The permafrost layer is 6 meters thick at a depth of 13 meters. The vertical black lines can be ignored and in no way effect the resulting model. The horizontal black lines indicate the contact boundary between the basalt and permafrost layers.

Contour Intervals: 500, 490, 480, 470, 460, 450, 440, 430, 420, 410, 400, 390, 380, 370, 360, 350, 340, 330, 320, 310, 300, 290, 280, 270, 260, 250, 240, 230, 220, 210, 200, 190, 180, 170, 160, 150, 140, 130, 120, 100, 90, 80, 70, 60, 50, 40, 30, 20, 10, 9, 8, 7, 6, 5, 4, 3, 2, 1

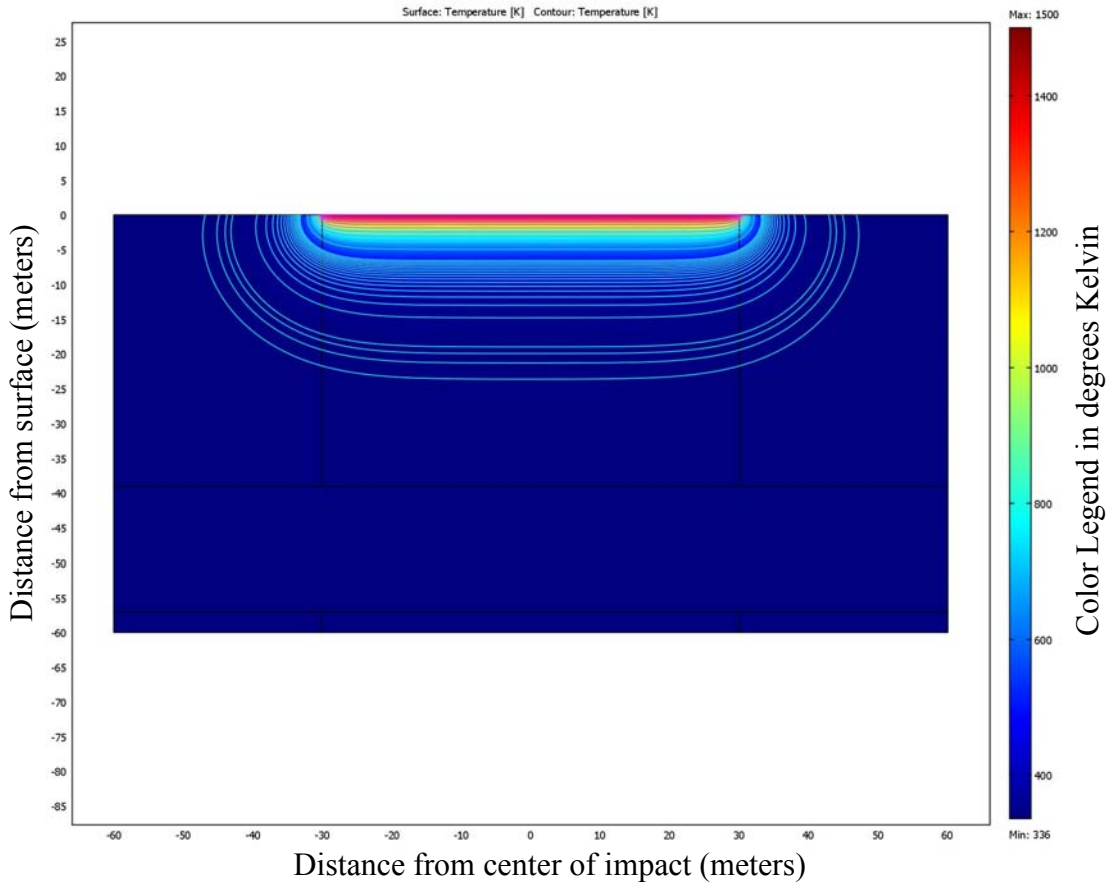

Figure 46: COMSOL generated image of an epsomite, permafrost, epsomite stratigraphic column. The permafrost layer is 18 meters thick at a depth of 39 meters. This model is 3 times that of Figure 45. The vertical black lines can be ignored and in no way effect the resulting model. The horizontal black lines indicate the contact boundary between the basalt and permafrost layers.

Contour Intervals: 1500, 1400, 1300, 1200, 1100, 1000, 900, 800, 700, 600, 500, 490, 480, 470, 460, 450, 440, 430, 420, 410, 400, 390, 380, 370, 360, 350, 340, 339, 338, 337, 336

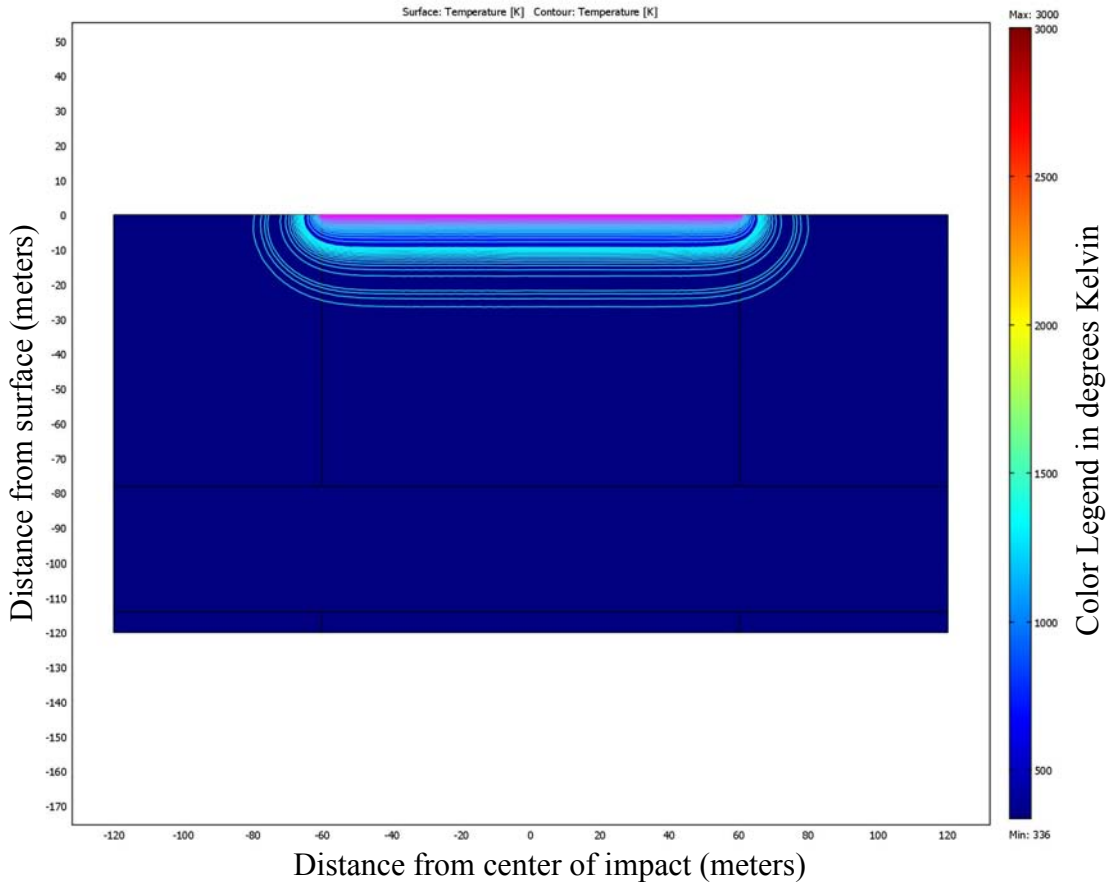

Figure 47: COMSOL generated image of an epsomite, permafrost, epsomite stratigraphic column. The permafrost layer is 36 meters thick at a depth of 78 meters. This model is 6 times that of Figure 45. The vertical black lines can be ignored and in no way effect the resulting model. The horizontal black lines indicate the contact boundary between the basalt and permafrost layers.

Contour Intervals: 3000, 2900, 2800, 2700, 2600, 2500, 2400, 2300, 2200, 2100, 2000, 1900, 1800, 1700, 1600, 1500, 1400, 1300, 1200, 1100, 1000, 900, 800, 700, 600, 500, 490, 480, 470, 460, 450, 440, 430, 420, 410, 400, 390, 380, 370, 360, 350, 340, 339, 338, 337, 336

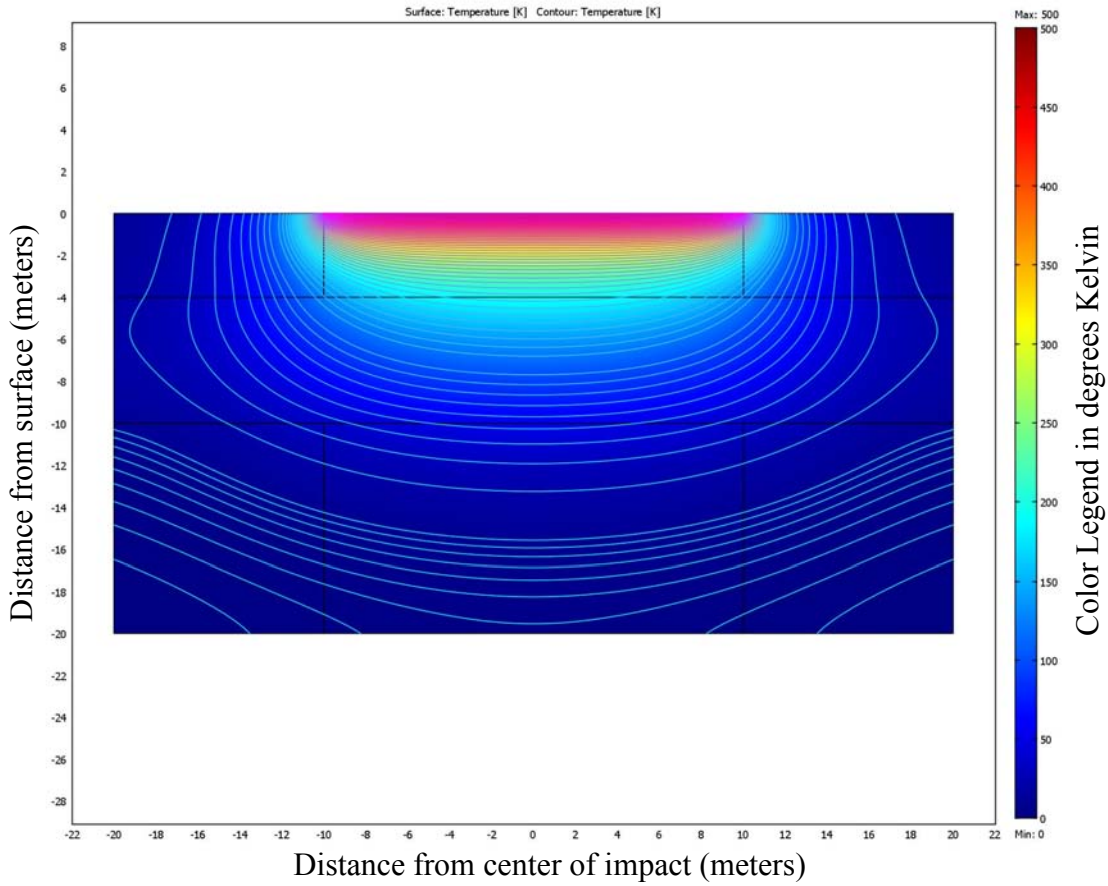

Figure 48: COMSOL generated image of an epsomite, permafrost, epsomite stratigraphic column. The permafrost layer is 6 meters thick at a depth of 4 meters. The vertical black lines can be ignored and in no way effect the resulting model. The horizontal black lines indicate the contact boundary between the basalt and permafrost layers.

Contour Intervals: 500, 490, 480, 470, 460, 450, 440, 430, 420, 410, 400, 390, 380, 370, 360, 350, 340, 330, 320, 310, 300, 290, 280, 270, 260, 250, 240, 230, 220, 210, 200, 190, 180, 170, 160, 150, 140, 130, 120, 100, 90, 80, 70, 60, 50, 40, 30, 20, 10, 9, 8, 7, 6, 5, 4, 3, 2, 1

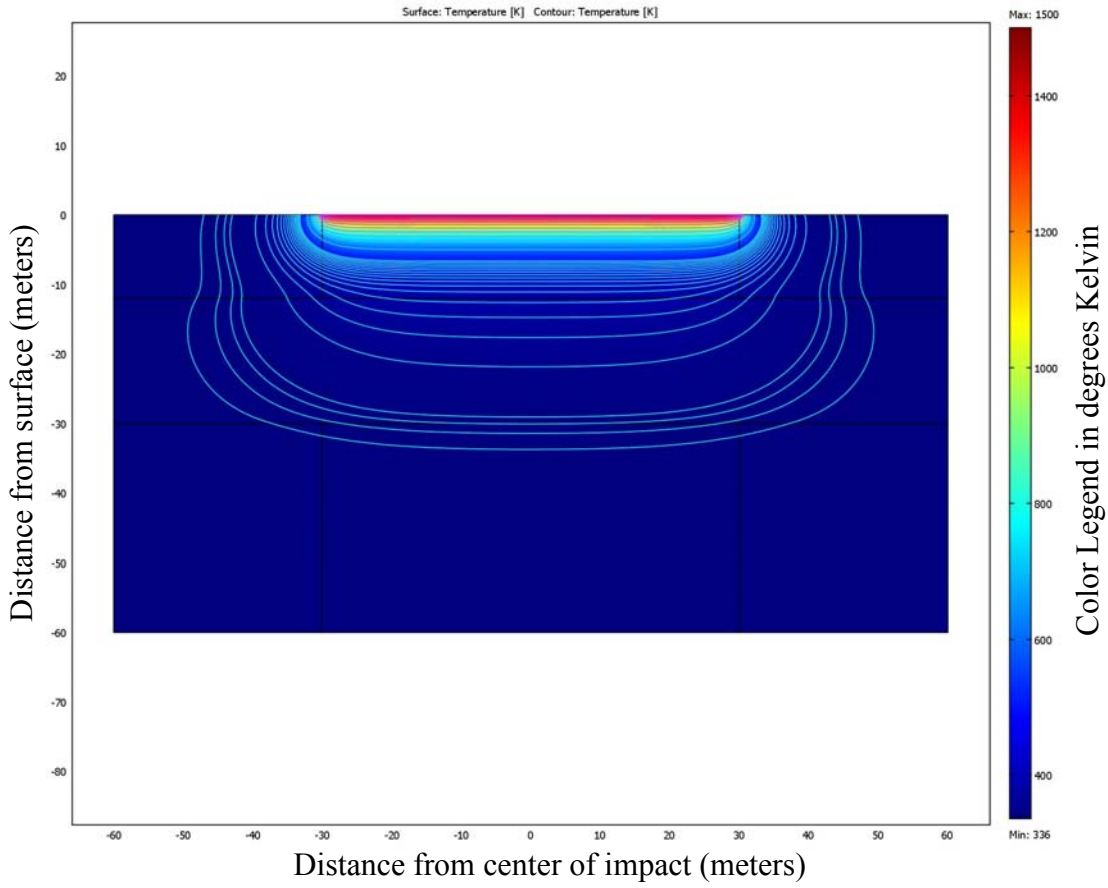

Figure 49: COMSOL generated image of an epsomite, permafrost, epsomite stratigraphic column. The permafrost layer is 18 meters thick at a depth of 12 meters. This model is 3 times that of Figure 48. The vertical black lines can be ignored and in no way effect the resulting model. The horizontal black lines indicate the contact boundary between the basalt and permafrost layers.

Contour Intervals: 1500, 1400, 1300, 1200, 1100, 1000, 900, 800, 700, 600, 500, 490, 480, 470, 460, 450, 440, 430, 420, 410, 400, 390, 380, 370, 360, 350, 340, 339, 338, 337, 336

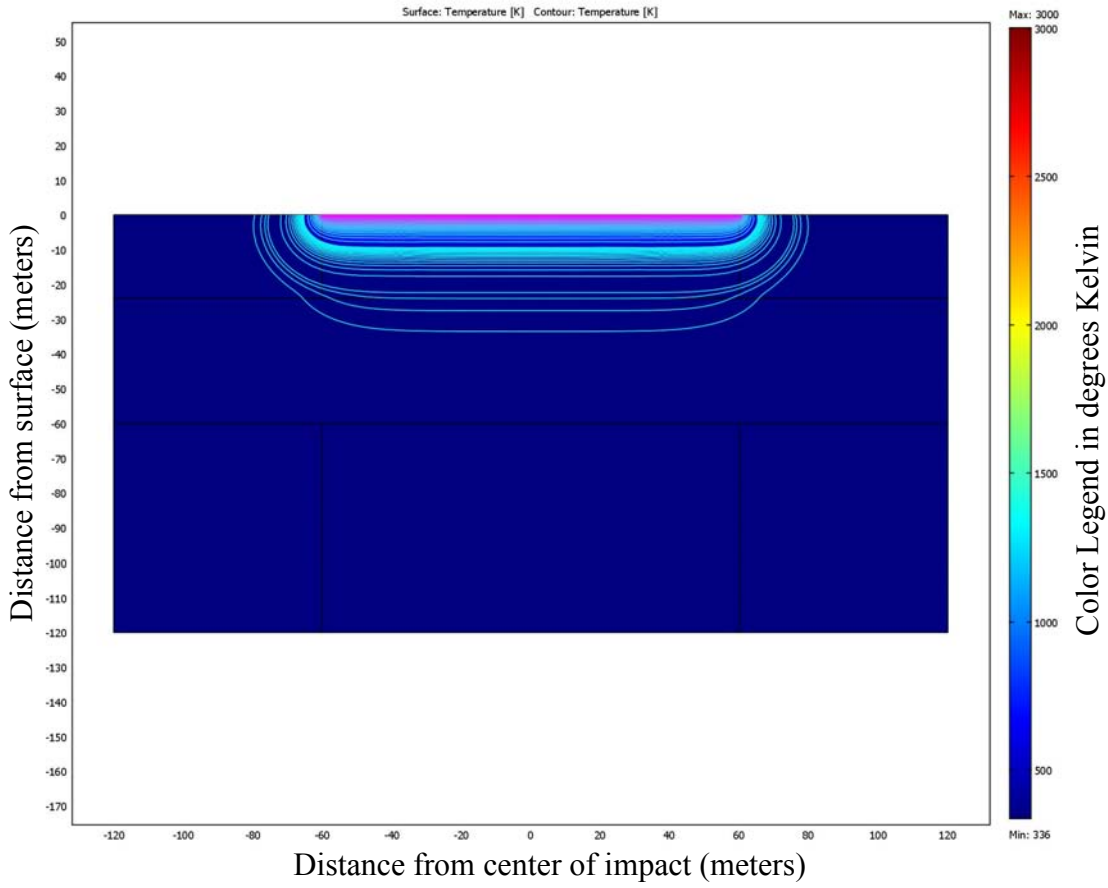

Figure 50: COMSOL generated image of an epsomite, permafrost, epsomite stratigraphic column. The permafrost layer is 36 meters thick at a depth of 24 meters. This model is 6 times that of Figure 48. The vertical black lines can be ignored and in no way effect the resulting model. The horizontal black lines indicate the contact boundary between the basalt and permafrost layers.

Contour Intervals: 3000, 2900, 2800, 2700, 2600, 2500, 2400, 2300, 2200, 2100, 2000, 1900, 1800, 1700, 1600, 1500, 1400, 1300, 1200, 1100, 1000, 900, 800, 700, 600, 500, 490, 480, 470, 460, 450, 440, 430, 420, 410, 400, 390, 380, 370, 360, 350, 340, 339, 338, 337, 336

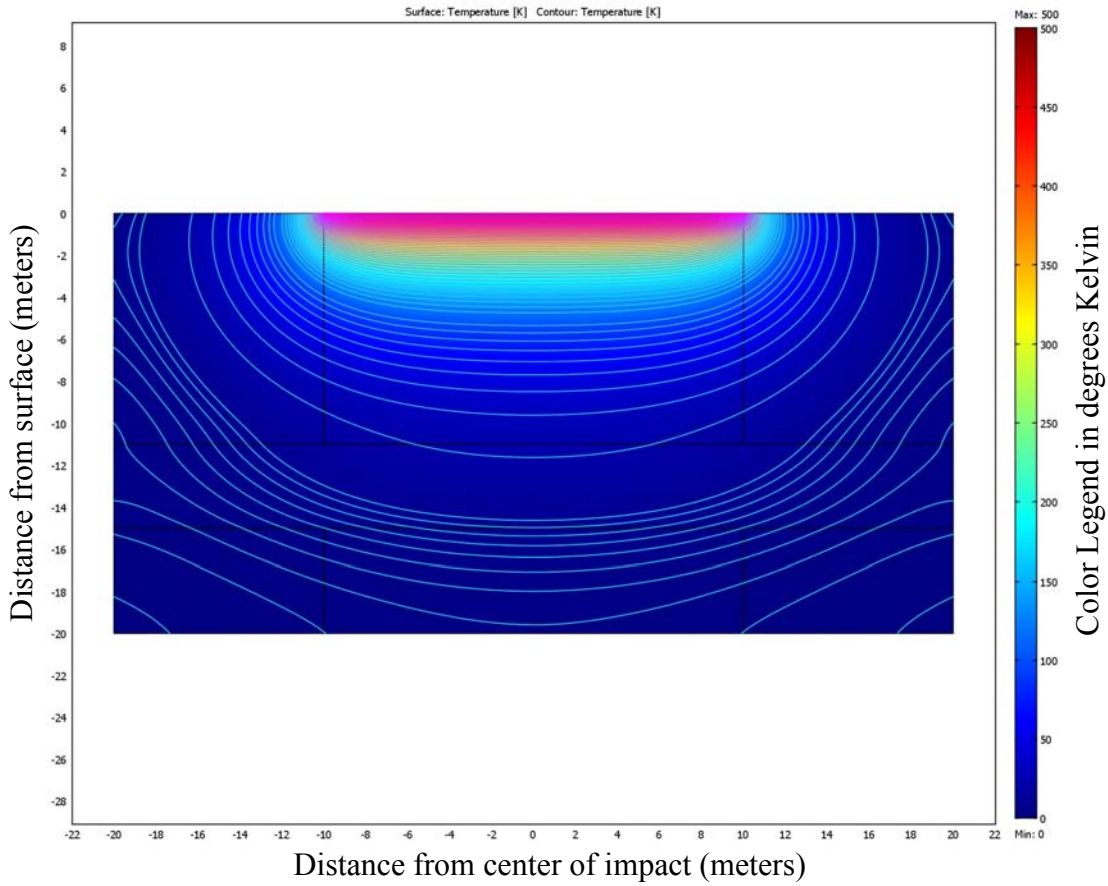

Figure 51: COMSOL generated image of an epsomite, permafrost, epsomite stratigraphic column. The permafrost layer is 2 meters thick at a depth of 13 meters. The vertical black lines can be ignored and in no way effect the resulting model. The horizontal black lines indicate the contact boundary between the basalt and permafrost layers.

Contour Intervals: 500, 490, 480, 470, 460, 450, 440, 430, 420, 410, 400, 390, 380, 370, 360, 350, 340, 330, 320, 310, 300, 290, 280, 270, 260, 250, 240, 230, 220, 210, 200, 190, 180, 170, 160, 150, 140, 130, 120, 100, 90, 80, 70, 60, 50, 40, 30, 20, 10, 9, 8, 7, 6, 5, 4, 3, 2, 1

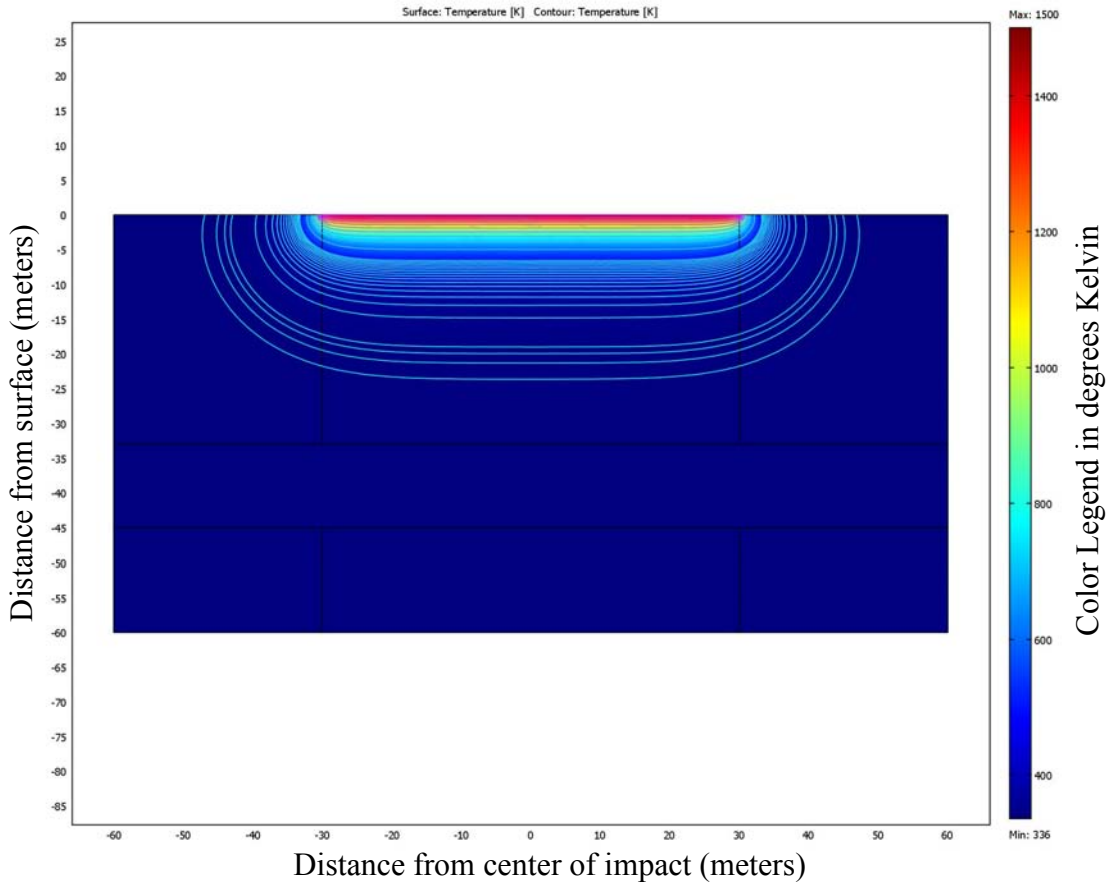

Figure 52: COMSOL generated image of an epsomite, permafrost, epsomite stratigraphic column. The permafrost layer is 6 meters thick at a depth of 39 meters. This model is 3 times that of Figure 51. The vertical black lines can be ignored and in no way effect the resulting model. The horizontal black lines indicate the contact boundary between the basalt and permafrost layers.

Contour Intervals: 1500, 1400, 1300, 1200, 1100, 1000, 900, 800, 700, 600, 500, 490, 480, 470, 460, 450, 440, 430, 420, 410, 400, 390, 380, 370, 360, 350, 340, 339, 338, 337, 336

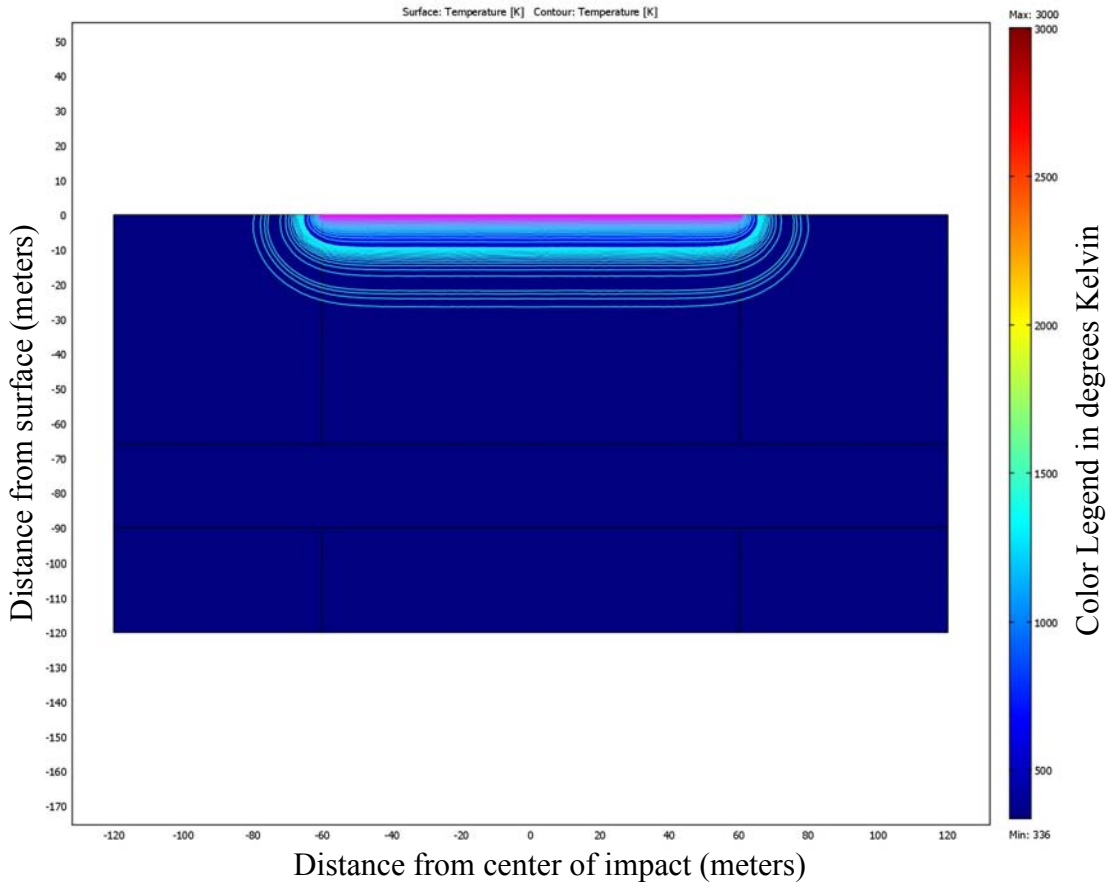

Figure 53: COMSOL generated image of an epsomite, permafrost, epsomite stratigraphic column. The permafrost layer is 12 meters thick at a depth of 78 meters. This model is 6 times that of Figure 51. The vertical black lines can be ignored and in no way effect the resulting model. The horizontal black lines indicate the contact boundary between the basalt and permafrost layers.

Contour Intervals: 3000, 2900, 2800, 2700, 2600, 2500, 2400, 2300, 2200, 2100, 2000, 1900, 1800, 1700, 1600, 1500, 1400, 1300, 1200, 1100, 1000, 900, 800, 700, 600, 500, 490, 480, 470, 460, 450, 440, 430, 420, 410, 400, 390, 380, 370, 360, 350, 340, 339, 338, 337, 336

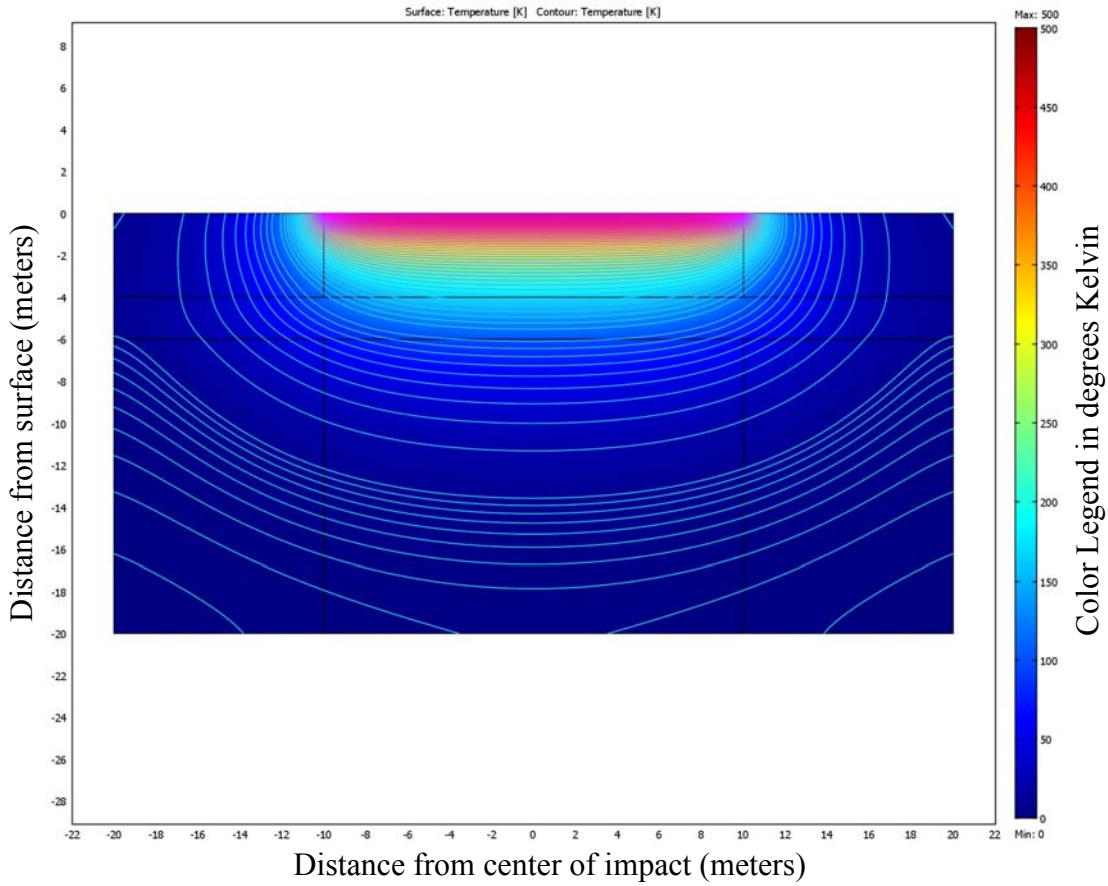

Figure 54: COMSOL generated image of an epsomite, permafrost, epsomite stratigraphic column. The permafrost layer is 2 meters thick at a depth of 4 meters. The vertical black lines can be ignored and in no way effect the resulting model. The horizontal black lines indicate the contact boundary between the basalt and permafrost layers.

Contour Intervals: 500, 490, 480, 470, 460, 450, 440, 430, 420, 410, 400, 390, 380, 370, 360, 350, 340, 330, 320, 310, 300, 290, 280, 270, 260, 250, 240, 230, 220, 210, 200, 190, 180, 170, 160, 150, 140, 130, 120, 100, 90, 80, 70, 60, 50, 40, 30, 20, 10, 9, 8, 7, 6, 5, 4, 3, 2, 1

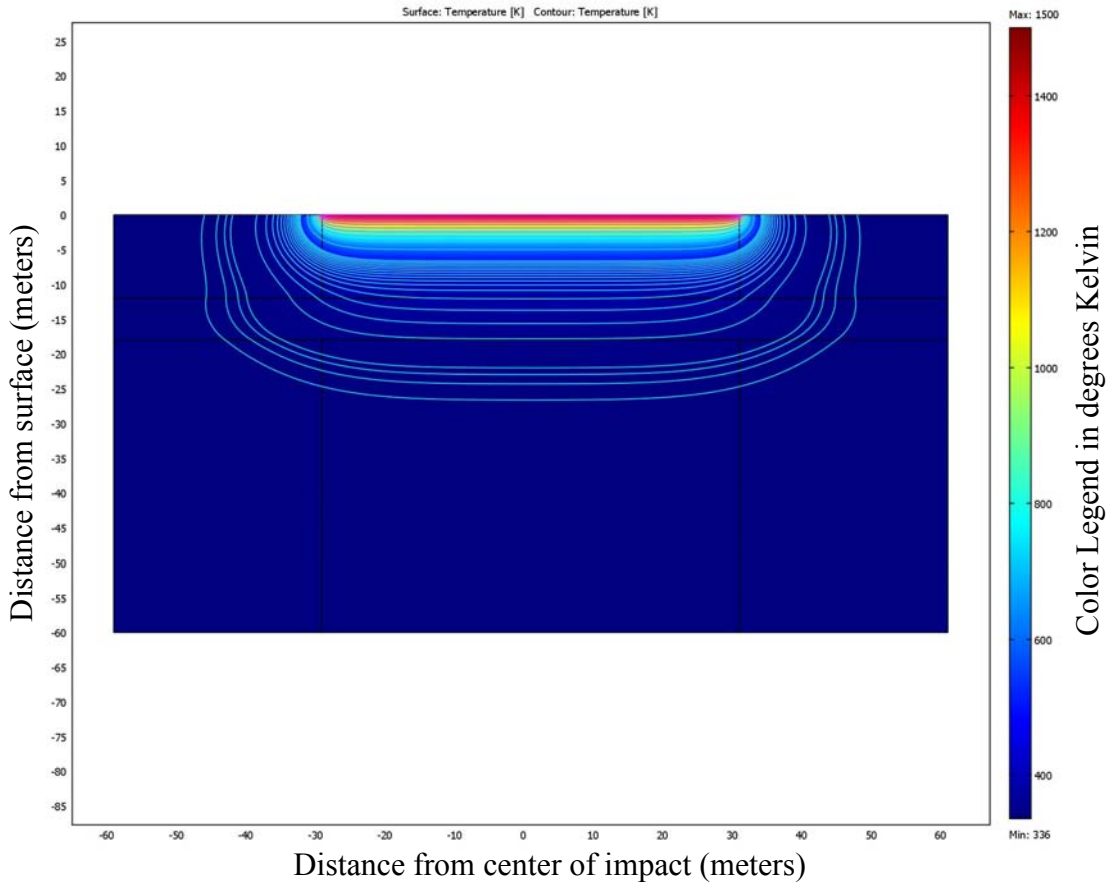

Figure 55: COMSOL generated image of an epsomite, permafrost, epsomite stratigraphic column. The permafrost layer is 6 meters thick at a depth of 12 meters. This model is 3 times that of Figure 54. The vertical black lines can be ignored and in no way effect the resulting model. The horizontal black lines indicate the contact boundary between the basalt and permafrost layers.

Contour Intervals: 1500, 1400, 1300, 1200, 1100, 1000, 900, 800, 700, 600, 500, 490, 480, 470, 460, 450, 440, 430, 420, 410, 400, 390, 380, 370, 360, 350, 340, 339, 338, 337, 336

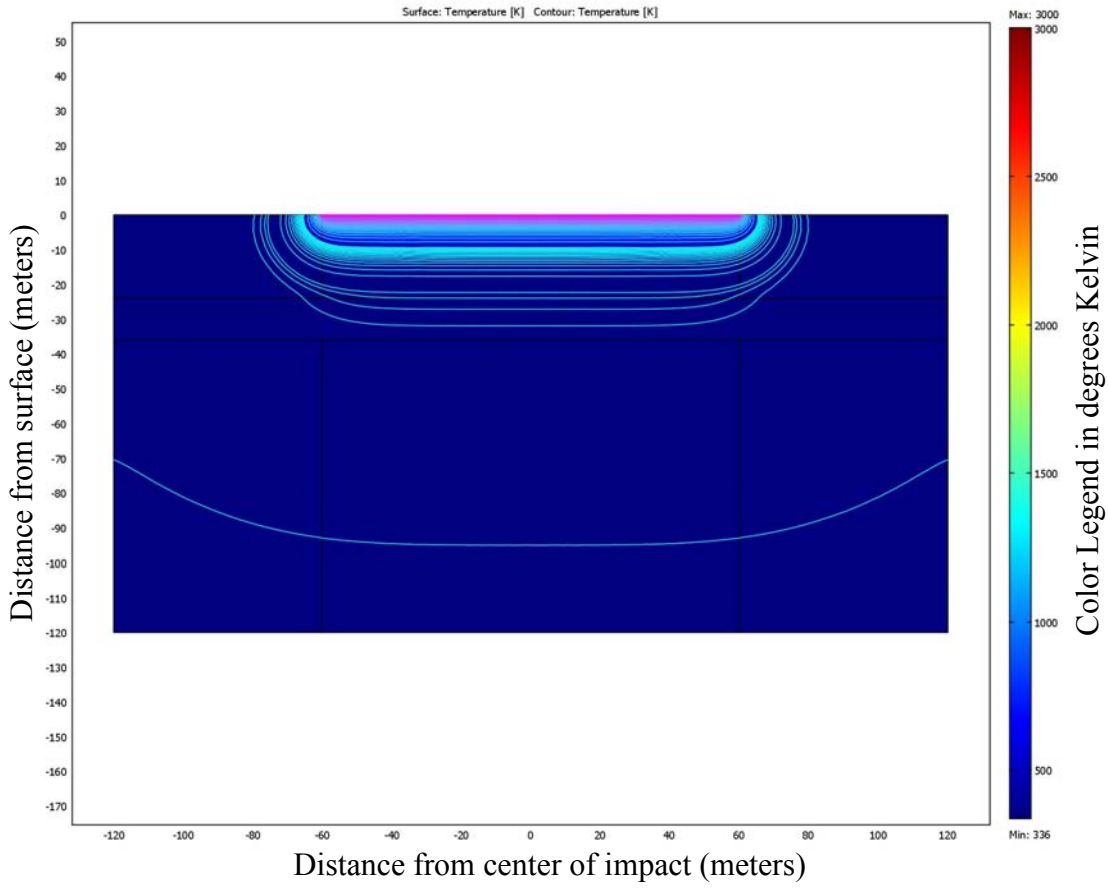

Figure 56: COMSOL generated image of an epsomite, permafrost, epsomite stratigraphic column. The permafrost layer is 12 meters thick at a depth of 24 meters. This model is 6 times that of Figure 54. The vertical black lines can be ignored and in no way effect the resulting model. The horizontal black lines indicate the contact boundary between the basalt and permafrost layers.

Contour Intervals: 3000, 2900, 2800, 2700, 2600, 2500, 2400, 2300, 2200, 2100, 2000, 1900, 1800, 1700, 1600, 1500, 1400, 1300, 1200, 1100, 1000, 900, 800, 700, 600, 500, 490, 480, 470, 460, 450, 440, 430, 420, 410, 400, 390, 380, 370, 360, 350, 340, 339, 338, 337, 336

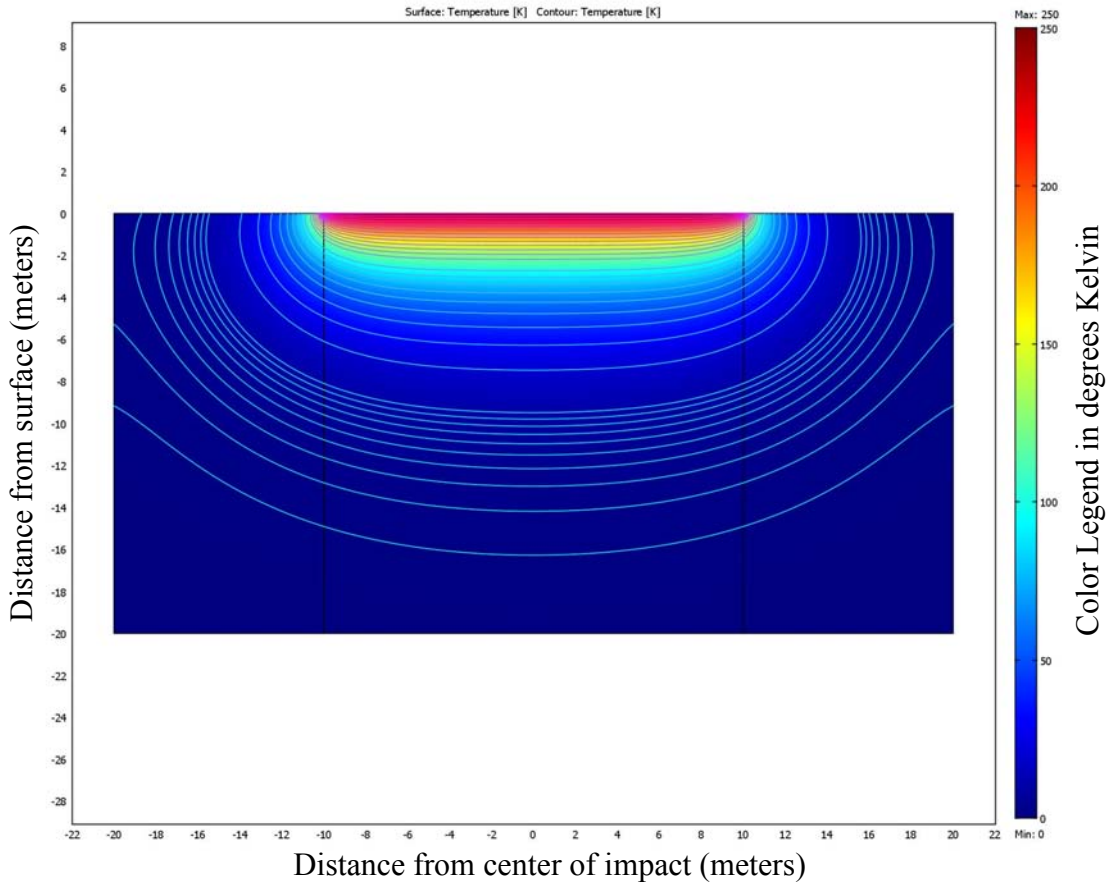

Figure 57: COMSOL generated image of a homogeneous gypsum stratigraphic column. The gypsum layer is 20 meters thick. The vertical black lines can be ignored and in no way effect the resulting model.

Contour Intervals: 250, 240, 230, 220, 210, 200, 190, 180, 170, 160, 150, 140, 130, 120, 100, 90, 80, 70, 60, 50, 40, 30, 20, 10, 9, 8, 7, 6, 5, 4, 3, 2, 1

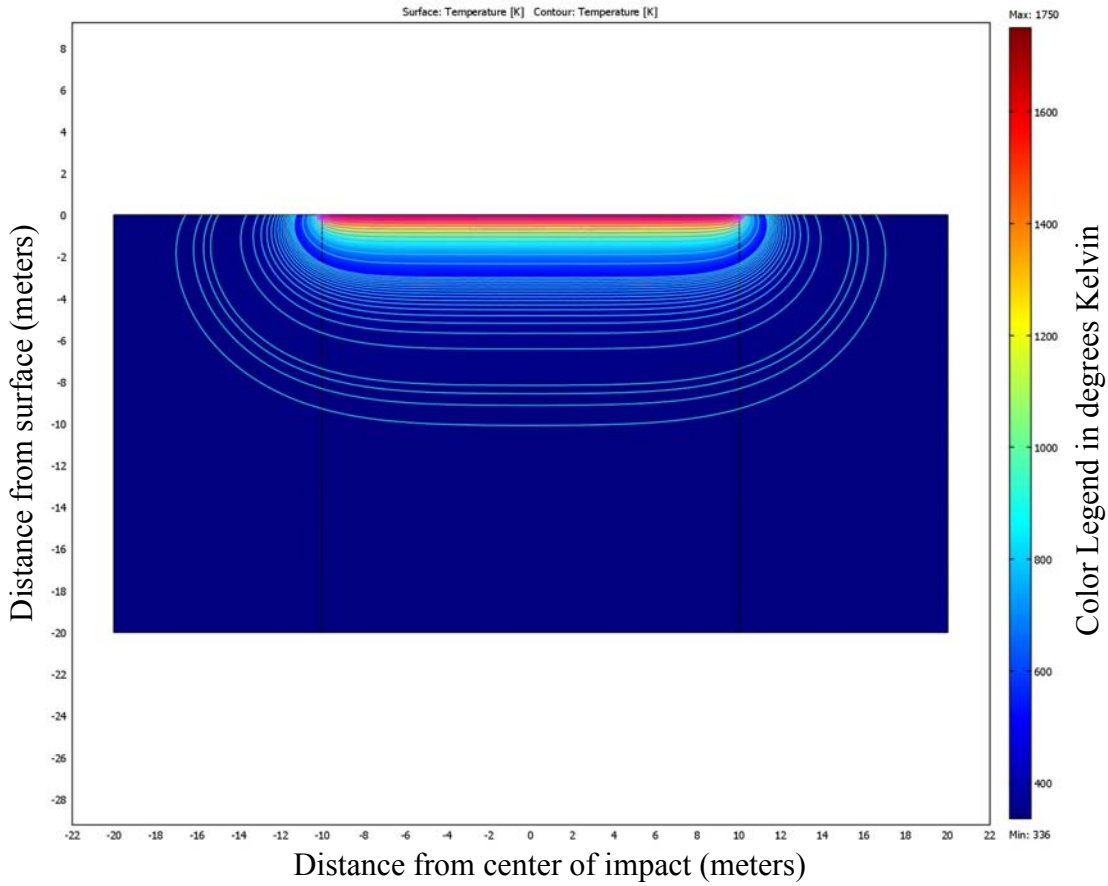

Figure 58: COMSOL generated image of a homogeneous gypsum stratigraphic column. The gypsum layer is 20 meters thick. The vertical black lines can be ignored and in no way effect the resulting model.

Contour Intervals: 1700, 1600, 1500, 1400, 1300, 1200, 1100, 1000, 900, 800, 700, 600, 500, 490, 480, 470, 460, 450, 440, 430, 420, 410, 400, 390, 380, 370, 360, 350, 340, 339, 338, 337, 336

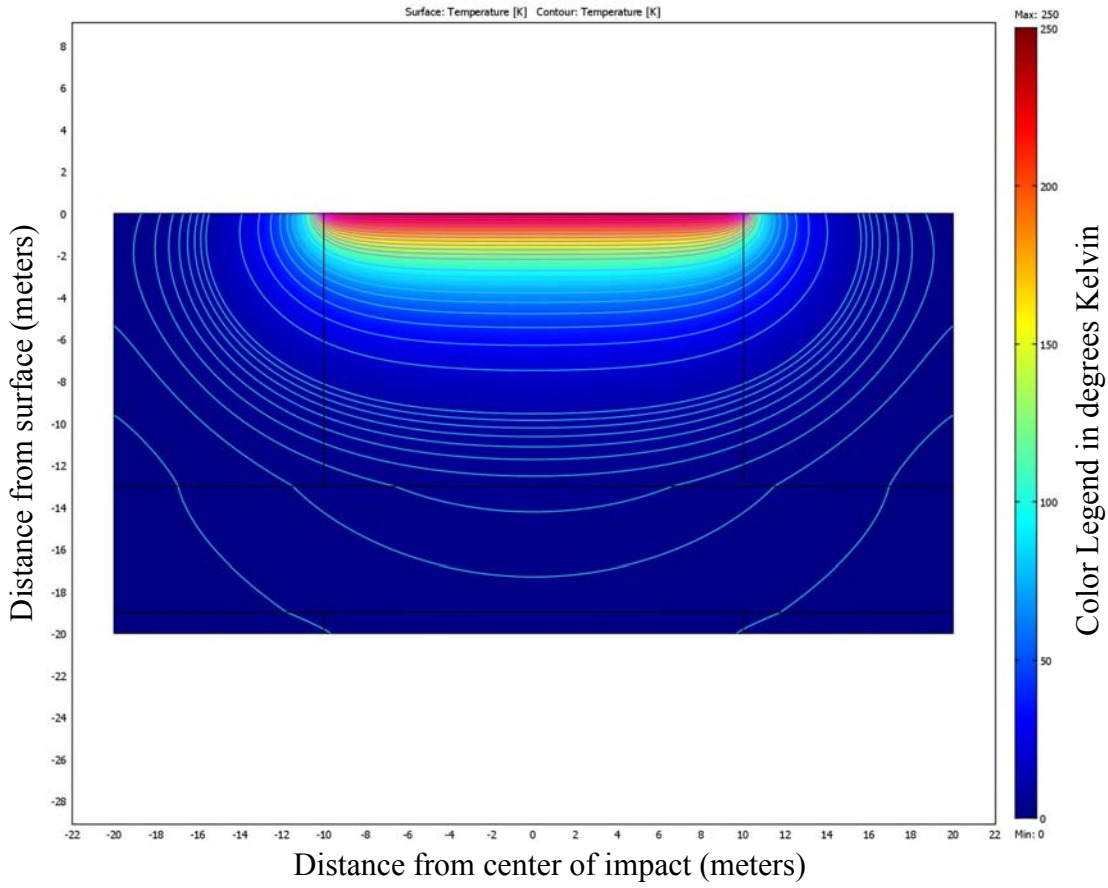

Figure 59: COMSOL generated image of a gypsum, permafrost, gypsum stratigraphic column. The permafrost layer is 6 meters thick at a depth of 13 meters. The vertical black lines can be ignored and in no way effect the resulting model. The horizontal black lines indicate the contact boundary between the basalt and permafrost layers.

Contour Intervals: 250, 240, 230, 220, 210, 200, 190, 180, 170, 160, 150, 140, 130, 120, 100, 90, 80, 70, 60, 50, 40, 30, 20, 10, 9, 8, 7, 6, 5, 4, 3, 2, 1

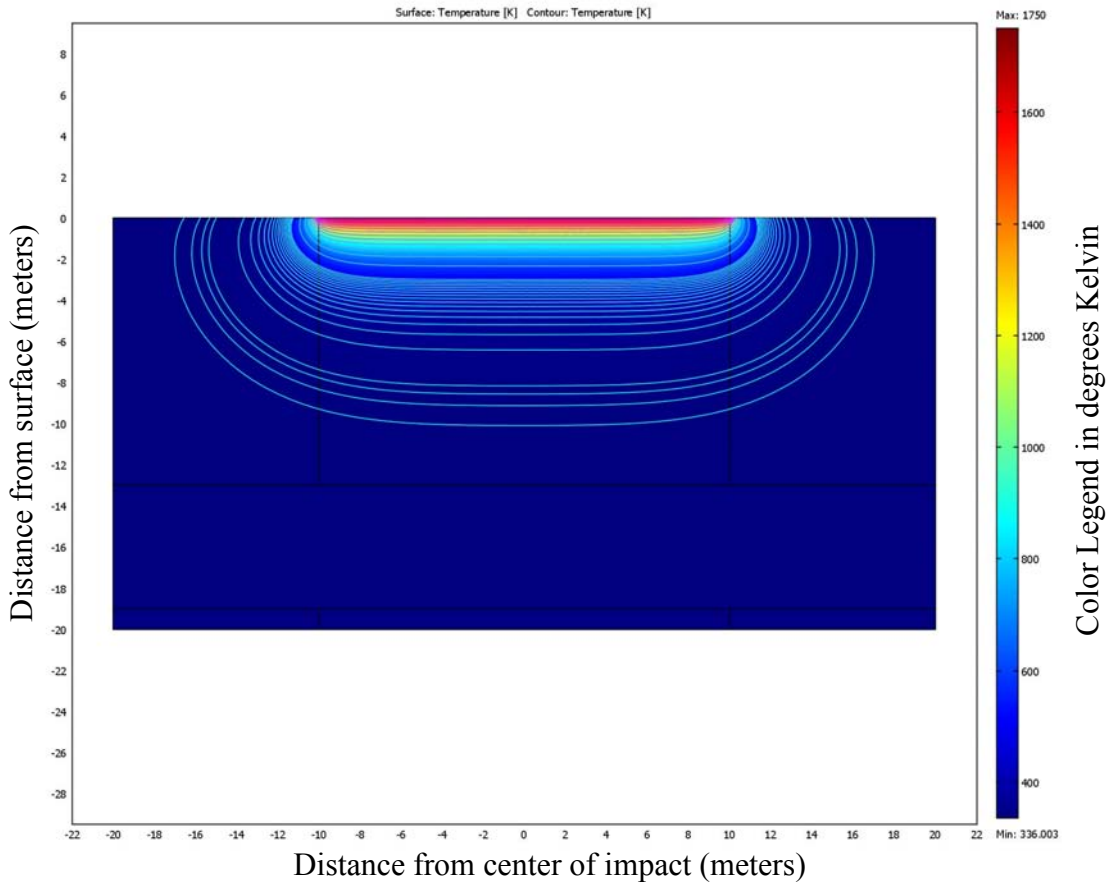

Figure 60: COMSOL generated image of a gypsum, permafrost, gypsum stratigraphic column. The permafrost layer is 6 meters thick at a depth of 13 meters. The vertical black lines can be ignored and in no way effect the resulting model. The horizontal black lines indicate the contact boundary between the basalt and permafrost layers.

Contour Intervals: 1700, 1600, 1500, 1400, 1300, 1200, 1100, 1000, 900, 800, 700, 600, 500, 490, 480, 470, 460, 450, 440, 430, 420, 410, 400, 390, 380, 370, 360, 350, 340, 339, 338, 337, 336

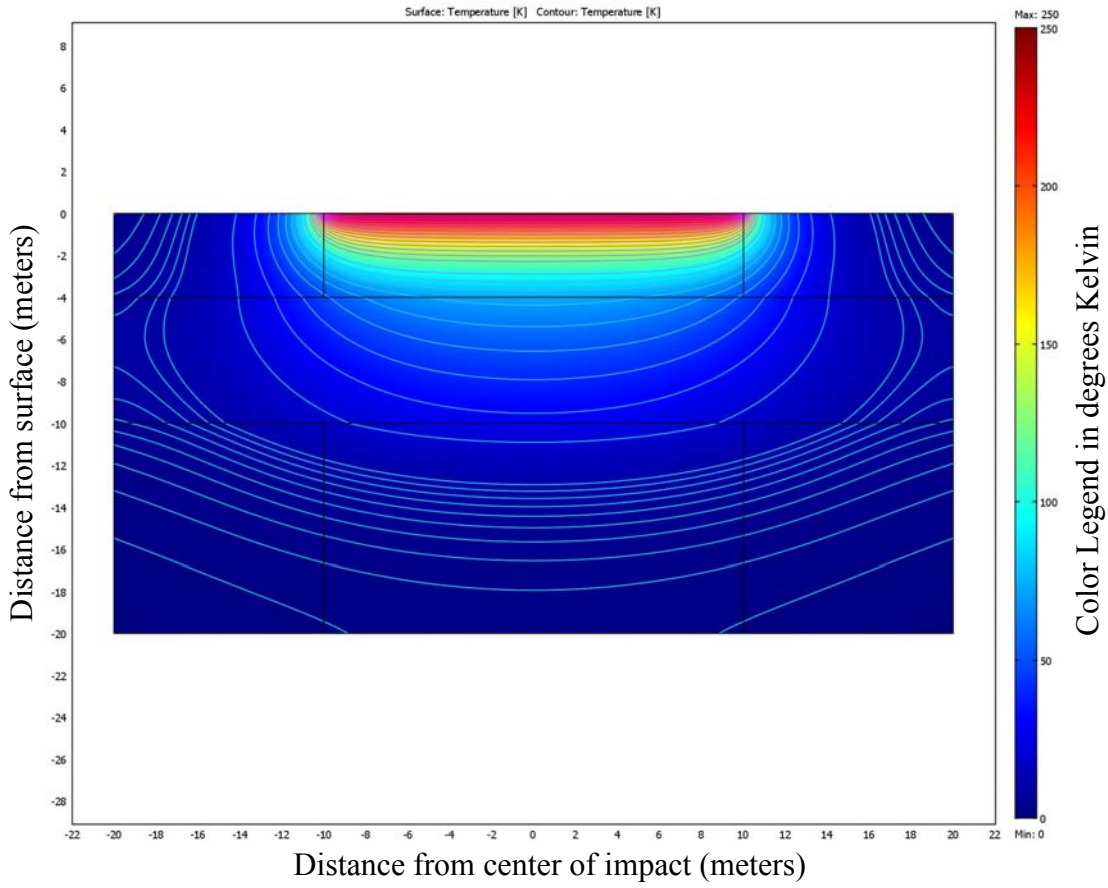

Figure 61: COMSOL generated image of a gypsum, permafrost, gypsum stratigraphic column. The permafrost layer is 6 meters thick at a depth of 4 meters. The vertical black lines can be ignored and in no way effect the resulting model. The horizontal black lines indicate the contact boundary between the basalt and permafrost layers.

Contour Intervals: 250, 240, 230, 220, 210, 200, 190, 180, 170, 160, 150, 140, 130, 120, 100, 90, 80, 70, 60, 50, 40, 30, 20, 10, 9, 8, 7, 6, 5, 4, 3, 2, 1

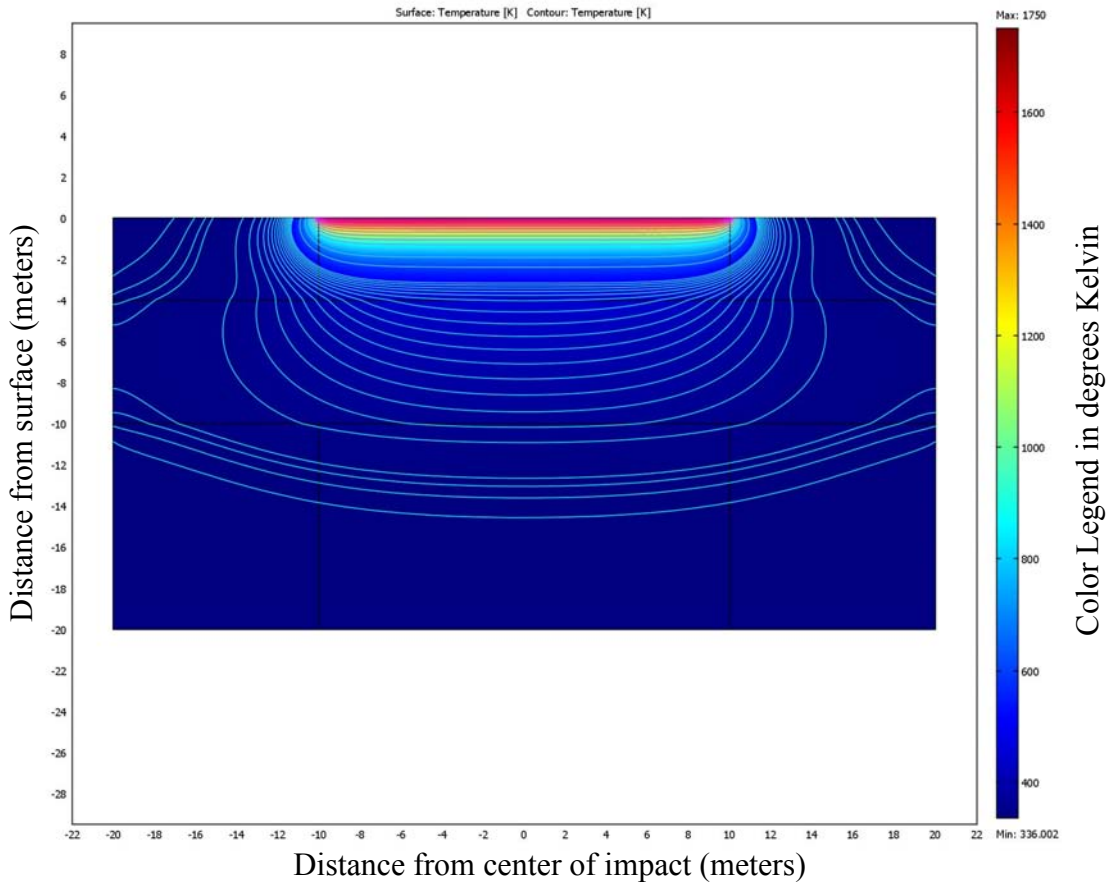

Figure 62: COMSOL generated image of a gypsum, permafrost, gypsum stratigraphic column. The permafrost layer is 6 meters thick at a depth of 4 meters. The vertical black lines can be ignored and in no way effect the resulting model. The horizontal black lines indicate the contact boundary between the basalt and permafrost layers.

Contour Intervals: 1700, 1600, 1500, 1400, 1300, 1200, 1100, 1000, 900, 800, 700, 600, 500, 490, 480, 470, 460, 450, 440, 430, 420, 410, 400, 390, 380, 370, 360, 350, 340, 339, 338, 337, 336

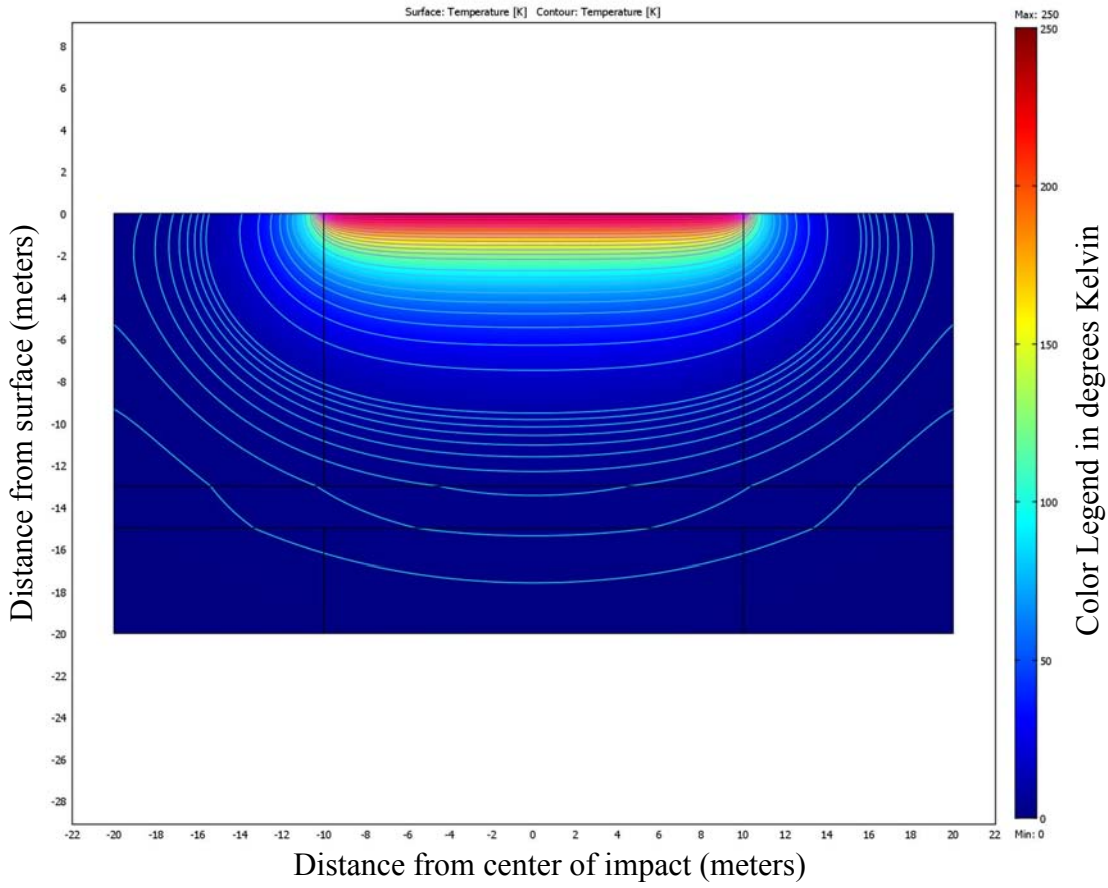

Figure 63: COMSOL generated image of a gypsum, permafrost, gypsum stratigraphic column. The permafrost layer is 2 meters thick at a depth of 13 meters. The vertical black lines can be ignored and in no way effect the resulting model. The horizontal black lines indicate the contact boundary between the basalt and permafrost layers.

Contour Intervals: 250, 240, 230, 220, 210, 200, 190, 180, 170, 160, 150, 140, 130, 120, 100, 90, 80, 70, 60, 50, 40, 30, 20, 10, 9, 8, 7, 6, 5, 4, 3, 2, 1

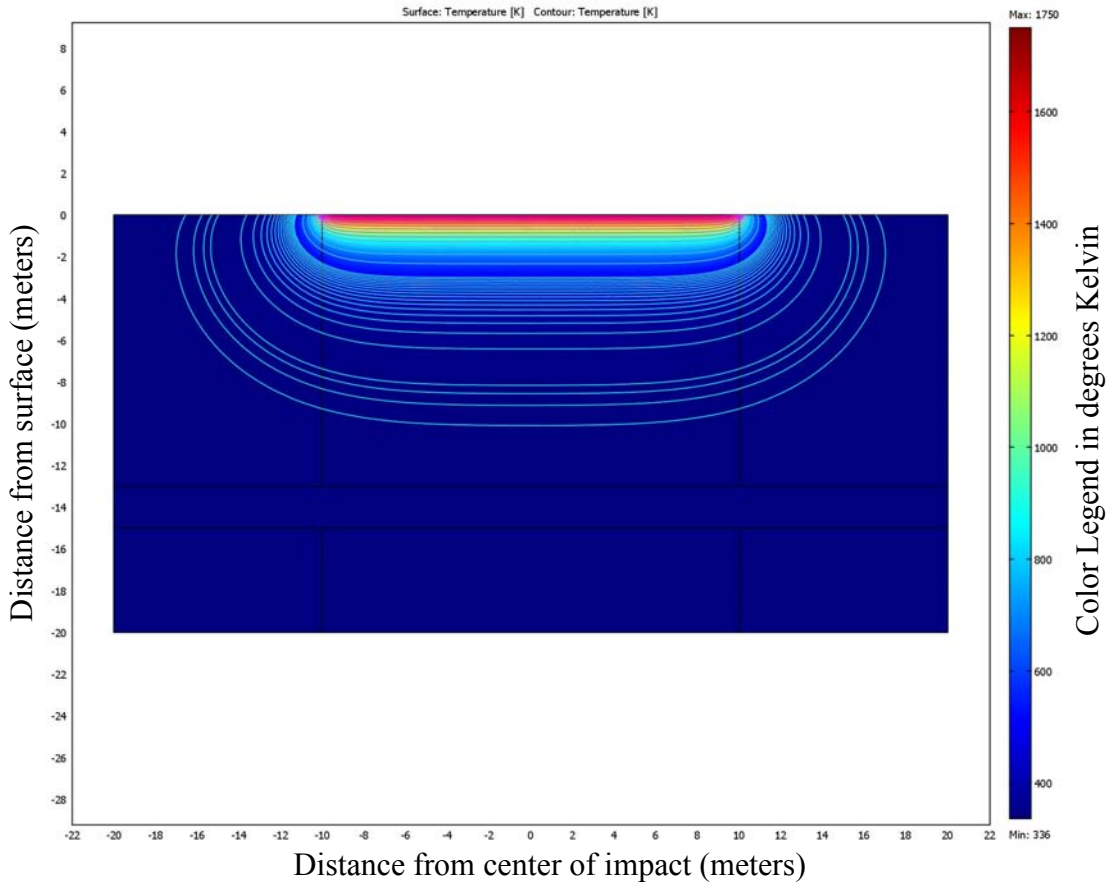

Figure 64: COMSOL generated image of a gypsum, permafrost, gypsum stratigraphic column. The permafrost layer is 2 meters thick at a depth of 13 meters. The vertical black lines can be ignored and in no way effect the resulting model. The horizontal black lines indicate the contact boundary between the basalt and permafrost layers.

Contour Intervals: 1700, 1600, 1500, 1400, 1300, 1200, 1100, 1000, 900, 800, 700, 600, 500, 490, 480, 470, 460, 450, 440, 430, 420, 410, 400, 390, 380, 370, 360, 350, 340, 339, 338, 337, 336

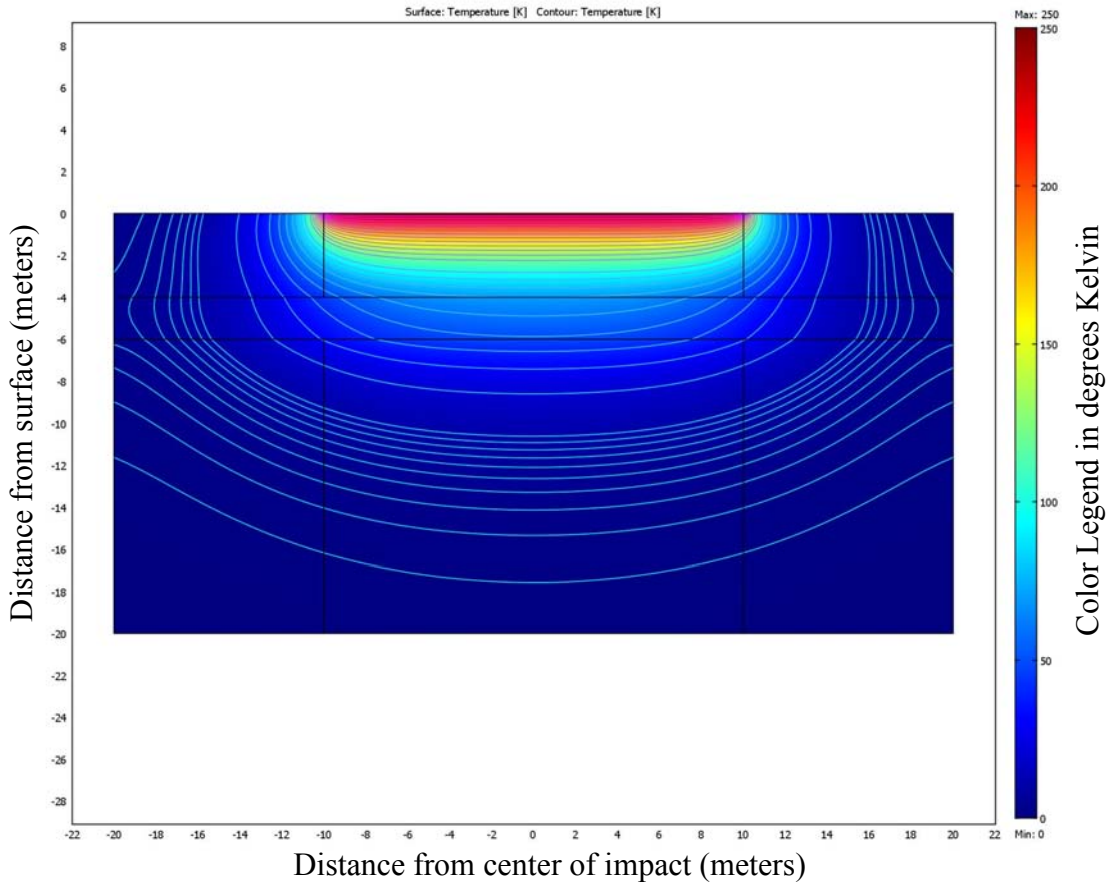

Figure 65: COMSOL generated image of a gypsum, permafrost, gypsum stratigraphic column. The permafrost layer is 2 meters thick at a depth of 4 meters. The vertical black lines can be ignored and in no way effect the resulting model. The horizontal black lines indicate the contact boundary between the basalt and permafrost layers.

Contour Intervals: 250, 240, 230, 220, 210, 200, 190, 180, 170, 160, 150, 140, 130, 120, 100, 90, 80, 70, 60, 50, 40, 30, 20, 10, 9, 8, 7, 6, 5, 4, 3, 2, 1

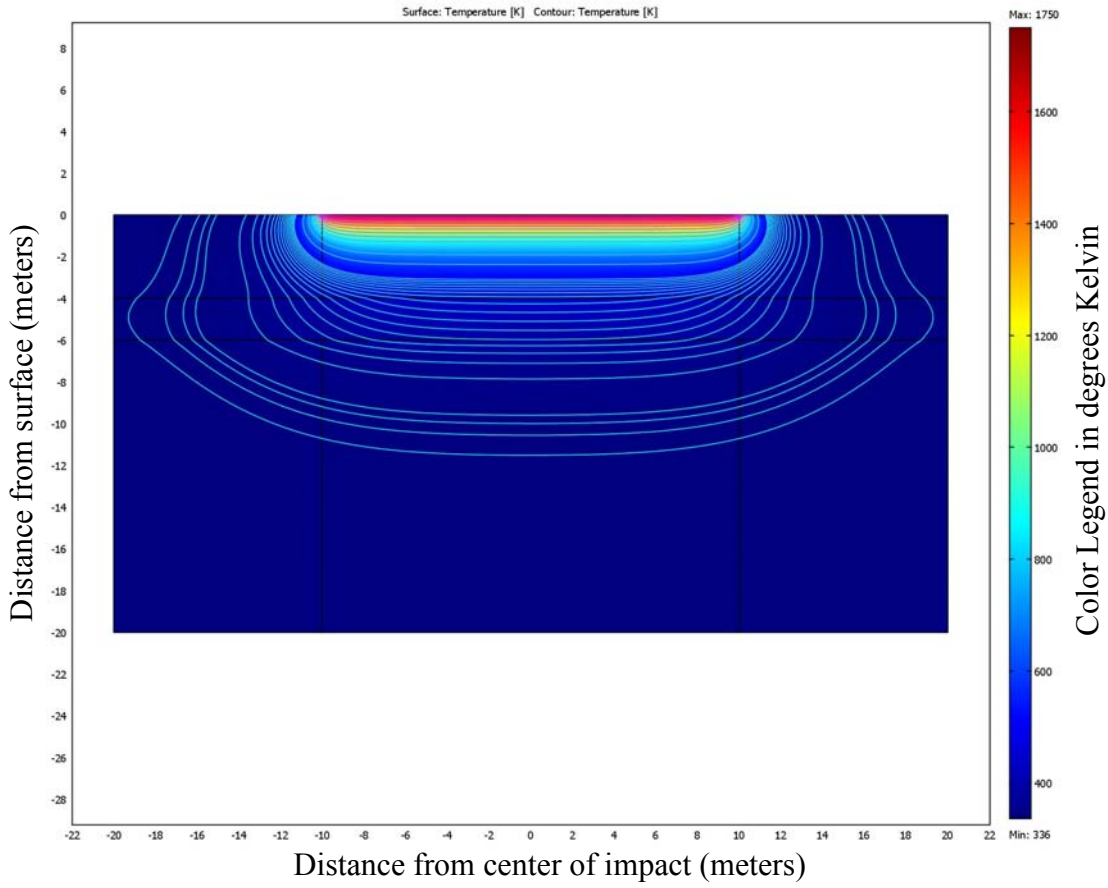

Figure 66: COMSOL generated image of a gypsum, permafrost, gypsum stratigraphic column. The permafrost layer is 2 meters thick at a depth of 4 meters. The vertical black lines can be ignored and in no way effect the resulting model. The horizontal black lines indicate the contact boundary between the basalt and permafrost layers.

Contour Intervals: 1700, 1600, 1500, 1400, 1300, 1200, 1100, 1000, 900, 800, 700, 600, 500, 490, 480, 470, 460, 450, 440, 430, 420, 410, 400, 390, 380, 370, 360, 350, 340, 339, 338, 337, 336

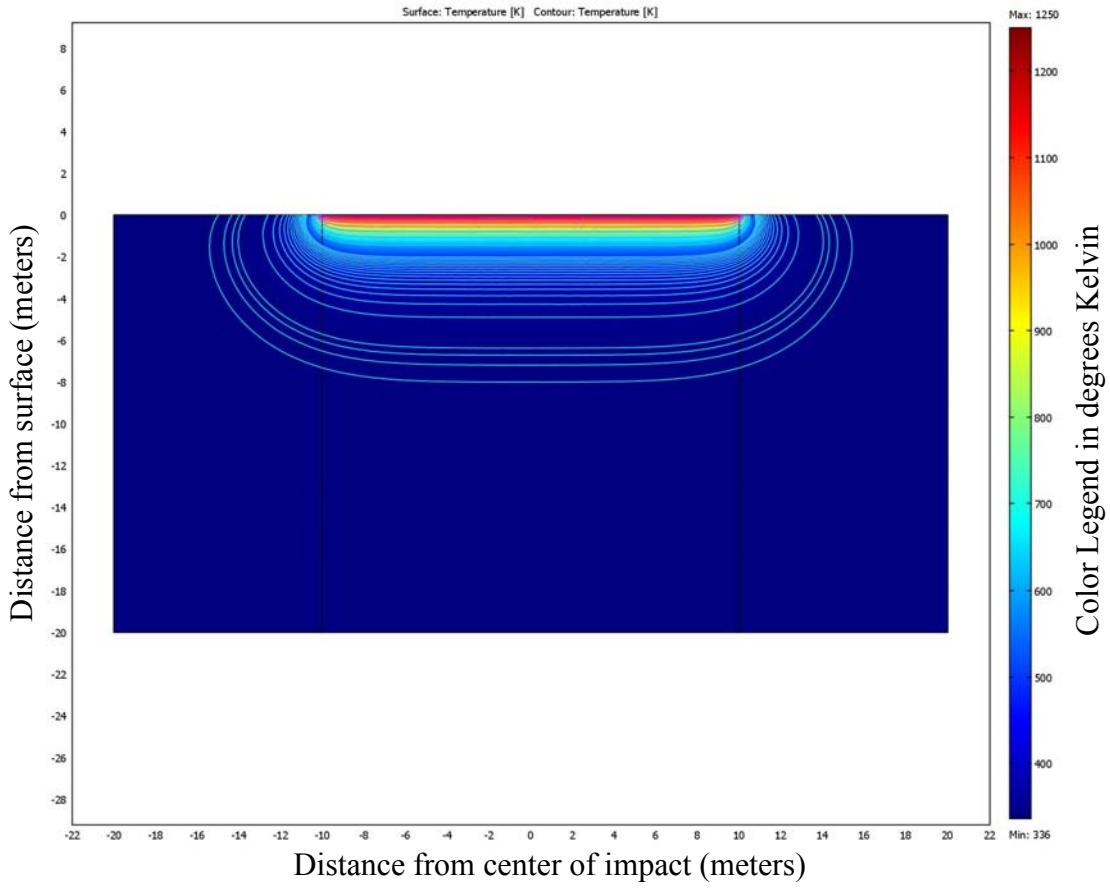

Figure 67: COMSOL generated image of a homogeneous halite stratigraphic column. The halite layer is 20 meters thick. The vertical black lines can be ignored and in no way effect the resulting model.

Contour Intervals: 1200, 1100, 1000, 900, 800, 700, 600, 500, 490, 480, 470, 460, 450, 440, 430, 420, 410, 400, 390, 380, 370, 360, 350, 340, 339, 338, 337, 336

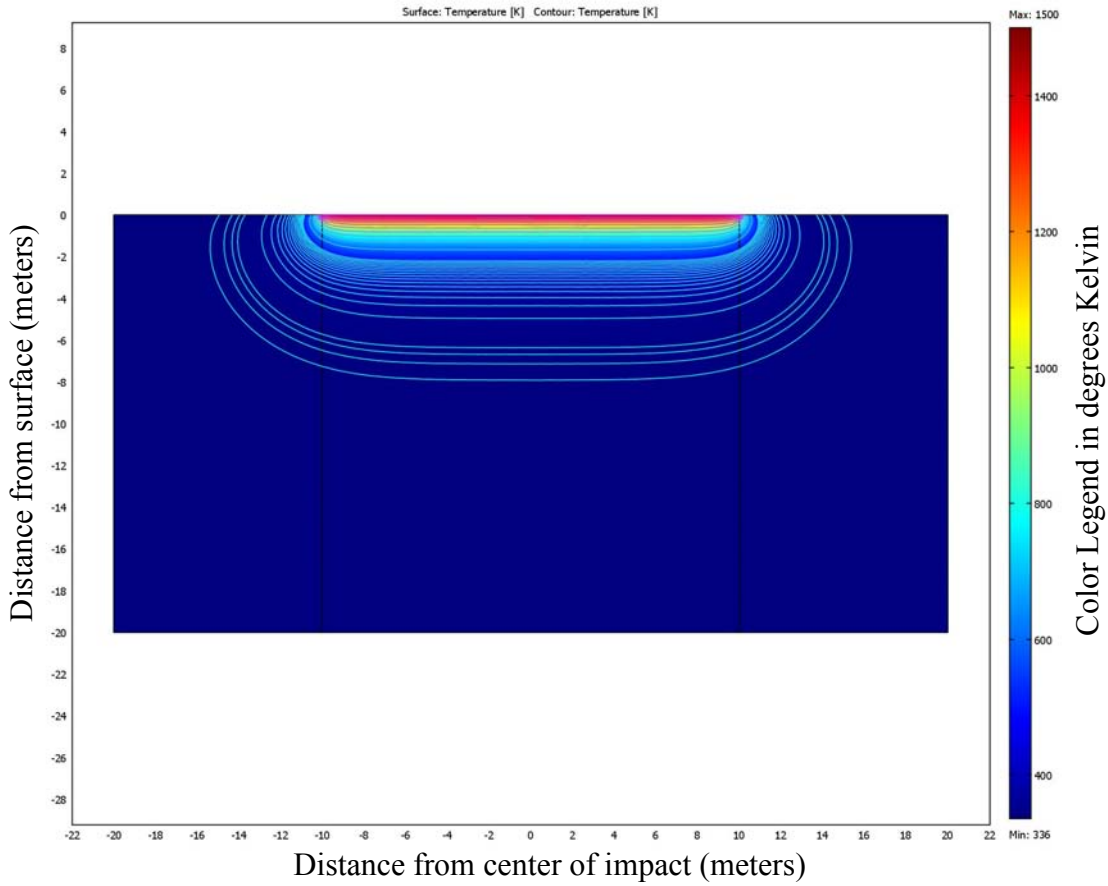

Figure 68: COMSOL generated image of a homogeneous halite stratigraphic column. The halite layer is 20 meters thick. The vertical black lines can be ignored and in no way effect the resulting model.

Contour Intervals: 1700, 1600, 1500, 1400, 1300, 1200, 1100, 1000, 900, 800, 700, 600, 500, 490, 480, 470, 460, 450, 440, 430, 420, 410, 400, 390, 380, 370, 360, 350, 340, 339, 338, 337, 336

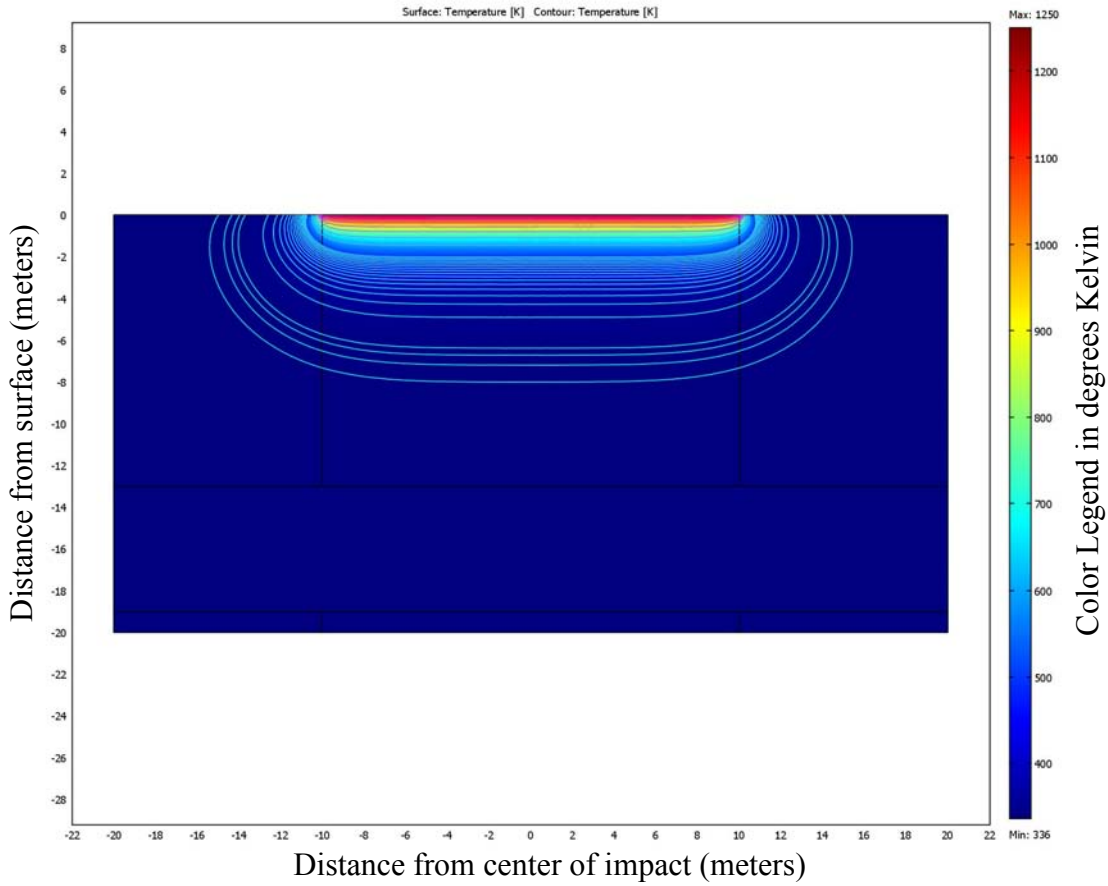

Figure 69: COMSOL generated image of a halite, permafrost, halite stratigraphic column. The permafrost layer is 6 meters thick at a depth of 13 meters. The vertical black lines can be ignored and in no way effect the resulting model. The horizontal black lines indicate the contact boundary between the basalt and permafrost layers.

Contour Intervals: 1200, 1100, 1000, 900, 800, 700, 600, 500, 490, 480, 470, 460, 450, 440, 430, 420, 410, 400, 390, 380, 370, 360, 350, 340, 339, 338, 337, 336

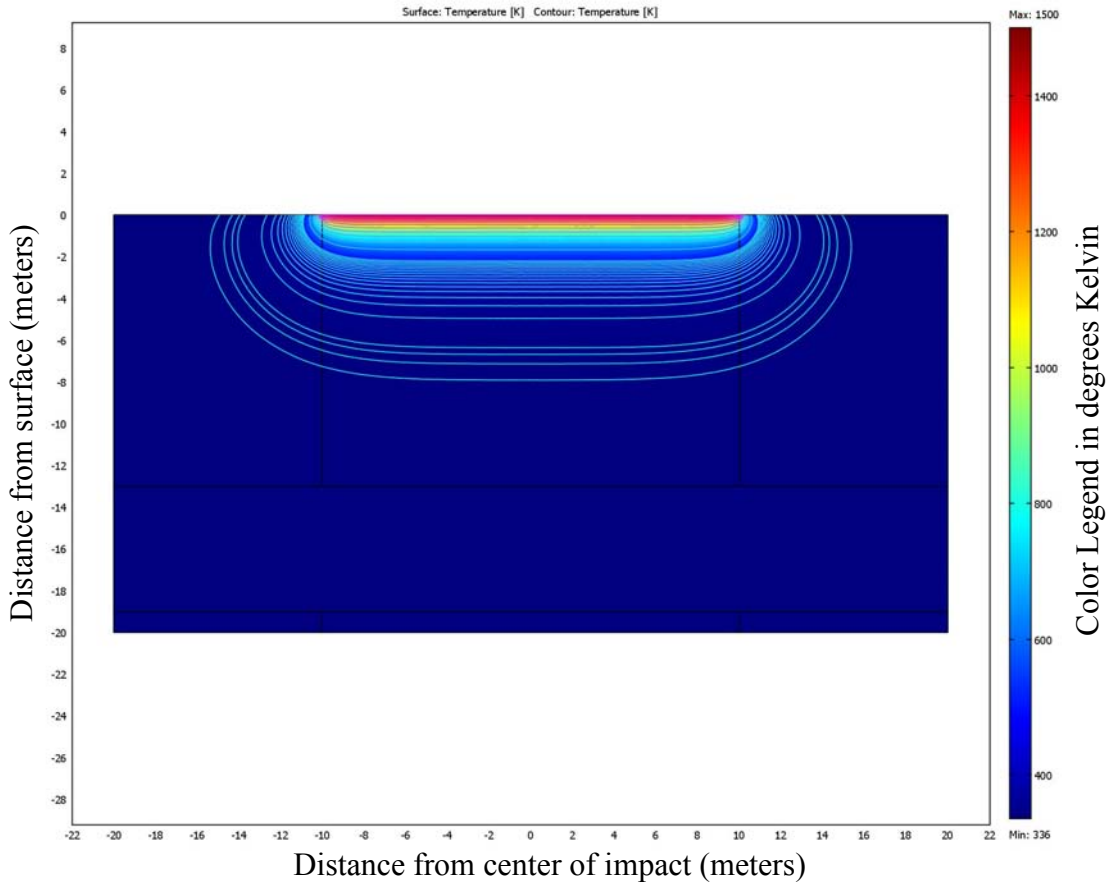

Figure 70: COMSOL generated image of a halite, permafrost, halite stratigraphic column. The permafrost layer is 6 meters thick at a depth of 13 meters. The vertical black lines can be ignored and in no way effect the resulting model. The horizontal black lines indicate the contact boundary between the basalt and permafrost layers.

Contour Intervals: 1500, 1400, 1300, 1200, 1100, 1000, 900, 800, 700, 600, 500, 490, 480, 470, 460, 450, 440, 430, 420, 410, 400, 390, 380, 370, 360, 350, 340, 339, 338, 337, 336

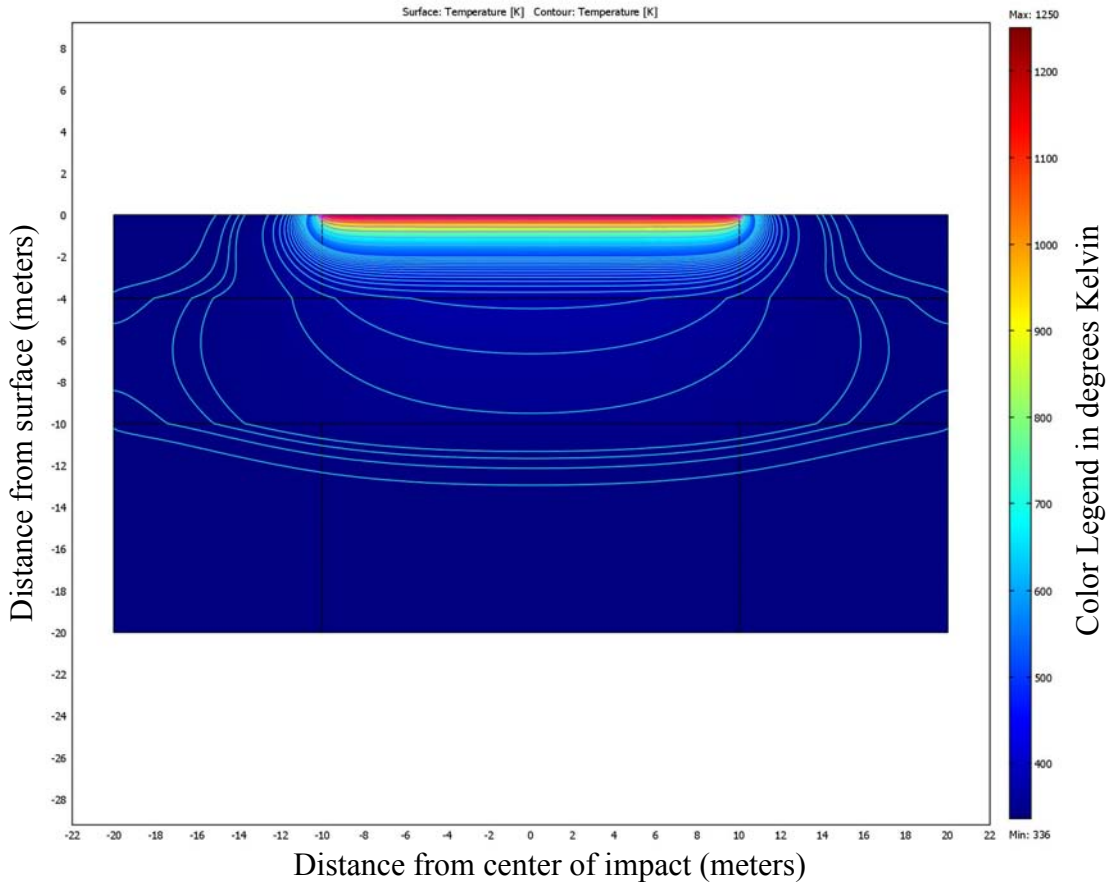

Figure 71: COMSOL generated image of a halite, permafrost, halite stratigraphic column. The permafrost layer is 6 meters thick at a depth of 4 meters. The vertical black lines can be ignored and in no way effect the resulting model. The horizontal black lines indicate the contact boundary between the basalt and permafrost layers.

Contour Intervals: 1200, 1100, 1000, 900, 800, 700, 600, 500, 490, 480, 470, 460, 450, 440, 430, 420, 410, 400, 390, 380, 370, 360, 350, 340, 339, 338, 337, 336

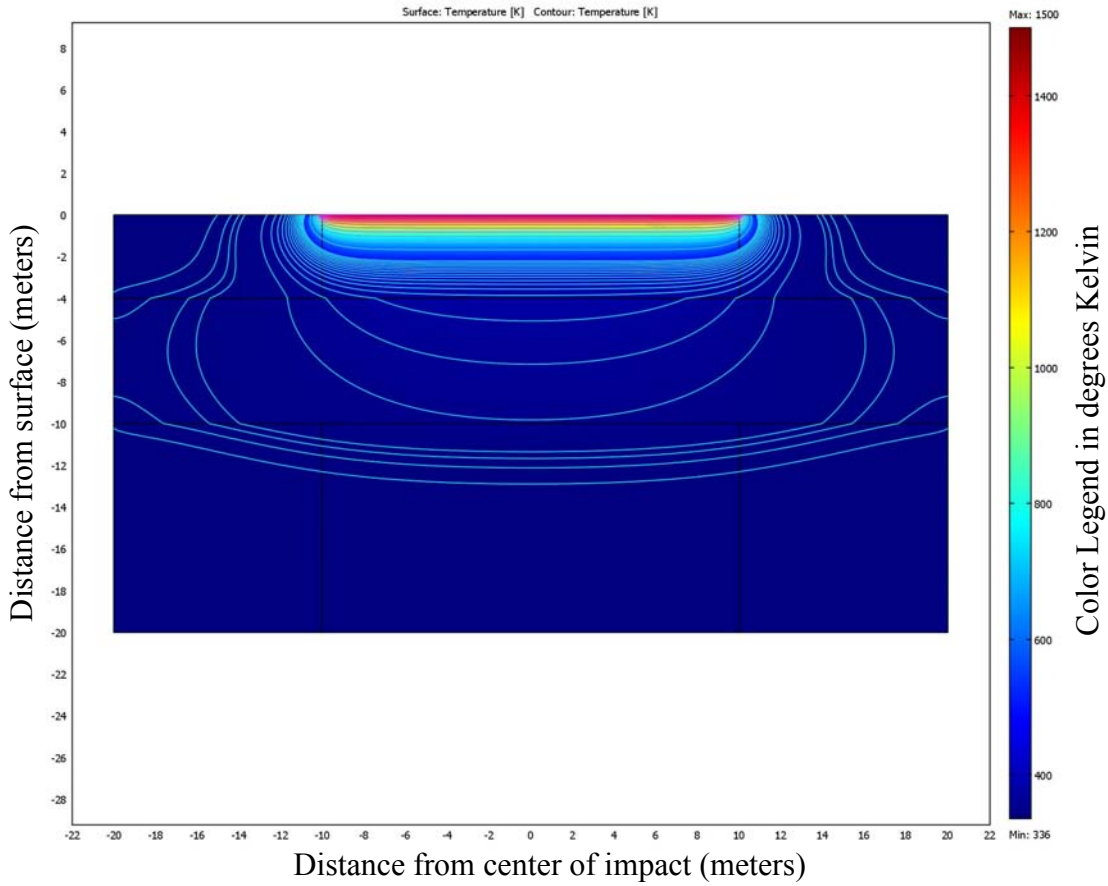

Figure 72: COMSOL generated image of a halite, permafrost, halite stratigraphic column. The permafrost layer is 6 meters thick at a depth of 4 meters. The vertical black lines can be ignored and in no way effect the resulting model. The horizontal black lines indicate the contact boundary between the basalt and permafrost layers.

Contour Intervals: 1500, 1400, 1300, 1200, 1100, 1000, 900, 800, 700, 600, 500, 490, 480, 470, 460, 450, 440, 430, 420, 410, 400, 390, 380, 370, 360, 350, 340, 339, 338, 337, 336

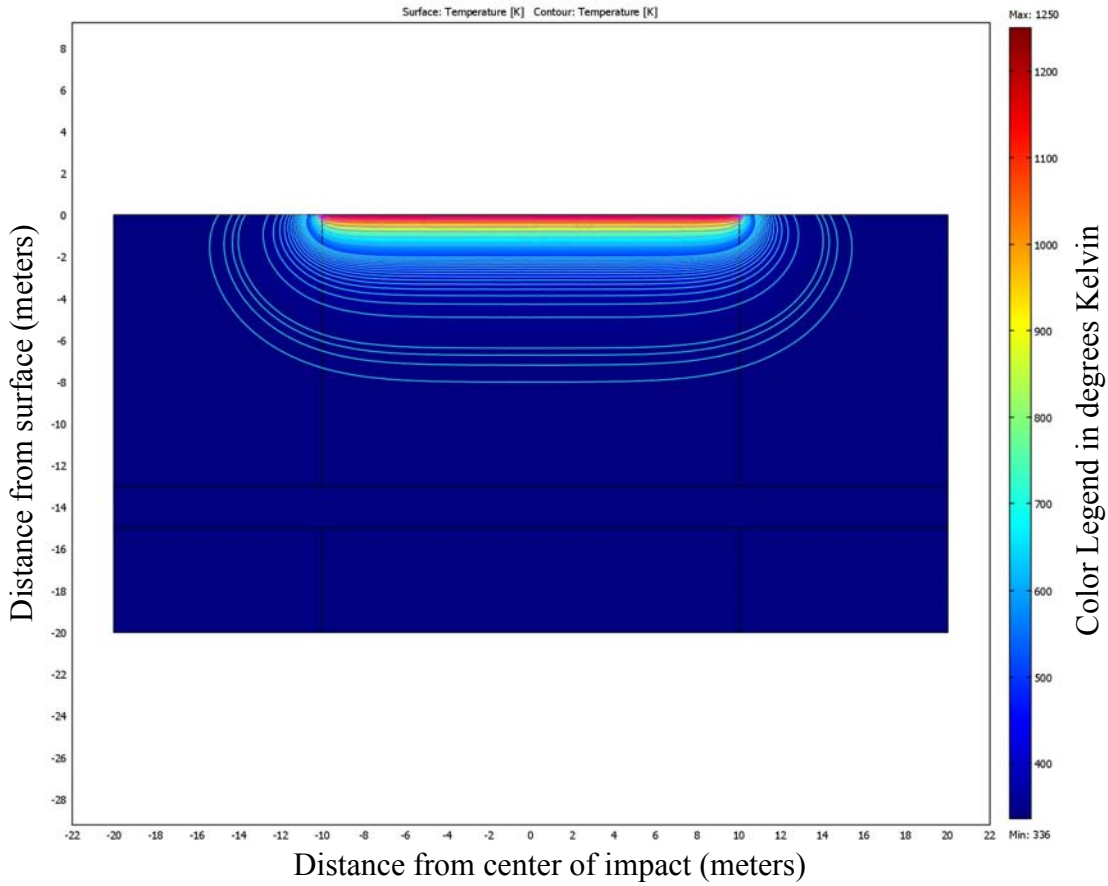

Figure 73: COMSOL generated image of a halite, permafrost, halite stratigraphic column. The permafrost layer is 2 meters thick at a depth of 13 meters. The vertical black lines can be ignored and in no way effect the resulting model. The horizontal black lines indicate the contact boundary between the basalt and permafrost layers.

Contour Intervals: 1200, 1100, 1000, 900, 800, 700, 600, 500, 490, 480, 470, 460, 450, 440, 430, 420, 410, 400, 390, 380, 370, 360, 350, 340, 339, 338, 337, 336

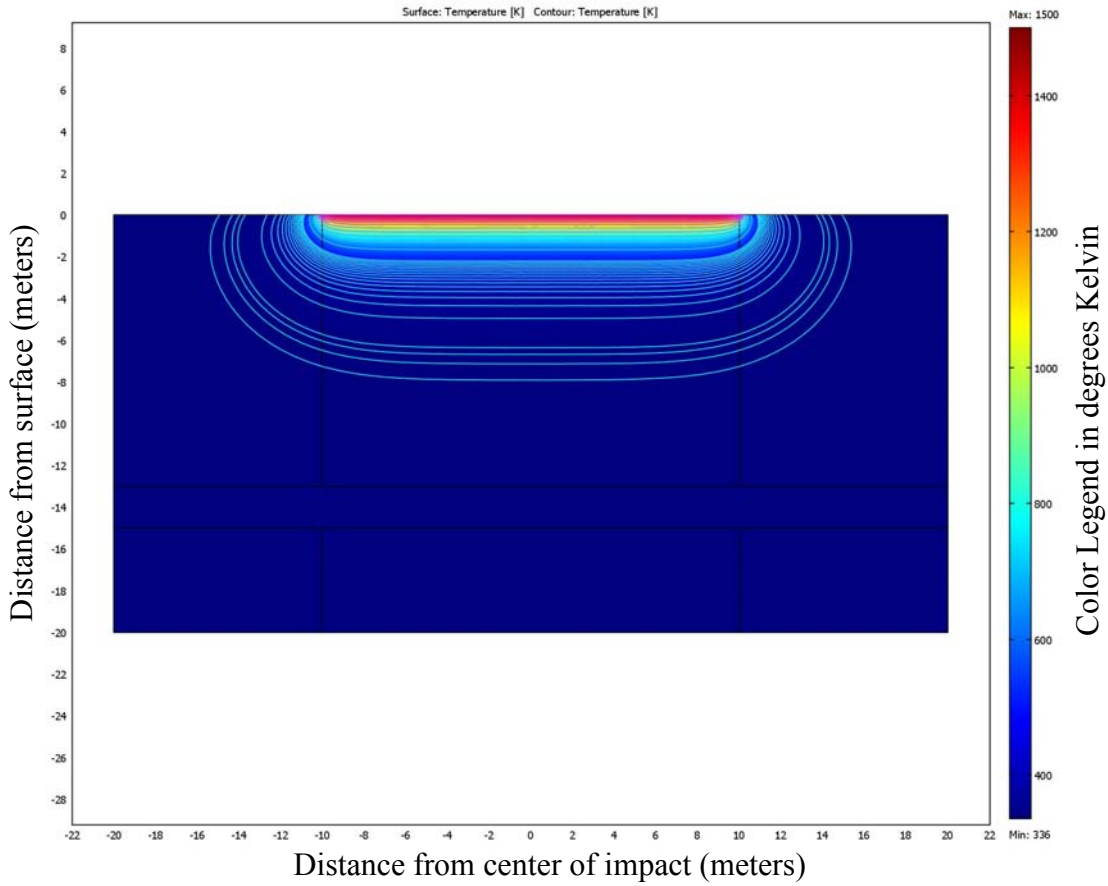

Figure 74: COMSOL generated image of a halite, permafrost, halite stratigraphic column. The permafrost layer is 2 meters thick at a depth of 13 meters. The vertical black lines can be ignored and in no way effect the resulting model. The horizontal black lines indicate the contact boundary between the basalt and permafrost layers.

Contour Intervals: 1500, 1400, 1300, 1200, 1100, 1000, 900, 800, 700, 600, 500, 490, 480, 470, 460, 450, 440, 430, 420, 410, 400, 390, 380, 370, 360, 350, 340, 339, 338, 337, 336

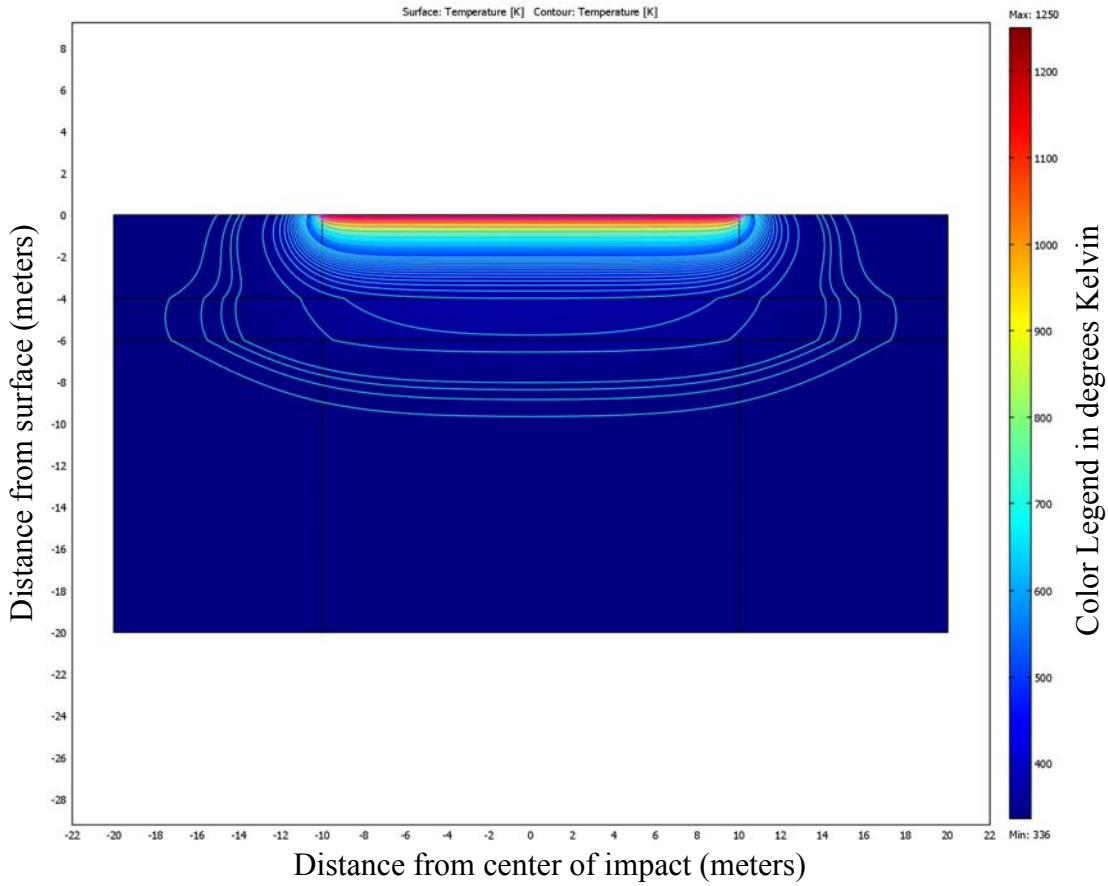

Figure 75: COMSOL generated image of a halite, permafrost, halite stratigraphic column. The permafrost layer is 2 meters thick at a depth of 4 meters. The vertical black lines can be ignored and in no way effect the resulting model. The horizontal black lines indicate the contact boundary between the basalt and permafrost layers.

Contour Intervals: 1200, 1100, 1000, 900, 800, 700, 600, 500, 490, 480, 470, 460, 450, 440, 430, 420, 410, 400, 390, 380, 370, 360, 350, 340, 339, 338, 337, 336

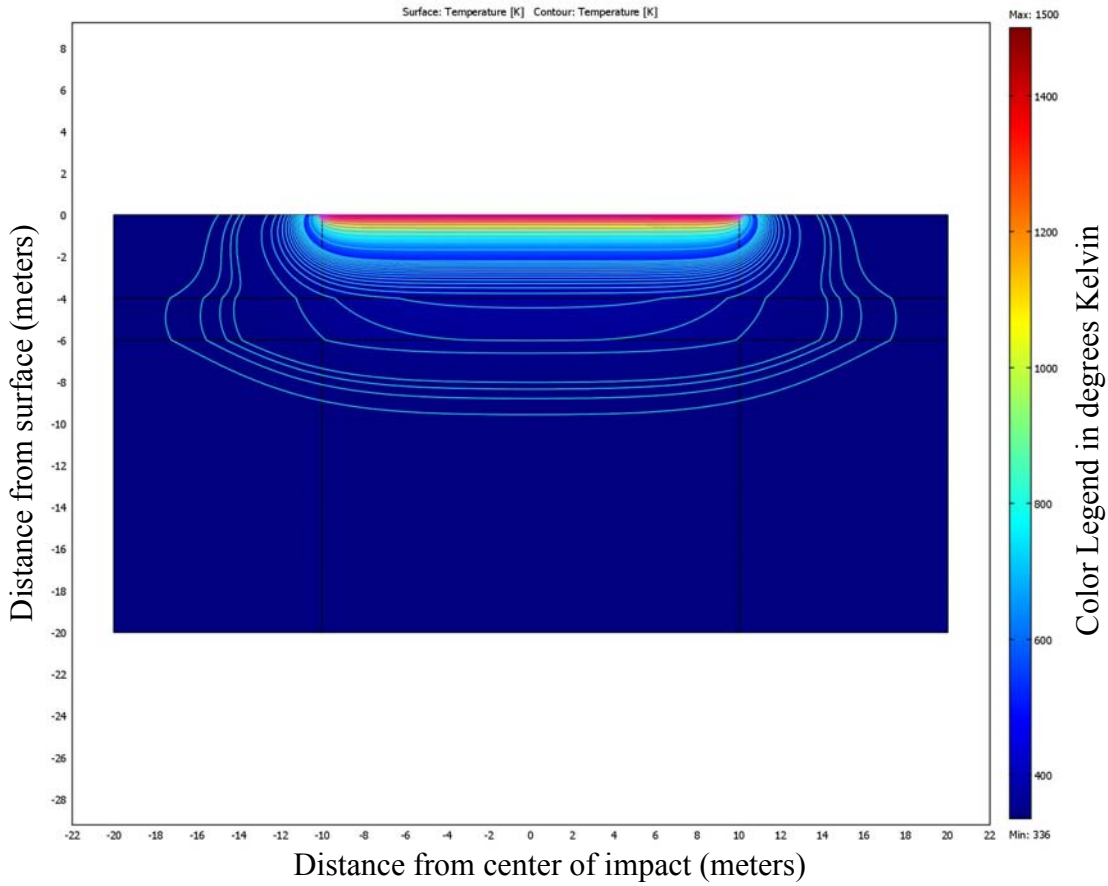

Figure 76: COMSOL generated image of a halite, permafrost, halite stratigraphic column. The permafrost layer is 2 meters thick at a depth of 4 meters. The vertical black lines can be ignored and in no way effect the resulting model. The horizontal black lines indicate the contact boundary between the basalt and permafrost layers.

Contour Intervals: 1500, 1400, 1300, 1200, 1100, 1000, 900, 800, 700, 600, 500, 490, 480, 470, 460, 450, 440, 430, 420, 410, 400, 390, 380, 370, 360, 350, 340, 339, 338, 337, 336

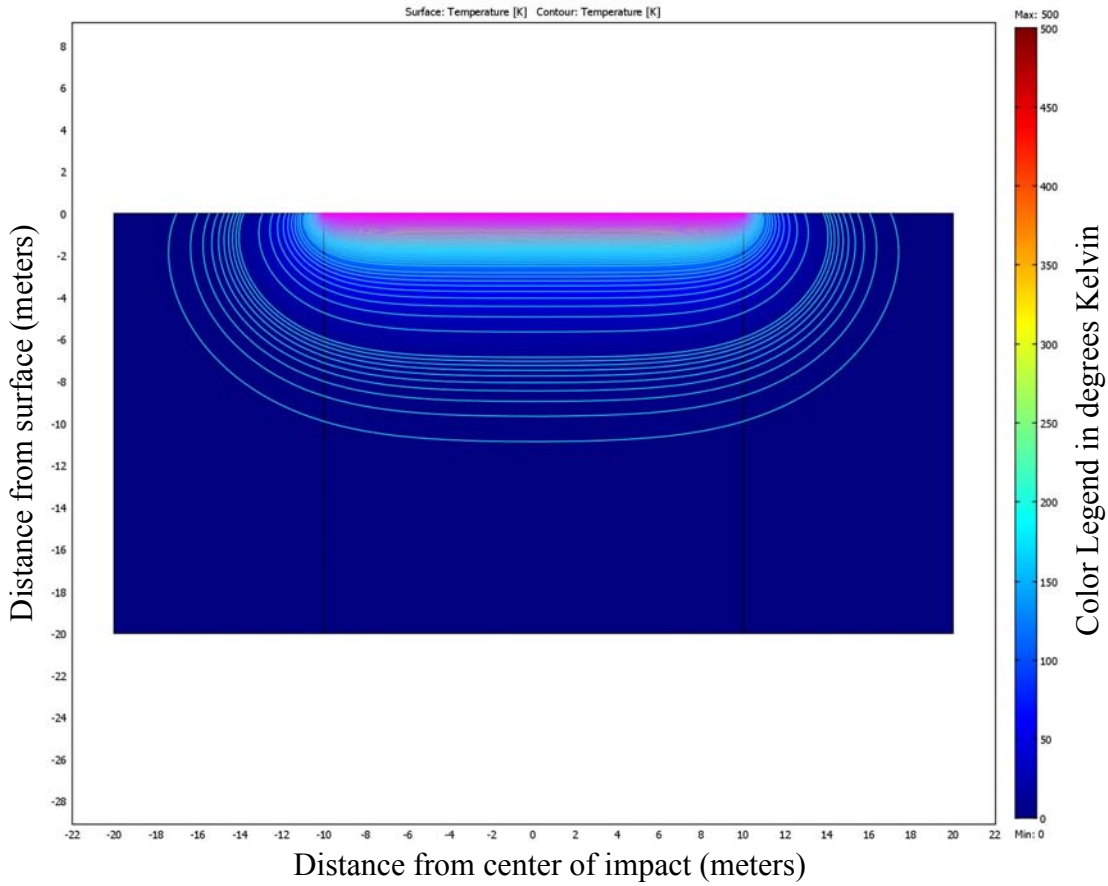

Figure 77: COMSOL generated image of a homogeneous limestone stratigraphic column. The limestone layer is 20 meters thick. The vertical black lines can be ignored and in no way effect the resulting model.

Contour Intervals: 500, 490, 480, 470, 460, 450, 440, 430, 420, 410, 400, 390, 380, 370, 360, 350, 340, 330, 320, 310, 300, 290, 280, 270, 260, 250, 240, 230, 220, 210, 200, 190, 180, 170, 160, 150, 140, 130, 120, 100, 90, 80, 70, 60, 50, 40, 30, 20, 10, 9, 8, 7, 6, 5, 4, 3, 2, 1

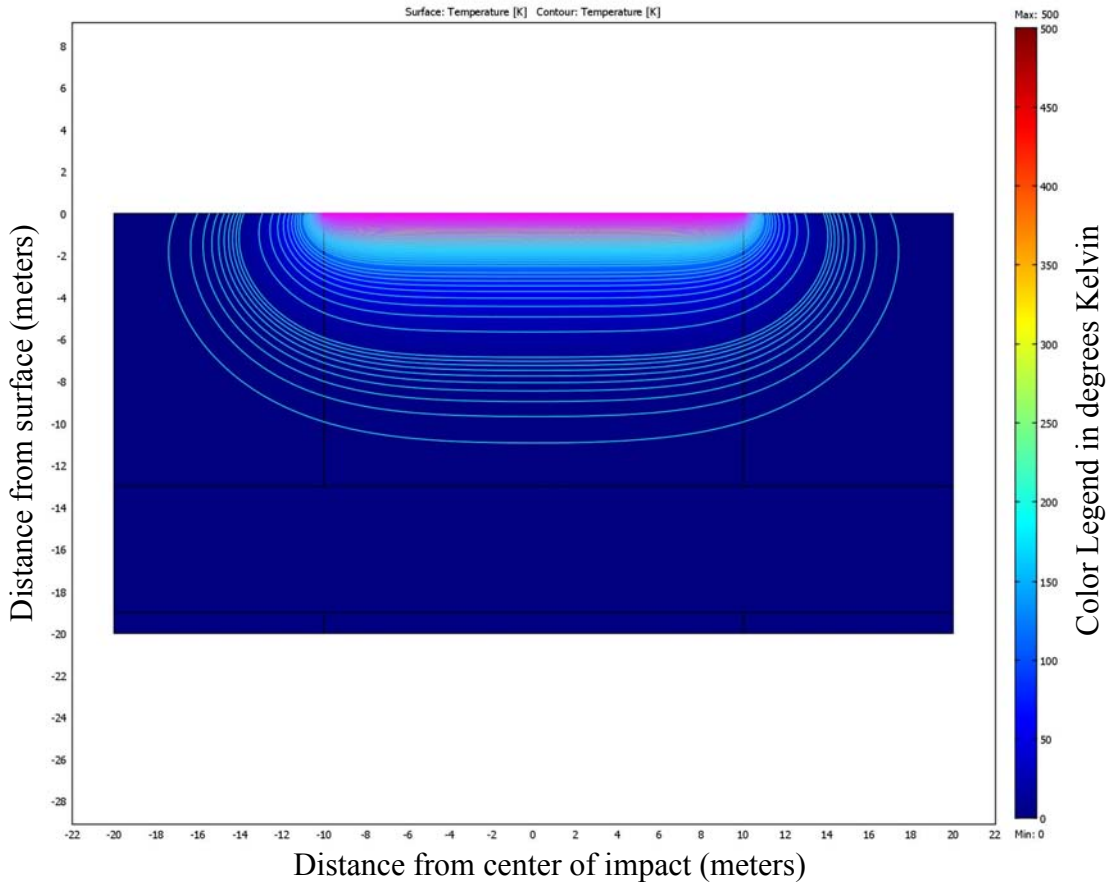

Figure 78: COMSOL generated image of a limestone, permafrost, limestone stratigraphic column. The permafrost layer is 6 meters thick at a depth of 13 meters. The vertical black lines can be ignored and in no way effect the resulting model. The horizontal black lines indicate the contact boundary between the basalt and permafrost layers.

Contour Intervals: 500, 490, 480, 470, 460, 450, 440, 430, 420, 410, 400, 390, 380, 370, 360, 350, 340, 330, 320, 310, 300, 290, 280, 270, 260, 250, 240, 230, 220, 210, 200, 190, 180, 170, 160, 150, 140, 130, 120, 100, 90, 80, 70, 60, 50, 40, 30, 20, 10, 9, 8, 7, 6, 5, 4, 3, 2, 1

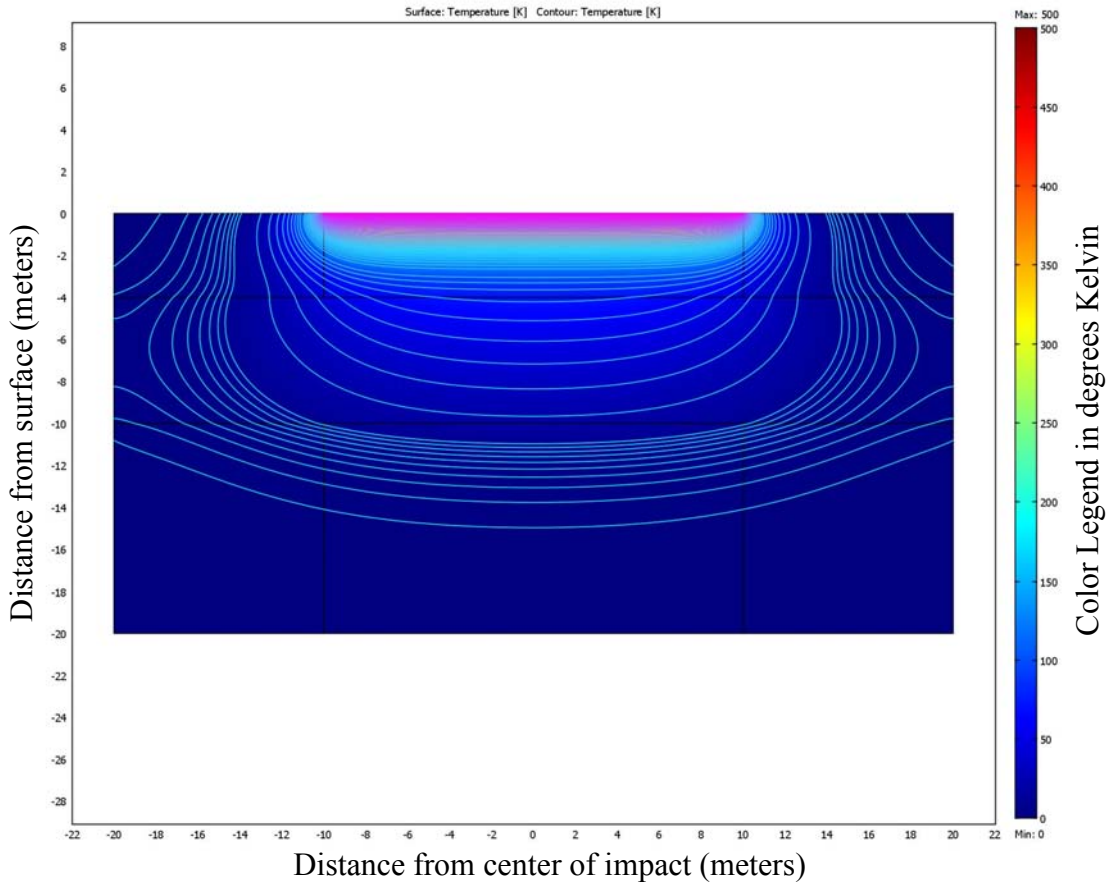

Figure 79: COMSOL generated image of a limestone, permafrost, limestone stratigraphic column. The permafrost layer is 6 meters thick at a depth of 4 meters. The vertical black lines can be ignored and in no way effect the resulting model. The horizontal black lines indicate the contact boundary between the basalt and permafrost layers.

Contour Intervals: 500, 490, 480, 470, 460, 450, 440, 430, 420, 410, 400, 390, 380, 370, 360, 350, 340, 330, 320, 310, 300, 290, 280, 270, 260, 250, 240, 230, 220, 210, 200, 190, 180, 170, 160, 150, 140, 130, 120, 100, 90, 80, 70, 60, 50, 40, 30, 20, 10, 9, 8, 7, 6, 5, 4, 3, 2, 1

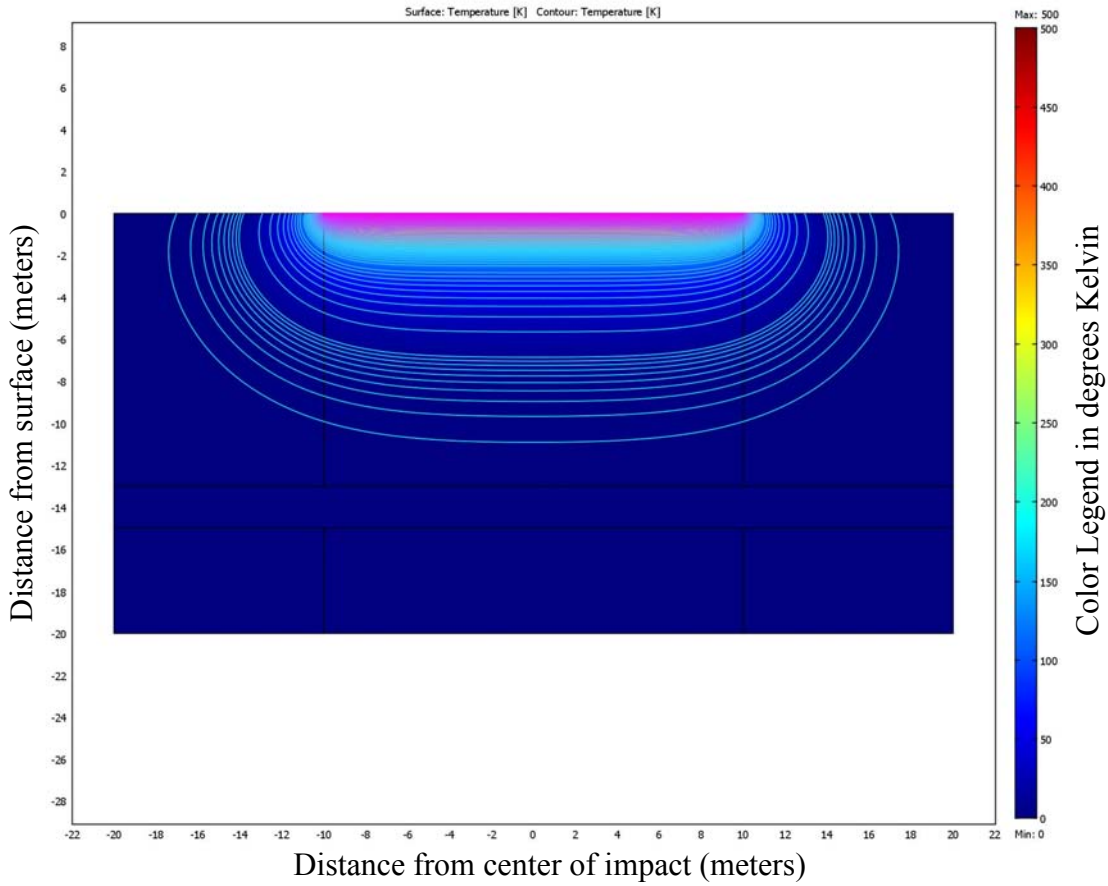

Figure 80: COMSOL generated image of a limestone, permafrost, limestone stratigraphic column. The permafrost layer is 2 meters thick at a depth of 13 meters. The vertical black lines can be ignored and in no way effect the resulting model. The horizontal black lines indicate the contact boundary between the basalt and permafrost layers.

Contour Intervals: 500, 490, 480, 470, 460, 450, 440, 430, 420, 410, 400, 390, 380, 370, 360, 350, 340, 330, 320, 310, 300, 290, 280, 270, 260, 250, 240, 230, 220, 210, 200, 190, 180, 170, 160, 150, 140, 130, 120, 100, 90, 80, 70, 60, 50, 40, 30, 20, 10, 9, 8, 7, 6, 5, 4, 3, 2, 1

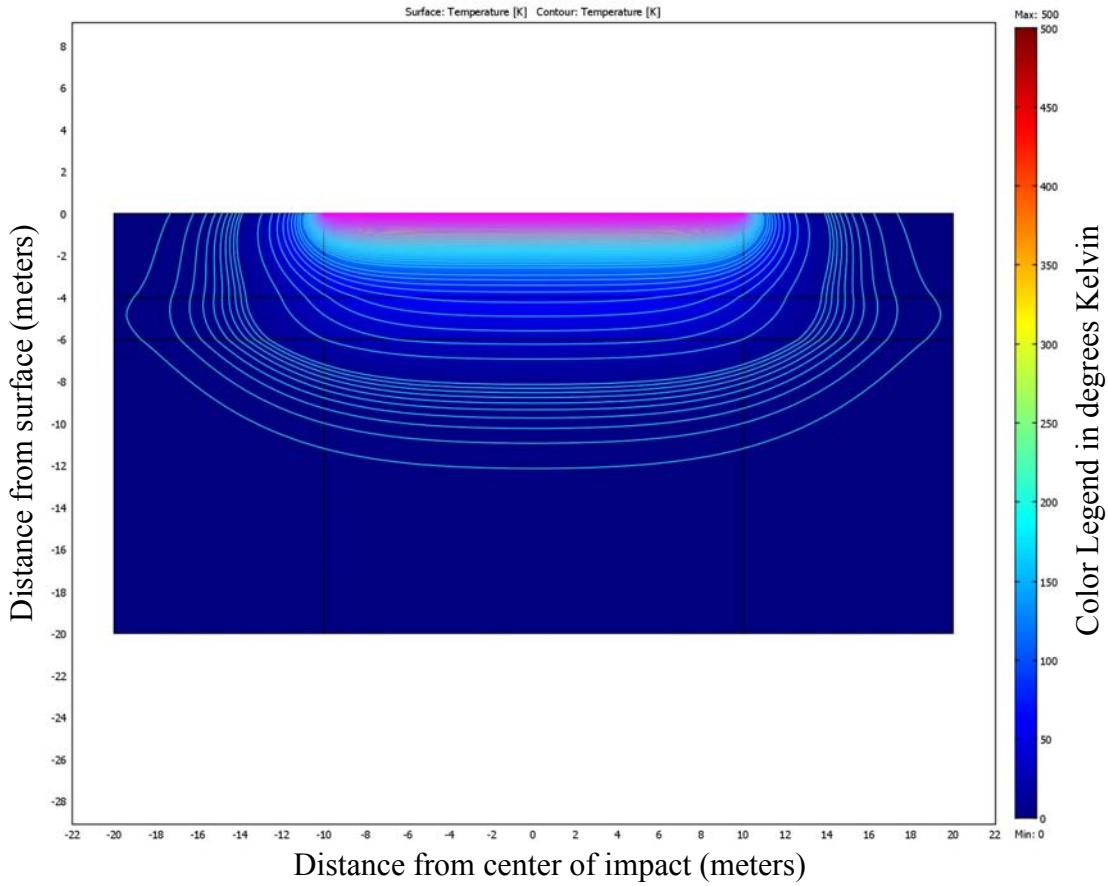

Figure 81: COMSOL generated image of a limestone, permafrost, limestone stratigraphic column. The permafrost layer is 2 meters thick at a depth of 4 meters. The vertical black lines can be ignored and in no way effect the resulting model. The horizontal black lines indicate the contact boundary between the basalt and permafrost layers.

Contour Intervals: 500, 490, 480, 470, 460, 450, 440, 430, 420, 410, 400, 390, 380, 370, 360, 350, 340, 330, 320, 310, 300, 290, 280, 270, 260, 250, 240, 230, 220, 210, 200, 190, 180, 170, 160, 150, 140, 130, 120, 100, 90, 80, 70, 60, 50, 40, 30, 20, 10, 9, 8, 7, 6, 5, 4, 3, 2, 1

Ejecta Blanket Modeling Results

COMSOL models were produced to determine the depth to which the heat from an ejecta blanket would propagate. One uniform ejecta blanket thickness was used in coordination with one temperature, 1250 degrees Kelvin. A uniform ejecta blanket thickness was used so the model results could be applied to a wide variety of impact crater diameters. The assumption was made that the material ejected from the impact event would be the same composition as the material that it would cover. In the following model figures the heated ejecta blanket is sandwiched between a cooler layer of deposited material above with a bedrock layer below. This set up provides a visual representation of the heat loss to the surrounding cooler layers (both above and below). In each model there exist temperature contour lines (shown as horizontal lines). Contour line values are the same for each figure for ease of comparison.

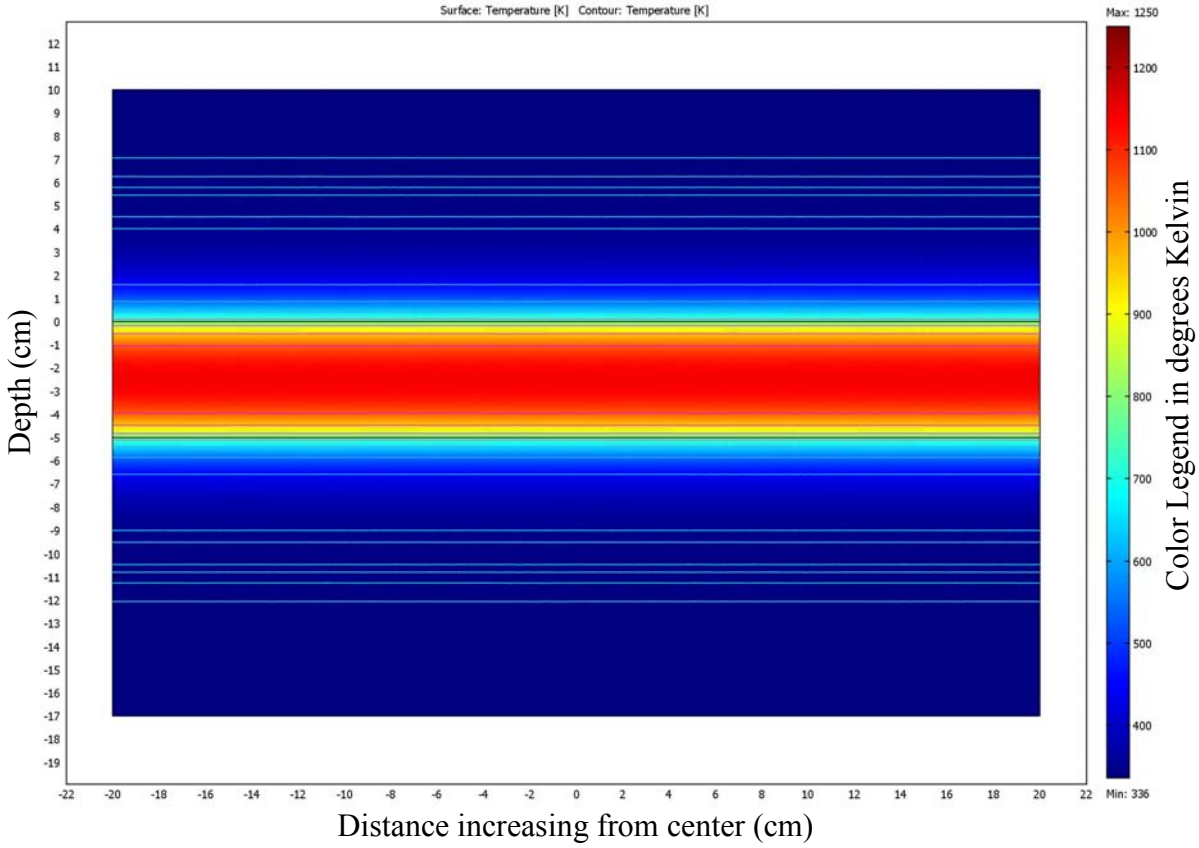

Figure 82: COMSOL generated image of a basalt ejecta blanket. The stratigraphic column is basalt ejecta blanket, heated basalt ejecta blanket, basalt bedrock. The horizontal black lines indicate the contact boundary between the (top to bottom) cool ejecta blanket, heated ejecta blanket, and bedrock. This figure illustrates the propagation of heat through the bedrock as well as the overlying ejecta blanket that has been deposited cold rather than heated.

Contour Intervals: 1150, 1050, 950, 850, 750, 650, 550, 450, 350, 345, 340, 339, 338, 337

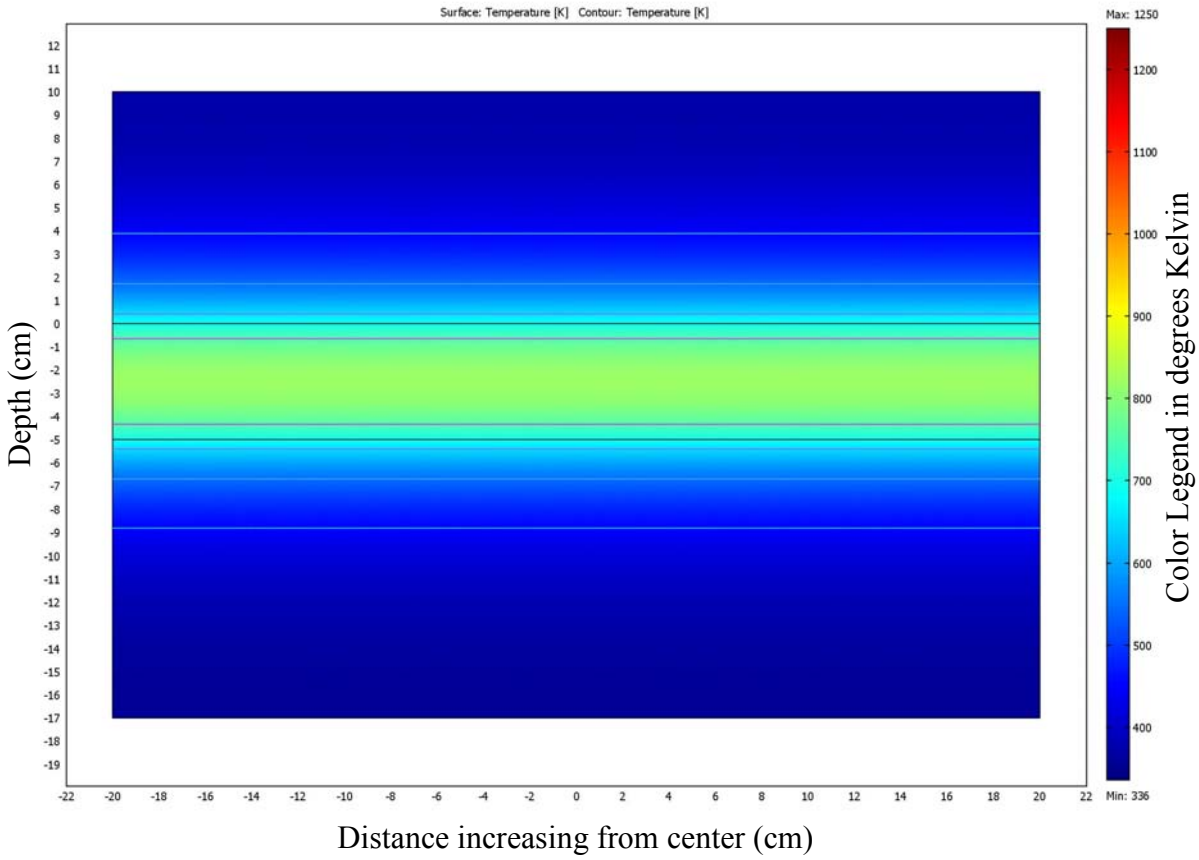

Figure 83: COMSOL generated image of an epsomite ejecta blanket. The stratigraphic column is epsomite ejecta blanket, heated epsomite ejecta blanket, epsomite bedrock. The horizontal black lines indicate the contact boundary between the (top to bottom) cool ejecta blanket, heated ejecta blanket, and bedrock. This figure illustrates the propagation of heat through the bedrock as well as the overlying ejecta blanket that has been deposited cold rather than heated.

Contour Intervals: 1150, 1050, 950, 850, 750, 650, 550, 450, 350, 345, 340, 339, 338, 337

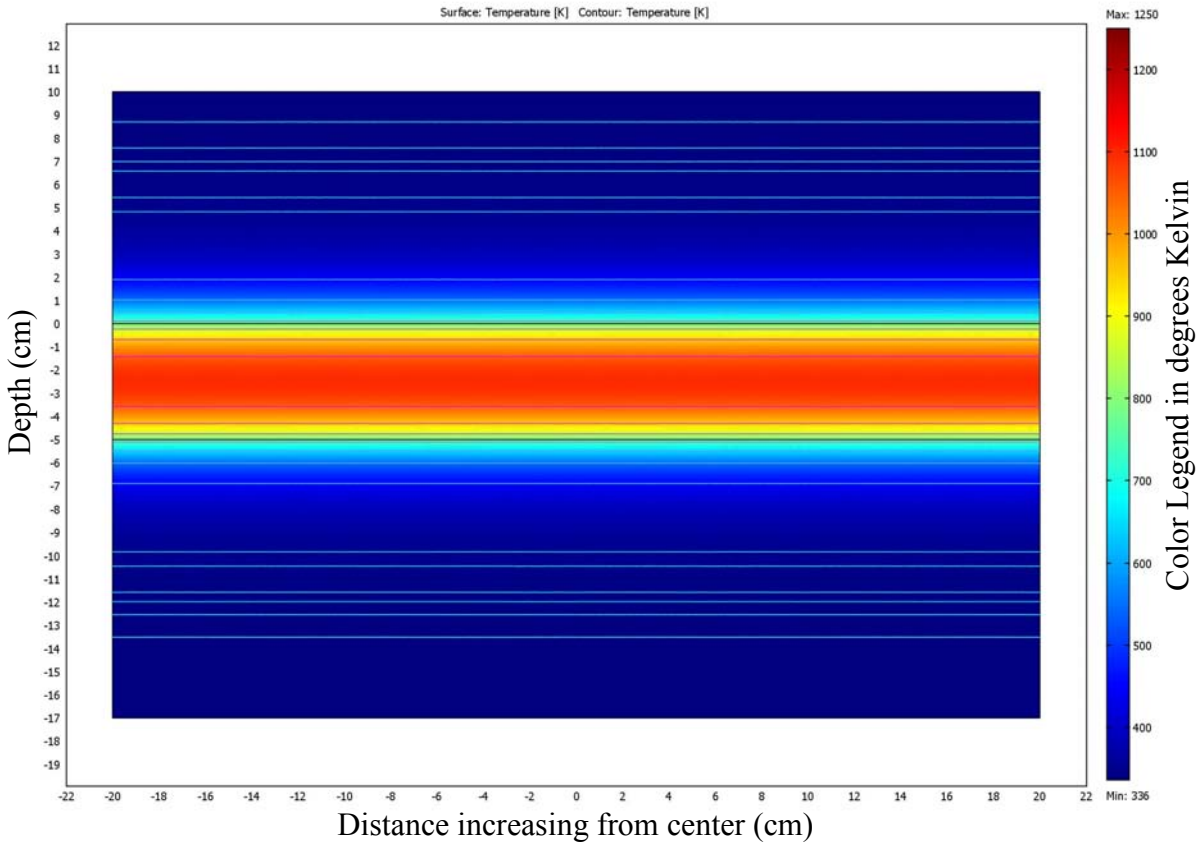

Figure 84: COMSOL generated image of a gypsum ejecta blanket. The stratigraphic column is gypsum ejecta blanket, heated gypsum ejecta blanket, gypsum bedrock. The horizontal black lines indicate the contact boundary between the (top to bottom) cool ejecta blanket, heated ejecta blanket, and bedrock. This figure illustrates the propagation of heat through the bedrock as well as the overlying ejecta blanket that has been deposited cold rather than heated.

Contour Intervals: 1150, 1050, 950, 850, 750, 650, 550, 450, 350, 345, 340, 339, 338, 337

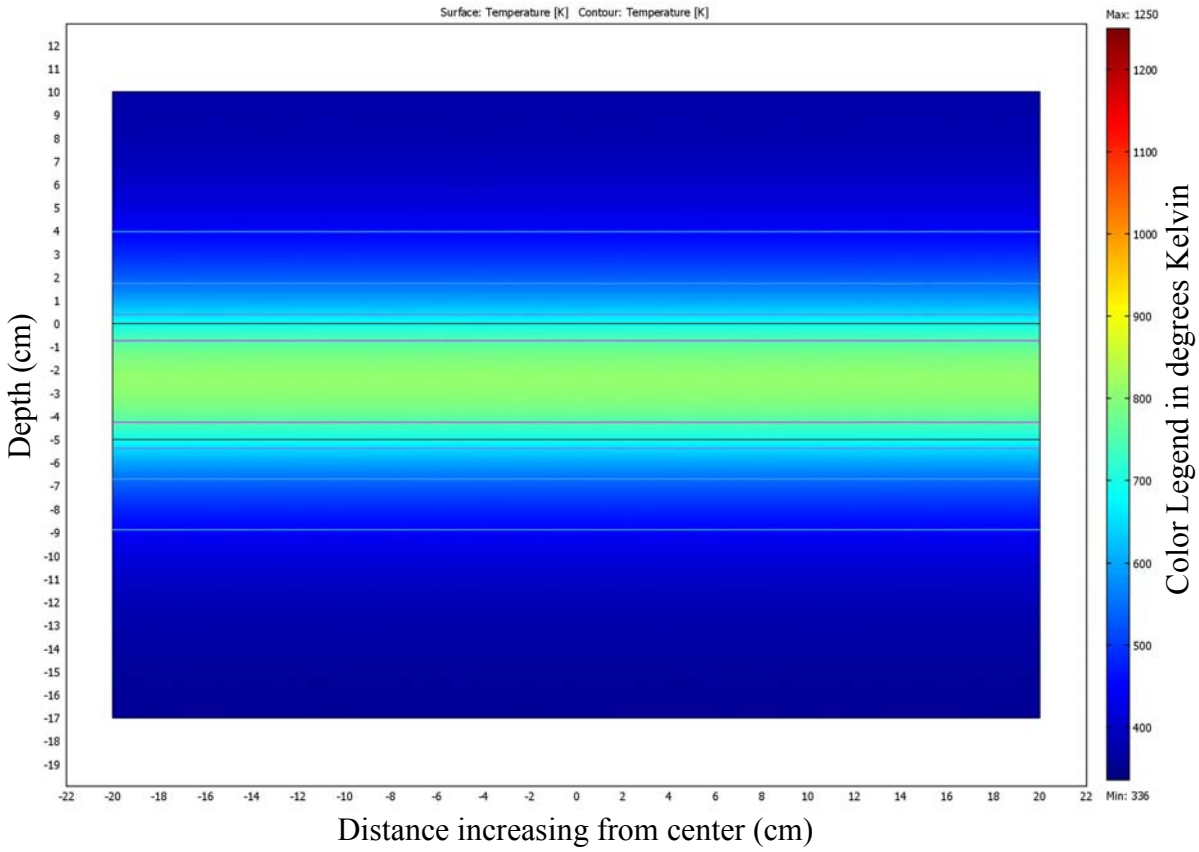

Figure 85: COMSOL generated image of a halite ejecta blanket. The stratigraphic column is halite ejecta blanket, heated halite ejecta blanket, halite bedrock. The horizontal black lines indicate the contact boundary between the (top to bottom) cool ejecta blanket, heated ejecta blanket, and bedrock. This figure illustrates the propagation of heat through the bedrock as well as the overlying ejecta blanket that has been deposited cold rather than heated.

Contour Intervals: 1150, 1050, 950, 850, 750, 650, 550, 450, 350, 345, 340, 339, 338, 337

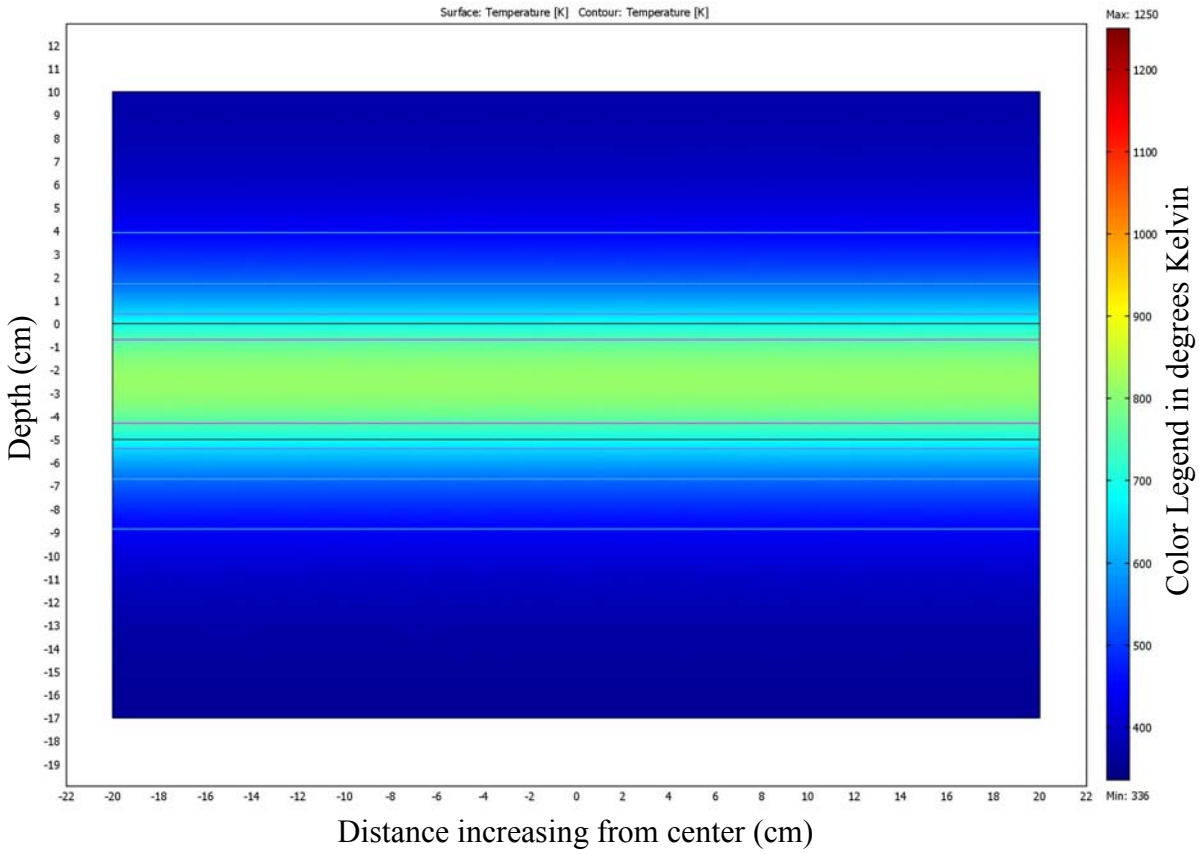

Figure 86: COMSOL generated image of a limestone ejecta blanket. The stratigraphic column is limestone ejecta blanket, heated limestone ejecta blanket, limestone bedrock. The horizontal black lines indicate the contact boundary between the (top to bottom) cool ejecta blanket, heated ejecta blanket, and bedrock. This figure illustrates the propagation of heat through the bedrock as well as the overlying ejecta blanket that has been deposited cold rather than heated.

Contour Intervals: 1150, 1050, 950, 850, 750, 650, 550, 450, 350, 345, 340, 339, 338, 337

References

Abramov, O and Kring, D. A., (2005) Impact-induced hydrothermal activity on early Mars. *Journal of Geophysical Research* **110**. doi: 10.1029/2005JE002453

Arnet, B., (2005) Earth. www.nineplanets.org/earth.html. Last updated: February 11, 2005. Visited April 26, 2005.

Baker, V. R., (2001) Water and the martian landscape. *Nature* **412**: 228-236.

Bartlett, R. W. (1969) Magma convection, temperature distribution, and differentiation. *American Journal of Science* **287**: 1067-1082.

Baross, J. A., Dahm, C. N., Ward, A. K., Lilley, M. D., and Sedell, J. R. (1982) Initial microbiological response in lakes to the Mt St Helens eruption. *Nature* **296**(4):49-52.

Benison, K. C., and Laclair, D. A., (2003) Modern and Ancient Extremely Acid Saline Deposits: Terrestrial Analogs for Martian Environments? *Astrobiology* **3**(3): 609-618.

Biemann, K., Oro, J., Toulmin III, P., Orgel, L. E., Nier, A. O., Anderson, D. M., Simmonds, P. G., Flory, D., Diaz, A. V., Rushneck, D. R., Biller, J. E., and Lafleur, A. L., (1977) The Search for Organic Substances and Inorganic Volatile Compounds in the Surface of Mars. Journal of Geophysical Research **82**(28): 4641.

Birch, F. and Clark, H., (1940) The thermal conductivity of rocks and its dependence upon temperature and composition. *Am. J. Sci.*, **238**: 529-558.

Bishop, J. L., (2005) Hydrated Minerals on Mars. In: *Water on Mars and Life*, Tetsuya Tokano (ed), Adv. Astrobiol. Biogeophys., pp. 65-96.

Boston, P. J., Ivanov, M. V., and McKay, C. P., (1992) On the possibility of chemosynthetic ecosystems in subsurface habitats on Mars. *Icarus* 95: 300-308.

Boston, P. J., Hose, L. D., Northup, D. E., and Spilde, M. N., (2006) The microbial communities of sulfur caves: A newly appreciated geologically driven system on

Earth and potential model for Mars. *Karst Geomorphology, Hydrology, & Geochemistry, Geological Soc. Amer. Special Paper* **404**: 331-344.

Boston, P. J., Spilde, M. N., Northup, D. E., Melim, L. A., Soroka, D. S., Kleina, L. G., Lavoie, K. H., Hose, L. D., Mallory, L. M., Dahm, C. N., Crossey, L. J., and Schelble, R. T., (2001) Cave biosignature suites: Microbes, minerals and Mars. *Astrobiology Journal* 1(1):25-55.

Bullock, M. A., (2005) The flow and ebb of water. *Nature* **438**: 1087-1088.

Cabrol, N. A. and Grin, E. A., (2005) Ancient and Recent Lakes on Mars. In: *Water on Mars and Life*, Tetsuya Tokano (ed.), Adv. Astrobiol. Biogeophys., pp. 235-259.

Cavicchioli, R., (2002) Extremophiles and the Search for Extraterrestrial Life. *Astrobiology* **2**(3): 281-292.

Christensen, P. R., Bandfield, J. L., Bell, J. F., Gorelick, N., Hamilton, V. E., Ivanov, A., Jakosky, B. M., Kieffer, H. H., Lane, M. D., Malin, M. C., McConnochie, T., McEwen, A. S., McSween Jr., H. Y., Mehall, G. L., Moersch, J. E., Nealson, K. H., Rice Jr., J. W., Richardson, M. I., Ruff, S. W., Smith, M. D., Titus, T. N., Wyatt, M. B., (2003) Morphology and Composition of the Surface of Mars: Mars Odyssey THEMIS Results. *Science* **300**, 2056 DOI: 10.1126/science.1080885.

Christensen, P. R., Wyatt, M. B., Glotch, T. D., Rogers, A. D., Anwar, S., Arvidson, R. E., Bandfield, J. L., Blaney, D. L., Budney, C., Calvin, W. M., Fallacaro, A., Fergason, R. L., Gorelick, N., Graff, T. G., Hamilton, V. E., Hayes, A. G., Johnson, J. R., Knudson, A. T., McSween Jr., H. Y., Mehall, G. L., Mehall, L. K., Moersch, J. E., Morris, R. V., Smith, M. D., Squyres, S. W., Ruff, S. W., Wolff, M. J., (2004) Mineralogy at Meridiani Planum from the Mini-TES Experiment on the Opportunity Rover. *Science* **306**: 1733-1739.

Cockell, C. S. and Lim, D. S. S., (2005) Impact Craters, Water and Microbial Life. In: *Water on Mars and Life*, Tetsuya Tokano (ed), Adv. Astrobiol. Biogeophys., pp. 261-275.

Cockell, C. S., Pascal, L., (2002) The biology of impact craters – a review. *Biol. Rev.* **77**: 279-310.

COMSOL AB_a, COMSOL Multiphysics 3.3: COMSOL Modeling Guide, 2005.

Connors, M., Hildebrand, A. R., Pilkington, M., Ortiz-Aleman, C., Chavez, R. E., Urrutia-Fucugauchi, J., Graniel-Castro, E., Camara-Zi, A., Vasquez, J., and Halpenny, J. F., (1996) Yucatán karst features and the size of Chicxulub crater. Geophysical Journal International 127 (3), F11–F14.

Dmitriev, A. P., Derbenev, L. S., and Goncharov, S. A., (1969) *Fiz. Tekh. Probl. Razrab. Polez. Iskop.*, **2**: 107-108; English Translation: *Sov. Min. Sci.*, **2**: 199-200.

Dunn, J. T., (1986) Diffusion in silicate melts: An introduction and literature review. In *Short course on silicate melts*, C. M. Scarfe (ed), 57-92. Toronto: Mineralogical Association of Canada.

Fairén, A. G., Fernández-Remolar, D., Dohm, J. M., Baker, V. R., Amils, R., (2004) Inhibition of carbonate synthesis in acidic oceans on early Mars. *Nature* **431**: 423-426.

Fishbaugh, K. E., F. Poulet, V. Chevrier, Y. Langevin, and J.-P. Bibring (2007), On the origin of gypsum in the Mars north polar region, *J. Geophys. Res.*, 112, E07002, doi:10.1029/2006JE002862.

Ford, D., (1988) Characteristics of Dissolutional Cave Systems in Carbonate Rocks. In: *Paleokarst*, James, N. P. and Choquette, P. W. (ed) pp. 25-57.

Goetz, W., Bertelsen, P., Binau, C. S., Gunnlaugsson, H. P., Hviid, S. F., Kinch, K. M., Madsen, D. E., Madsen, M. B., Olsen, M., Gellert, R., Klingelhöfer, G., Ming, D. W., Morris, R. V., Rieder, R., Rodionov, D. S., de Souza Jr., P. A., Schröder, C., Squyres, S. W., Wdowiak, T., Yen, A., (2005) Indication of drier periods on Mars from the chemistry and mineralogy of atmospheric dust. *Nature* **436**: 62-65.

Golden, D. C., (2005) Laboratory-simulated acid-sulfate weathering of basaltic materials: Implications for formation of sulfates at Meridiani Planum and Gusev craters, Mars. *Journal of Geophysical Research* **110**: E12S07.

Haskin, L. A., Wang, A., Jolliff, B. L., McSween, H. Y., Clark, B. C., Des Marais, D. J., Mclennon, S. M., Tosca, N. J., Hurowitz, J. A., Farmer, J. D., Yen, A., Squyres, S. W., Arvidson, R. E., Klingelhöfer, G., Schröder, C., de Souza Jr., P. A., Ming, D. W., Gellert, R., Zipfel, J., Bruckner, J., Bell III, J. F., Herkenhoff, K., Christensen, P. R., Ruff, S., Blaney, D., Gorevan, S., Cabrol, N. A., Crumpler, L., Grant, J., Soderblom, L., (2005) Water alteration of rocks and soils on Mars at the Spirit rover site in Gusev crater. *Nature* **436**: 66-69.

Hildebrand, A. R., Penfield, G. T., Kring, D. A., Pilkington, M., Zanoguera, Antonio, C., Jacobsen, S. B., Boynton, W. V., (September 1991). "Chicxulub Crater; a possible Cretaceous/Tertiary boundary impact crater on the Yucatan Peninsula, Mexico. *Geology* **19** (9): 867–871.

Hiscox, J. A., (2005) Biology and the Planetary Engineering of Mars. http://spot.colorado.edu/~marscase/cfm/articles/biorev3.html. Visited November 7, 2005.

Hode, T., von Dalwigk, I., Broman, C., (2003) A Hydrothermal System Associated with the Siljan Impact Structure, Sweden – Implications for the Search for Fossil Life on Mars. *Astrobiology* **3(2)**: 271-289.

Horedt, G. P. and Neukum, G. (1984) Comparison of Six Crater-Scaling Laws. *Earth, Moon, and Planets* **31**:265-269.

Housen, K. R., Schmidt, R. M., and Holsapple, K. A., (1983) Crater Ejecta Scaling Laws: Fundamental Forms Based on Dimensional Analysis. *J. of Geophys. Research* **88**(B3): 2485-2499.

Huppert, H. E. and Sparks, R. S. J., (1980) The fluid dynamics of a basaltic magma chamber replenished by influx of hot, dense ultramafic magmas. *Contributions to Mineralogy and Petrology* **75**: 279-289.

Incropera, Frank P., DeWitt, David P., Bergman, Theodore L., and Lavine, Adrienne S., (2006) Fundamentals of Heat and Mass Transfer, 6th ed. Wiley Publishing. pp. 1024.

Jakosky, B. M., and Phillips, R. J., (2001) Mars' volatile and climate history. *Nature* **412**: 237-244.

Jakosky, B. M., Haberle, R. M., Arvidson, R. E. (2005) The Changing Picture of Volatiles and Climate on Mars. *Science* **310**: 1439-1440.

Johnston, J. G., Boston, P. J., and Stafford, K. W., (2006) Assessment of Karst Landform Potential on Mars. Lunar and Planetary Science XXXVII.

Kempe, S., and Werner, M. S., (2003) The Kuka'iau Cave, Mauna Kea, Hawaii, Created by water erosion, a new Hawaiian cave type. *Journal of Cave and Karst Studies*, **65**(1): 53-67.

Kempe, S., Bauer, I., and Henschel, H.-V., (2003) Pa'auhau Civil Defense Cave on Mauna Kea, Hawaii, A lava tube modified by water erosion. *Journal of Cave and Karst Studies*, **65**(1): 76-85.

Kerr, R. A., (2004) Rainbow of Martian Minerals Paints Picture of Degradation. *Science* **305**: 770-771.

Kiefer, S. W., (1971) Shock Metamorphism of the Coconino Sandstone at Meteor Crater, Arizona. Specific heat of Solids of Geophysical Interest. California Institute of Technology, Ph. D. Thesis, pp 262. University Microfilms No. 71-27, 102.

Kieffer, H. H., Jakosky, B. M., Snyder, (1992) The Planet Mars: From Antiquity to the Present. In *Mars*, eds. Kieffer, H. H., Jakosky, B. M., Snyder, C. W. Matthews, M. S. University of Arizona Press. 1-33.

Klein, Cornelis, (2002) Mineral Science, 22nd Edition. John Wiley and Sons, pp. 641.

Klimchouk, A. and Andrejchuk, V., (1996) Sulphate rocks as an arena for karst development. *Int. J. Speleol.* **25**: (3-4).

Klingelhöfer, G., Morris, R. V., Bernhardt, B., Schröder, C., Rodionov, D. S., de Souza Jr., P. A. Yen, A., Gellert, R., Evlanov, E. N., Zubkov, B., Foh, J., Bonnes, U., Kankeleit, E., Gütlich, P., Ming, D. W., Renz, F., Wdowiak, T., Squyres, S. W., Arvidson, R. E., (2004) Jarosite and Hematite at Meridiani Planum from Opportunity's Mössbauer Spectrometer. *Science* **306**: 1740-1745.

Larson, D., (1993) The Recovery of Spirit Lake. *American Scientist* **81**(2):166-177.

Lide, David, E., (2004) CRC Handbook of Chemistry and Physics, 85th Edition. CRC Press, pp. 2656.

Lindroth, D. P. and Krawza, W. G., (1971) Bureau of Mines Rept. BMRI-7503, pp 28.

Lindsay, J. and Brasier, M., (2006) Impact craters as biospheric microenvironments, Lawn Hill Structure, Northern Australia. *Astrobiology* **6**(2): 348-363.

Madigan, M. T., and Martinko, J. M., (2006) Brock Biology of Microorganisms, 11th edition. Pearson Prentice Hall.

McKay, C. P. and Stoker, C. R., (1989) The early environment and it's evolution on Mars; implications for life. *Rev. Geophys.* 27, 189-214.

Melosh, H. J., (1989) *Impact Cratering: A Geologic Process (Oxford Monographs on Geology and Geophysics; no.11).* Oxford University Press Inc., pp. 245.

Murase, T. and McBirney, A. R., (1970) Thermal Conductivity of Lunar and Terrestrial Igneous Rocks in Their Melting Range. *Science* **170**: 165-167.

Newsom, H., (2005) Clays in the history of Mars. *Nature* **438**: 570-571.

Nisbet, E. G., and Sleep, N. H., (2001) The habitat and nature of early life. *Nature* **409**: 1083-1091.

Noritomi, K., (1956) *Sci. Rep. Tohoku Imp. Univ.* **7**(5): 190-200.

Paige, D. A., (2005) Ancient Mars: Wet in Many Places. *Science* **307**: 1575-1576.

Palliser, Chrsitopher and McKibbin, Robert, (1998) A Model for Deep Geothermal Brines, III: Thermodynamic Properties – Enthalpy and Viscosity. *Transport in Porous Media*. Vol. 35: 155-171.

Palmer, A. N., (1991) Origin and morphology of limestone caves. *Geological Society of America Bulletin* **103**: 1-21.

Palmer, A. N., (2007) Cave Geology. Cave Books Publishing. pp 454.

Perry, Dale L., and Phillips, Sidney L., (ed), (1995) Handbook of Inorganic Compounds. CRC Press, Inc. pp. 578.

Pierazzo, E., and Melosh, H. J., (2000) Understanding oblique impacts from experiments, observations, and modeling, *Ann. Rev. Earth Planet. Sci*., **28**, 141-167.

Pope, K. O., Ocampo, A. C., and Duller, C. E., (1993) Surficial geology of the Chicxulub impact crater, Yucatan, Mexico. *Earth, Moon, and Planets* **63**(2).

Poulet, F., Bibring, J.-P., Mustard, J. F., Gendrin, A., Mangold, N., Langevin, Y., Arvidson, R. E., Gondet, B., Gomez. C., the Omega Team, (2005) Phyllosilicates on Mars and implications for early martian climate. *Nature* **438**: 623-627.

Rodriguez, J. A. P., Sasaki, S., Dohm, J. M., Ken, L. T., Strom, B. Kargel, J., Kuzmin, R, Miyamoto, H., Spray, J. G., Fairen, A. G., Komatsu, G., Kurita, K., Baker, V., (2005) Control of impact crater fracture systems on subsurface hydrology, ground subsidence, and collapse, Mars. *J. Geophys. Res.* **110**, E06003, doi: 10.1029/2004JE002365.

Rossini, F. D., Cowie, P. A., Ellison, F. O., and Browne, C. C., (1956) Office of Naval Research Rept. ONR ANC 17, pp 448.

Sass, J. H. and Munroe, R. J., (ed), (1974) U.S. Geological Survey Open File Rept. 74-79, Sections 2-7.

Scarfe, C. M., (1986) Viscosity and density of silicate melts. In *Short course on silicate melts*, C. M. Scarfe (ed), 36-56. Toronto: Mineralogical Association of Canada.

Schultz, P. H., (1992) Atmospheric Effects on Ejecta Emplacement and Crater Formation From Magellan, Journal of Geophysical Research, **97:**E10, p. 16,183-16,248.

Sinke, G. C., (1959) AD 214 587.

Sleep, N. H., (1994) Martian plate tectonics. *J. Geophys. Res.* **99**: 5639-5655.

Somerton, W. H. and Boozer, G. D., (1960) *J. Petrol. Technol.*, **12**:77-81.

Stafford, K. W. and Boston, P. J., (2005) Theoretical Evaporite Karst Development on Mars. Lunar and Planetary Science XXXVI.

Thompson, G. W., and Garelis, E., (1956) Physical and thermodynamic properties of sodium, Sodium (M. Sittig). ACS Monograph 133, Reinhold, New York, Chapter 9.

Titus, T. N., (2004) Water, water everywhere. *Nature* **428**: 610-611.

Tosca, N. J., McLennan, S. M., (2006) Chemical divides and evaporite assemblages on Mars. Earth and Planetary Science Letters 241, 21-31.

Touloukian, Y. S., Judd, W. R., and Roy, R. F., (ed), (1989) Physical Properties of Rocks and Minerals. Cindas DataSeries on Material Properties, Vol II-2.

Treiman, A. H. and Schedl, A., (1983) Properties of carbonatite magma and processes in carbonatite magma chamgers. *Journal of Geology* **91**: 437-447.

Ward, D. M., and Cohan, F. M., (2005) Microbial Diversity in Hot Spring Cyanobacterial Mats: Pattern and Prediction. In MSU Thermal Biology Insititute's *Geothermal Biology and Geochemistry in Yellowstone National Park.* W. P. Inskeep and T. R. McDermott (eds.). 185-201.

Ward, A. K., Baross, J. A., Dahm, C. N., Lilley, M. D., and Sedell, J. R., (1983) Qualitative and Quantitative Observations on Aquatic Algal Communities and Recolonization within the Blast Zone of Mt. St. Helens, 1980 and 1981. *Journal of Phycology* **19**:238-247.

Wellsbury, P., Mather, I., and Parkes, R. J., (2002) Geomicrobiology of deep, low organic sediments in the Woodlark Basin, Pacific Ocean. *FEMS Microbiology Ecoloy* **42**(1): 59-79.

Wentworth, S. J., Bailey, J., McKay, D. S., Thomas-Keprta, K. L., (2002) Carbonates on Mars: All Martian Meteorites are not alike. GSA Abstract.

White, W. B., (1988) Geomorphology and hydrology of karst terrains. Oxford University Press, Inc. pp. 464.

Wrobel, K. E., Schultz, P. H., and Crawford, D. A., (2005) Effects on an early-time impact generated vapor clast in the martian atmosphere: formation of high-latitude pedestal craters. Role of Volatiles and Atmospheres on Marian Impact Craters 2005.

Yang, J. M., (1979) Thermophysical Propoerties of Rock Salt. CINDAS/Purdue University Internal Rept.

Yen, A. S., Gellert, R., Schröder, C., Morris, R. V., Bell, J. F., Knudson, A. T., Clark, B. C., Ming, D. W., Crisp, J. A., Arvidson, R. E., Blaney, D., Brückner, J., Christensen, P. R., DesMarais, D. J., de Souza, P. A., Economou, T. E., Ghosh,

A., Hahn, B. C., Herkenhoff, K. E., Haskin, L. A., Hurowitz, J. A., Joliff, B. L., Johnson, J. R., Klingelhöfer, G., Madsen, M. B., McLennan, C. M., McSween, H. Y., Richter, L., Rieder, R., Rodionov, D., Soderblom, L., Squyres, S. D., Tosca, N. J., Wang, A., Wyatt, M., Zipfel, J., (2005) An integrated view of the chemistry and mineralogy of martian soils. *Nature* **436**: 49-54.

Zuber, M. T., (2001) The crust and mantle of Mars. *Nature* **412**: 220-227.